



## The Use of Capacitive Transimpedance Amplifier Array Detectors for Mass Spectrometry

Item type	text; Electronic Dissertation
Authors	Zarzana, Christopher Andrew
Publisher	The University of Arizona.
Rights	Copyright © is held by the author. Digital access to this material is made possible by the University Libraries, University of Arizona. Further transmission, reproduction or presentation (such as public display or performance) of protected items is prohibited except with permission of the author.
Downloaded	4-Jan-2016 18:01:06
Link to item	<a href="http://hdl.handle.net/10150/202954">http://hdl.handle.net/10150/202954</a>

THE USE OF CAPACITIVE TRANSIMPEDANCE AMPLIFIER  
ARRAY DETECTORS FOR MASS SPECTROMETRY

by

Christopher Andrew Zarzana

---

A Dissertation Submitted to the Faculty of the  
DEPARTMENT OF CHEMISTRY AND BIOCHEMISTRY

In Partial Fulfillment of the Requirements  
For the Degree of

DOCTOR OF PHILOSOPHY  
WITH A MAJOR IN CHEMISTRY

In the Graduate College  
THE UNIVERSITY OF ARIZONA

2011

THE UNIVERSITY OF ARIZONA  
GRADUATE COLLEGE

As members of the Dissertation Committee, we certify that we have read the dissertation prepared by Christopher Andrew Zarzana  
entitled The Use of Capacitive Transimpedance Amplifier Array Detectors for Mass Spectrometry  
and recommend that it be accepted as fulfilling the dissertation requirement for the Degree of Doctor of Philosophy.

Date:

---

M. Bonner Denton, Ph. D

Date:

---

Craig A. Aspinwall, Ph. D

Date:

---

Vicki H. Wysocki, Ph. D

Date:

---

Stephen G. Kukolich, Ph. D

Final approval and acceptance of this dissertation is contingent upon the candidate's submission of the final copies of the dissertation to the Graduate College.  
I hereby certify that I have read this dissertation prepared under my direction and recommend that it be accepted as fulfilling the dissertation requirement.

Date:

---

Dissertation Director: M. Bonner Denton, Ph. D

### STATEMENT BY AUTHOR

This dissertation has been submitted in partial fulfillment of requirements for an advanced degree at the University of Arizona and is deposited in the University Library to be made available to borrowers under rules of the Library.

Brief quotations from this dissertation are allowable without special permission, provided that accurate acknowledgment of source is made. Requests for permission for extended quotation from or reproduction of this manuscript in whole or in part may be granted by the head of the major department or the Dean of the Graduate College when in his or her judgment the proposed use of the material is in the interests of scholarship. In all other instances, however, permission must be obtained from the author.

SIGNED: Christopher Andrew Zarzana

## ACKNOWLEDGEMENTS

I would like to thank a number of people who helped make this dissertation possible. First, I would like to thank my adviser, M. Bonner Denton, for his financial support, as well as his guidance throughout this process. I would like to further thank Bonner for the many hours he spent in his machine shop making a number of the components used in this work. I would also like to thank the members of the Denton Research Group, both past and present. In particular, I would like to thank Kent Gillig, Rodger Sperlin, Wit Wisniewsky, and Scott Tilden for many long conversations that helped shape this dissertation. I would like to thank Rodger Sperline as well for his assistance improving this manuscript. I would like to thank Lee Macomber and Ed Autz from the Chemistry and Biochemistry Machine Shop for their invaluable assistance and advice. I would also like to thank Dr. Jan Lorincik, who designed and built some of the equipment used in this work.

I would also like to acknowledge my family, for their support throughout my entire time in graduate school. In particular, I would like to thank my parents, who encouraged my inquisitiveness and curiosity about the world from a young age. Additional thanks go to my friends, who helped make my years in Tucson more enjoyable. I would like to extend a special thanks to Trina, for her love and support, especially at the end of this process.

## DEDICATION

*This work is dedicated to Trina*

## TABLE OF CONTENTS

LIST OF FIGURES . . . . .	10
LIST OF TABLES . . . . .	13
ABSTRACT . . . . .	14
CHAPTER 1 INTRODUCTION . . . . .	16
1.1 Single Channel Ion Detectors . . . . .	19
1.1.1 Electron Multipliers . . . . .	19
1.1.2 Faraday Detectors . . . . .	23
1.2 Multi-Channel Ion Detectors . . . . .	28
1.2.1 Photographic Emulsion Plates . . . . .	28
1.2.2 Multiple-Collector Detector Systems . . . . .	28
1.2.3 Micro-Channel Plate Arrays . . . . .	29
1.2.4 Faraday Arrays . . . . .	34
1.2.5 Capacitive Transimpedance Amplifier Array Detectors . . . . .	35
1.3 Instruments . . . . .	38
1.3.1 Traditional Double Focusing Mass Spectrometers . . . . .	40
1.3.2 Cycloidal Mass Spectrometer . . . . .	44
1.4 Thesis Organization . . . . .	48
CHAPTER 2 THEORY . . . . .	50
2.1 Linear System Theory . . . . .	50
2.1.1 Linear Time-Invariant and Shift-Invariant Systems . . . . .	50
2.1.2 Laplace Transforms . . . . .	53
2.1.3 Transfer Functions . . . . .	55
2.1.4 Continuous Fourier Transform . . . . .	55
2.1.5 Discrete-Time Fourier Transform . . . . .	57
2.1.6 Discrete Fourier Transform . . . . .	58
2.2 Random Variables and Processes . . . . .	59
2.2.1 Important Distribution . . . . .	60
2.2.2 Mean and Variance . . . . .	61
2.2.3 Independence . . . . .	62
2.2.4 Random Processes . . . . .	63
2.3 Linear Least Squares . . . . .	66
2.3.1 Ordinary Least Squares Slope Estimator . . . . .	66

TABLE OF CONTENTS – *Continued*

2.3.2	Generalized Least Squares Slope Estimator . . . . .	70
2.4	Noise . . . . .	71
2.4.1	Thermal Noise . . . . .	72
2.4.2	Shot Noise . . . . .	74
2.4.3	Flicker Noise . . . . .	74
2.4.4	Fixed Pattern Noise . . . . .	75
<b>CHAPTER 3 LINEAR MODELS OF A CAPACITIVE TRANSIMPEDANCE AMPLIFIER . . . . .</b>		<b>76</b>
3.1	Signal-to-Noise Models . . . . .	76
3.1.1	System Output with Deterministic Inputs . . . . .	77
3.1.2	System Output with Stochastic Inputs . . . . .	82
3.2	Mean-Variance for Gain Characterization . . . . .	86
3.2.1	Output Variance from Shot Noise on the Input . . . . .	87
3.2.2	Effect of Additional Source Noise on Mean-Variance Analysis . . . . .	90
3.3	Output Measurement Considerations . . . . .	91
3.4	Signal-to-Noise Ratios and Limits of Detection Equations . . . . .	92
3.4.1	Correlated Double Sampling (CDS) . . . . .	94
3.4.2	Least Squares Estimation of the Slope . . . . .	101
3.4.3	Influence of the Sampling Rate on SNR and LOD . . . . .	106
3.5	Conclusions . . . . .	107
<b>CHAPTER 4 DM0025 1696 PIXEL MONOLITHIC CTIA ARRAY DETECTOR . . . . .</b>		<b>111</b>
4.1	DM0025 . . . . .	111
4.2	Daughter Board and Motherboard . . . . .	116
4.3	Basic Operating Procedure . . . . .	117
4.3.1	Acquisition of All Pixels . . . . .	118
4.3.2	Single-Pixel Operation . . . . .	119
4.4	Reset Behavior . . . . .	120
<b>CHAPTER 5 CHARACTERIZATION OF THE 1696 PIXEL ARRAY DETECTOR . . . . .</b>		<b>126</b>
5.1	Flat Fielding of the 1696 Pixel CTIA Array Detector . . . . .	128
5.1.1	Gain Uniformity of the 1696 Pixel CTIA Array Detector . . . . .	129
5.1.2	Gain of a Subset of Pixels of the 1696 CTIA Array Detector . . . . .	131
5.2	Dark Current Characterization . . . . .	135
5.2.1	Experimental Procedures . . . . .	136
5.2.2	Results . . . . .	136
5.3	Temperature Dependence of the Post Reset Voltage . . . . .	139

TABLE OF CONTENTS – *Continued*

5.3.1	Results . . . . .	139
5.4	Sample-and-Hold Circuit Leakage . . . . .	149
5.4.1	Experimental Procedure . . . . .	149
5.4.2	Results . . . . .	149
5.5	Noise Characterization of the 1696 Pixel CTIA Detector as a Function of Temperature . . . . .	153
5.5.1	Experimental Procedure . . . . .	153
5.5.2	Standard Error vs Temperature . . . . .	154
5.5.3	Post-Reset Noise . . . . .	158
5.6	In-Depth Noise Characterization of the DM0025 at 228K . . . . .	163
5.6.1	Noise from the Sample-and-Hold Stage . . . . .	164
5.6.2	Noise in Reset . . . . .	170
5.6.3	Read Noise and Dark Current Noise . . . . .	174
5.7	Linearity of the 1696 Pixel CTIA Detector . . . . .	184
5.7.1	Experimental Procedure . . . . .	184
5.7.2	Results . . . . .	184
5.7.3	Dynamic Range and Charge Dynamic Range . . . . .	192
5.8	Predicted Limits of Detection in High Gain . . . . .	195
5.9	Conclusions . . . . .	198
 CHAPTER 6 EVALUATION OF THE 1696 PIXEL ARRAY DETECTOR FOR MASS SPECTROMETRY . . . . .		201
6.1	Adapting the 1696 Pixel CTIA Array Detector to the Monitor Instruments Cycloidal MS . . . . .	202
6.2	Performance of the Array Detector/Cycloidal MS System . . . . .	208
6.2.1	Instrument Control and Procedure . . . . .	208
6.2.2	Maximum Number of Samples . . . . .	209
6.2.3	Array Detection on a Linear Cycloid . . . . .	210
6.2.4	Limits of Detection . . . . .	216
6.2.5	Dynamic Range . . . . .	226
6.3	Conclusions . . . . .	231
 CHAPTER 7 FUTURE DIRECTIONS . . . . .		232
7.1	Detector Characterization . . . . .	232
7.2	Detector improvements . . . . .	234
7.3	Instrument Improvements . . . . .	235
7.4	Instrument Housing . . . . .	239
7.5	Instrument Control Electronics . . . . .	240
7.6	Data Collection System Improvements . . . . .	242

TABLE OF CONTENTS – *Continued*

APPENDIX A DERIVATIONS . . . . .	244
A.1 Output Voltage from an Input Voltage Noise . . . . .	244
A.2 Output Variance from an Input Voltage Noise Source . . . . .	246
A.3 Generalized Least Squares Variance with Time Increasing Variance .	246
A.4 Derivation of Ion Trajectories in a Linear Cycloid Mass Spectrometer	249
APPENDIX B CHARACTERIZATION OF SUPPORTING ELECTRONICS	253
B.1 NI PCI-6281 ADC Noise . . . . .	253
B.1.1 Experimental Procedure . . . . .	254
B.1.2 Results . . . . .	254
B.2 Characterization of the Burr Brown ACF2101 Switched Integrator .	254
B.2.1 Gain Calibration . . . . .	255
B.2.2 Post-Reset and Dark Current Characterization . . . . .	258
REFERENCES . . . . .	261

## LIST OF FIGURES

1.1	Types of electron multipliers. . . . .	21
1.2	Schematic of a Faraday type detector. . . . .	27
1.3	Micro-channel plate detector. . . . .	31
1.4	Electro-optical imaging detector. . . . .	33
1.5	Schematic of a Capacitive Transimpedance Amplifier ion detector. .	36
1.6	Mattauch-Herzog geometry double focusing mass spectrometer. . .	43
1.7	Ion trajectories in a cycloidal analyzer. . . . .	45
3.1	Linear models of the CTIA detector. . . . .	78
3.2	Linear model with only the source current present. . . . .	79
4.1	Block diagram of the DM0025 1696 pixel CTIA array detector. . . .	114
4.2	Diagram of a D flip-flop. . . . .	114
4.3	Voltage with the global reset line high, the sample-and-hold switch closed, and the device in high gain. . . . .	121
4.4	Voltage with the global reset line high, the sample-and-hold switch closed, and the device in low gain. . . . .	122
4.5	Global reset voltage with the sample-and-hold switch open in high gain for pixel 500. . . . .	124
4.6	Voltage before and after lowering of the global reset line in high gain.	125
5.1	Uniformity of the DM0025 pixels. . . . .	132
5.2	Gain calibration curve. . . . .	134
5.3	Dark current magnitude vs temperature of the DM0025. . . . .	138
5.4	Post-reset voltage with the device in high gain at 276K. . . . .	141
5.5	Post-reset voltage with the device in high gain at 228K. . . . .	142
5.6	Post-reset voltage with the device in low gain at 276K. . . . .	143
5.7	Post-reset voltage with the device in low gain at 228K. . . . .	144
5.8	Post-channel-reset voltage with the device in high gain. . . . .	146
5.9	Post-channel-reset voltage with the device in low gain. . . . .	147
5.10	Post-reset voltage vs time for pixel 500 with the device in high gain. .	148
5.11	Sample-and-hold leakage with the device in high gain. . . . .	151
5.12	Sample-and-hold leakage with the device in low gain. . . . .	152
5.13	Standard error of the slope measured in the dark vs temperature in high gain. . . . .	156

LIST OF FIGURES – *Continued*

5.14	Standard error of the slope measured in the dark vs temperature in low gain. . . . .	157
5.15	Various sources of post-reset voltage noises in high gain. . . . .	161
5.16	Various sources of post-reset voltage noises in low gain. . . . .	162
5.17	Noise from the sample-and-hold stage with the device in high gain. . . . .	168
5.18	Noise from the sample-and-hold stage with the device in low gain. . . . .	169
5.19	Noise with the device in reset in high gain. . . . .	172
5.20	Noise with the device in reset in low gain. . . . .	173
5.21	Output referred read noise vs pixel for the DM0025 in high gain. . . . .	177
5.22	Output referred read noise vs pixel for the DM0025 in low gain. . . . .	178
5.23	Output referred dark current noise vs pixel for the DM0025 in high gain. . . . .	179
5.24	Input referred read noise vs pixel for the DM0025 in high gain. . . . .	181
5.25	Input referred read noise vs pixel for the DM0025 in low gain. . . . .	182
5.26	Input referred dark current noise vs pixel for the DM0025 in high gain. . . . .	183
5.27	Output linearity of the DM0025 CTIA detector in high gain. . . . .	186
5.28	Output linearity of the DM0025 CTIA detector in low gain. . . . .	187
5.29	Maximum residual to determine the full scale range in high gain for the DM0025 CTIA detector. . . . .	189
5.30	Maximum residual to determine the full scale range in low gain for the DM0025 CTIA detector. . . . .	191
5.31	Charge dynamic range of the DM0025 CTIA array detector for both high and low gain. . . . .	194
5.32	Estimation of the limits of detection of the DM0025 in high gain as a function of number of samples . . . . .	196
5.33	Estimation of the limits of detection of the DM0025 in low gain as a function of number of samples . . . . .	197
6.1	Detector mounted on the copper finger with the thermoelectric cooler and support board. . . . .	205
6.2	Closeup of the Monitor Instruments linear cycloid mounted on the vacuum flange . . . . .	206
6.3	Detector mounted on the linear cycloid . . . . .	207
6.4	Mass spectrum of air with added CO <sub>2</sub> showing linear mass dispersion. . . . .	212
6.5	Mass spectrum of air with added CO <sub>2</sub> showing peak broadening and peak distortion. . . . .	213
6.6	Effect of positioning the array detector behind the focal plane . . . . .	215
6.7	Mass spectrum of perfluoro(methylcyclohexane) . . . . .	217

LIST OF FIGURES – *Continued*

6.8	Instrument response as a function of time from a $3.0e - 6$ mol/L sample of perfluoro(methylcyclohexane). The response peaks early due to incomplete mixing of the sample in the sample introduction vial, then levels off. Limit of detection data were collected 4 min after injection of each sample to ensure a stable response. . . . .	220
6.9	Instrument response as a function of concentration in high gain. . . . .	224
6.10	Instrument response as a function of concentration in low gain. . . . .	225
6.11	Dynamic range for the combined instrument with the detector in high gain . . . . .	227
6.12	Dynamic range for the combined instrument with the detector in low gain . . . . .	229
6.13	Response determined by peak area vs concentration in low gain. . . . .	230
A.1	Linear model of a CTIA with only the input voltage noise source. . . . .	245
A.2	The locus of the end of an arm attached to a wheel rolling on a line. . . . .	252
B.1	Calibration of the gain of the ACF2101 switched integrator . . . . .	257

## LIST OF TABLES

3.1	Summary of signal-to-noise equations . . . . .	110
3.2	Summary of LOD equations . . . . .	110
4.1	Structure of an 8 bit command . . . . .	118
5.1	Measured gains for the DM0025 in high and low gain. . . . .	135
5.2	Non-linearity for the DM0025 expressed as %FSR for high and low gain. . . . .	190
5.3	Summary of characterized detector parameters. Errors represent spread of measured parameters across the array . . . . .	200
6.1	Concentrations of perfluoro(methylcyclohexane) used for high gain with errors. . . . .	218
6.2	Concentrations of perfluoro(methylcyclohexane) used for low gain with errors. . . . .	219
6.3	Measured limits of detection for perfluoro(methylcyclohexane) in high and low gain compared to the predicted limits of detection from Chapter 5.8. . . . .	224
B.1	Voltage noise of the PCI-6281 ADC . . . . .	254
B.2	Characterized parameters of the ACF2101 switched integrator . . . . .	260

## ABSTRACT

Mass spectrometry is a powerful tool in the field of analytical chemistry. Though there have been numerous advances in mass analyzer technology over the decades, there has been comparatively little advancement in mass spectrometer detector technology. The development of the scientific charged-coupled device over 30 years ago brought the advantages of simultaneous detection over single channel detection to optical spectroscopy, including higher signal-to-noise ratios for a fixed analysis time, shorter analysis time to obtain a given signal-to-noise ratio, and greater sample throughput. While the use of array detectors to achieve simultaneous detection is commonplace in optical spectroscopy, ion detectors for mass spectrometry have lagged behind.

Over the last decade, a new type of ion detector, the capacitive transimpedance amplifier (CTIA) array detector, has been developed that has a number of properties that make it an excellent tool for simultaneous detection using dispersive mass spectrometers. The CTIA array detector has high sensitivity as well as high gain stability, allowing it to excel in applications that require high precision measurements of ion signals, such as isotope ratio mass spectrometry.

Capacitive transimpedance amplifier array detectors have previously been used

to demonstrate the power of simultaneous detection on Mattauch-Herzog double focusing mass spectrometers, but the non-linear mass dispersion of these instruments means that the resolution is not constant across the array. A different type of dispersive instrument, the linear cycloid, has a linear mass dispersion, making it a good candidate for an array detector.

The first detailed characterization of gain, read noise and dark-current noise, as well as of operating behavior over a range of temperatures, of the DM0025, a 1696 pixel CTIA array detector was performed. In addition, the first-ever combination of a CTIA array detector with a linear cycloid mass spectrometer was developed. This combined instrument demonstrated simultaneous detection of multiple masses, as well as a linear mass range. The results from the detailed characterization of the detector were used in conjunction with measurements of the performance of the combined instrument to suggest improvements for the next generation of linear cycloid instruments with CTIA array detectors.

## CHAPTER 1

### INTRODUCTION

Mass spectrometry has been a powerful tool for chemical analysis for many years.

Other analytical tools, such as optical spectroscopic instruments, have undergone a revolution with the introduction of focal plane detector arrays over two decades ago.

Through simultaneous detection of analytes, focal plane arrays allow for improved signal-to-noise ratios (S/N), shorter analysis times, and greater sample throughput. Although many of these advantages have been realized in optical spectroscopic methods, mass spectrometry has lagged behind. The field of mass spectrometry still relies primarily on two types of detectors: the electron multiplier and the Faraday type detector. Both electron multipliers and Faraday type detectors are widely employed on commercial instruments, but are single channel devices. While some progress has been made in the development of array detectors for ions, there is not yet a clear consensus on the optimal technology.

Of the many types of instruments used for mass spectrometry, the class that stands to benefit the most from array detection are magnetic and electric sector field instruments, which dispersively separate ions by mass-to-charge ( $m/z$ ) ratios.

Other class of instruments, such as time of flight , quadrupole, and trapping mass spectrometers, that do not separate ions along a focal plane do not gain as much

from array detectors. Sector field instruments are frequently used in the field of isotope ratio mass spectrometry. This technique involves precise measurement of the ratios between different isotopes of elements. These ratios are important in geological research, biology and life sciences, as well as nuclear chemistry (1). The characteristics of the ion detector used to measure the isotope intensities plays a large role in the ultimate sensitivity and precision of the measurements. Since precise measurements are the goal, the stability and reproducibility of the detector gain is of paramount importance. In addition, large linear dynamic ranges are desirable to allow for the quantitation of analyte over large ranges of concentrations. High detector sensitivity is desirable in order to detect very small signals.

For dispersive instruments, array detectors provide a large advantage through simultaneous detection. In a fixed analysis period, simultaneous detection results in increased signal-to-noise ratios (SNR) for the entire spectrum. When a scanning instrument acquires a spectrum, the instrument must acquire each unit of the spectrum separately in time. Ions produced in the source, that do not correspond to the unit of the spectrum the instrument is currently tuned, are lost. In contrast, with an array detector, the entire spectrum is acquired simultaneously, so those ions are not lost. For a fixed analysis time, this means more ions will accumulate on the detector, leading to a higher signal-to-noise ratio. Conversely, for a given desired signal-to-noise ratio (SNR), simultaneous detection will allow that SNR to be achieved in a shorter time, so less analyte is required.

In addition to improvement of SNR and decreased analysis times through collection of more signal, simultaneous detection can improve SNR through the reduction of correlated noise. Correlated noise affects all portions of the spectrum at a given time in the same way. Correlated noise comes from numerous sources, including the sample introduction equipment and the ion source. For isotope ratio mass spectrometry, simultaneous detection can serve to drastically reduce the effect of correlated noise, because the noise is the same for each isotope's data. Schilling et al. have demonstrated the ability of an array detector to overcome correlated noise both from sample introduction drift and from ion sources such as laser ablation (2). A final advantage from simultaneous detection is the ability to eliminate "spectral skew" while monitoring transients. Spectral skew arises when a scanning instrument is used to monitor a sample that is changing at a rate comparable to the scan speed. Portions of the spectrum collected at the beginning of the scan will reflect a different sample concentration than those collected at the end of the scan. It is especially critical to minimize this sort of error when measuring isotope ratios, as the spectral skew will lead to inaccuracies. Again, measurement of all portions of the spectrum of interest simultaneously will minimize error from spectral skew because changes in the sample affect all masses at the same time (2).

This dissertation describes a wide range of investigations providing the first detailed characterization of a new type of array ion detector, the Capacitive Transimpedance Amplifier (CTIA) array ion detector. In order to highlight the advan-

tages of the CTIA array ion detector, a brief review of ion detectors used for mass spectrometry, both single channel as well as multi-channel, will be presented.

## 1.1 Single Channel Ion Detectors

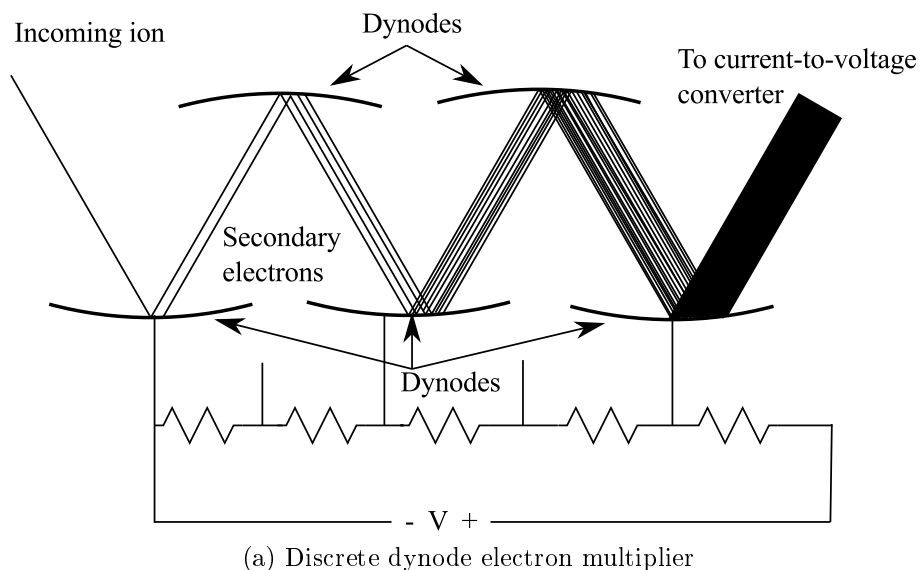
### 1.1.1 Electron Multipliers

An essential component of a mass spectrometer is the ion detector. The most commonly used detector in the field of mass spectrometry is the electron multiplier (EM) also known as a secondary electron multiplier (SEM). There are two main types of electron multipliers: discrete dynode shown in Figure 1.1a and continuous dynode (Channeltron<sup>®</sup>) shown in Figure 1.1b. These two types of electron multipliers work in essentially the same way. A large potential, typically on the order of a few kilovolts, is applied across the multiplier. In the discrete dynode case, it is applied across a resistor string with each dynode connected to a different element in the string, while in the continuous case the voltage is applied across the entire multiplier. An incoming ion strikes the first dynode producing secondary electrons that are accelerated by the potential farther into the device. These secondary electrons then strike the surface further down the channel, or the next dynode, giving rise to more secondary electrons. This process is repeated over numerous stages, producing a cascade of electrons. The result is a large amplification of the ion signal. Amplification factors of over a billion are now common in modern electron multipliers.

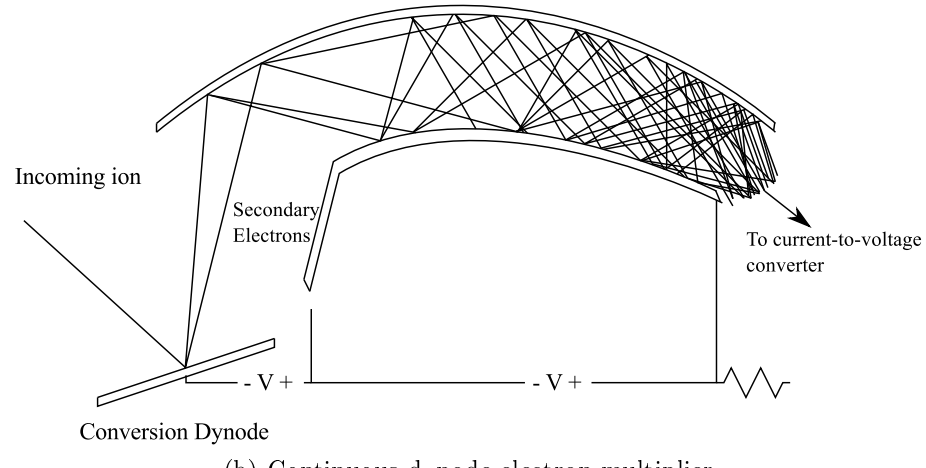
The output of the electron multiplier is processed in one of two ways: analog mode and pulse counting mode. In analog mode, the current is converted to a voltage by a resistor or a current-to-voltage amplifier and then digitized. This mode is suitable for the detection of ion fluxes higher than around  $10^7$  ions per second. The limiting current measurable in analog mode is determined by the gain as well as the sources of noise, which include thermal noise, shot noise, flicker noise as well as other background noise processes arising from thermionic emission of electrons from the electroemissive surface and electron emission from background gas striking the electroemissive surface.

In pulse counting mode, the electron pulse resulting from a single ion impacting on the surface of the EM is electronically buffered, shaped, and then counted as discrete events (3). Pulse counting mode is most effective for low fluxes of ions, so that pulses from different ions do not overlap, a phenomenon known as "pulse pile-up". The maximum count rate to avoid pulse pile-up is dependent on the surface condition of the multiplier, as well as the bias voltage and the capacitance of the channel (3). The surface conditions of the multiplier can change with use as well as over time. Pulse counting mode has the same sources of noise as analog mode, but these noise sources produce smaller peaks than the ion signal, and so can be thresholded out, leading to greater sensitivity.

Current multiplication makes electron multipliers extremely sensitive, giving them the ability to detect single ions. But, this method of charge amplification



(a) Discrete dynode electron multiplier



(b) Continuous dynode electron multiplier

Figure 1.1: Types of electron multipliers.

also has inherent weaknesses for quantitative work. The gain is dependent on many factors, including the location of ion and secondary electron impacts and the condition of the detector surface. The detection efficiency of an electron multiplier is also highly dependent the kinetic energy of the incoming ions as well as the ion mass, because the impact of a heavy or slow ion has a low probability of generating secondary electrons. This limitation can be overcome through the use of a conversion dynode, which is a separate electrode held at a high potential placed in near the entrance of the electron multiplier (4). Due to the high potential, ions are accelerated into the conversion dynode with enough kinetic energy to produce secondary electrons. These secondary electrons are then detected with the electron multiplier.

Secondary electron emission is a highly variable process, making the value of the gain unstable with time. The behavior of the device changes with time because the surface changes due to the impact of ions, which can cause sputtering as well as deposition of previously deposited analyte. This variability in detector signal means that electron multipliers are not the best choice for high precision measurements.

Another important characteristic of electron multipliers is linear dynamic range. The linear dynamic range of electron multipliers in analog mode can range from as small as 1 order of magnitude for high gain operation up to 4 or more orders of magnitude for lower gain operation. Higher bias currents result in larger gains, but at the expense of linear dynamic range. The dynamic range in counting mode is limited to ion signals of less than  $10^6$  counts per second, due to "pulse pile-up".

Pulse pile-up occurs when the rate of incident ions is high enough that the output pulses from each ion event begin to overlap.

Electron multipliers also respond fairly rapidly to ions. Typical pulse widths are on the order of 20 ns, with rise times of 3 – 5 ns. A special type of multiplier that will be discussed later, the micro-channel plate (MCP) detector often used for time of flight mass spectrometry, has typical pulse widths on the order of hundreds of picoseconds, with rise times even shorter.

A new type of multiplying detector, the MagneTOF<sup>TM</sup>, uses superimposed electric and magnetic fields to guide secondary electrons, produced from ion collisions on an ion impact plate, to a series of dynodes, resulting in an electron cascade (5). This detector can achieve pulse widths of about 400 ps and remains linear at higher currents than a traditional EM detector. However, because the detector gain is still produced by an electron cascade, it is statistical in nature, and thus this detector may not be suitable for high precision measurements.

### 1.1.2 Faraday Detectors

The statistical nature of the current multiplication used in the electron multiplier creates variance, so for high precision quantitative work, a different detector must be used. The detector typically used is the Faraday type detector. These detectors consist of a metal plate, known as a Faraday plate, or a cup known as Faraday cup, connected directly to a current-to-voltage converter, also known as an electrometer,

as seen in Figure 1.2. Ions arriving on the plate produce a current that flows through the feedback resistor, resulting in an output voltage. By analyzing the amplifier circuit, the output voltage is found to be

$$V_{out} = -R_f i_{in} \quad (1.1)$$

Because the feedback resistance is provided by a passive component, it is extremely stable, and thus the current-to-voltage gain is extremely stable. This stability makes Faraday type detectors the detectors of choice for techniques that require high precision, such as isotope ratio mass spectrometry. In addition to high stability, the electrometers used for Faraday type detectors can have large dynamic ranges, typically accomplished using switchable gain, where elements with different resistances are switched into and out of the feedback loop. For detection of low intensity signals, a large resistor is used, resulting in a large current-to-voltage gain. As the signal increases towards a level that would limit the output, a new lower resistance element is switched in. Using switchable gain, large dynamic ranges, often over 10 orders of magnitude, can be achieved.

Faraday plates by themselves can suffer from inaccuracies due to secondary electron emission from the metal surface when the ion energies are over approximately 200 eV, depending on the metal (6). The secondary electron emission acts as a second current on the input, and if these electrons escape, this secondary electron current can lead to significant errors. There are several ways to reduce the influence of secondary electron emission from the detector surface. The simplest is simply to

use low enough ion energies such that there is little to no secondary electron emission from the surface. In many instrument configurations, this leads to lower resolution and/or throughput, so this is not often an acceptable solution. A common method for dealing with secondary electron emission is the use of a suppressor grid above the Faraday plate. This suppressor grid is biased such that electrons emitted by the detector surface are accelerated back into the detector surface. This prevents these electrons from escaping, thus removing the secondary electron current, and the error associated with it.

Another method for secondary electron suppression is to use a cup shaped electrode instead of a flat plate. This cup, as shown in Figure 1.2, has a small opening in the top to allow entrance of ions. Secondary electrons produced inside the cup strike the walls and are reabsorbed, mitigating the errors associated with the secondary electron emission. Faraday cup as well as plate designs are often surrounded with a grounded box to help reduce electromagnetic interference, lowering the noise measured by the detector. There are some intrinsic noise and sensitivity limitations inherent in the current-to-voltage amplifier that limit the ultimate sensitivity of the Faraday type detectors.

The primary disadvantage of a Faraday type detector is that the sensitivity is significantly less than that of an electron multiplier. Although electron multipliers are capable of single ion detection, the best Faraday cup detectors have a detection limit of around 1 fA, or approximately 6000 ions per second. This large difference

in sensitivity is partially due to the Faraday type detector's lack of internal amplification. However, this difference in sensitivity also arises from the use of a large resistor as the current-to-voltage conversion element. As will be discussed later, the noise produced by a resistor increases as the resistance increases, thus limiting the sensitivity.

Another limitation compared to electron multiplier detectors is the response time of the electrometers used with Faraday type detectors. As shown in Figure 1.2, there is some capacitance in the amplifier feedback loop in addition to the resistance. This capacitance can be added intentionally to provide noise suppression, but also arises due to the capacitance of the resistor element itself. The presence of this capacitance makes the feedback network act as a low pass filter, with time constant  $\tau = R_f C_f$ . The larger the feedback resistance, the larger the time constant, and thus the slower the response time of the detector. This means that Faraday type detectors can typically only be used on instruments that have stable ion beams.

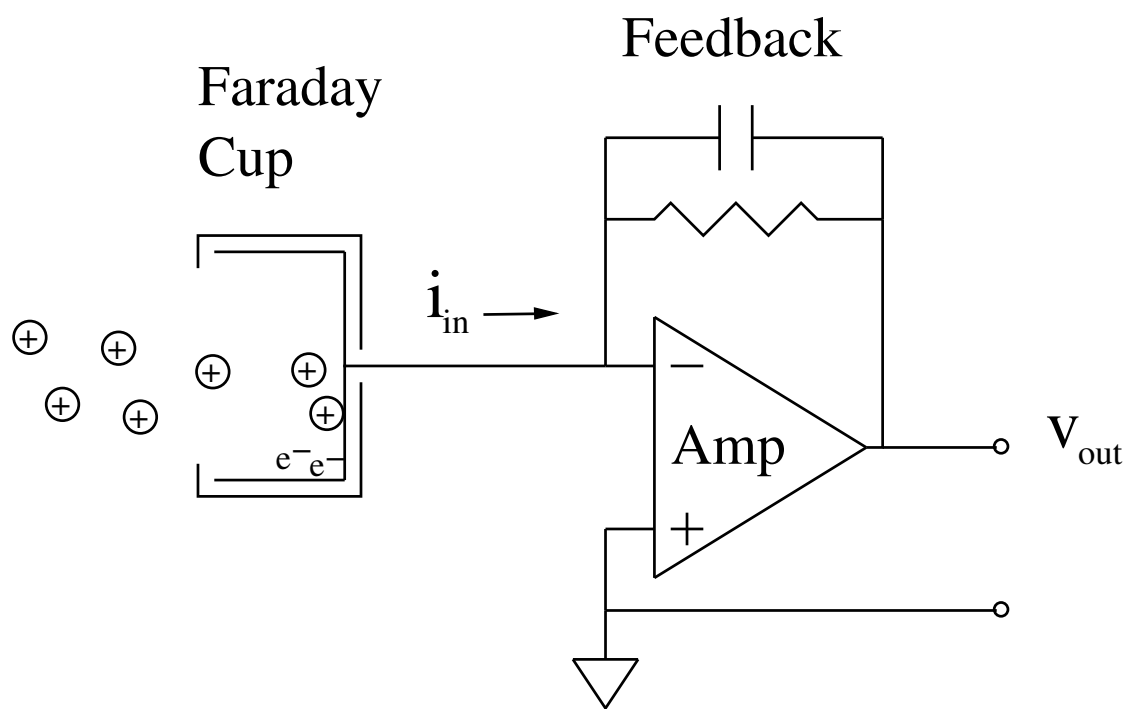


Figure 1.2: Schematic of a Faraday type detector.

## 1.2 Multi-Channel Ion Detectors

### 1.2.1 Photographic Emulsion Plates

One of the earliest ion detectors was a photographic emulsion plate. Incoming ions caused these plates to darken in the same manner as incoming light, allowing photographic emulsion plates to act as imaging and integrating ion detectors. Although photographic emulsion plates quickly faded from popularity, new instruments using them as detectors were being produced as late as the 1980's (7). A major advantage of photographic emulsion plates as an ion detector is they are the largest ion imaging detectors, but photographic emulsion plates suffer from numerous disadvantages including low sensitivity (8), dynamic ranges of only a few (1-2) orders of magnitude(9), poor reproducibility, and incompatibility with computer controlled data acquisition. (10-14)

### 1.2.2 Multiple-Collector Detector Systems

For isotope ratio mass spectrometry, as well as for other techniques that only require monitoring specific mass peaks in the spectrum, simultaneous detection can be accomplished by using multiple single channel detectors, placed at the locations of interest on the focal plane. This method has the advantage that advances in single channel detection technology are easily implemented in multi-collector systems. In addition, through careful spatial arrangement, multiple types of detectors can be used, allowing large dynamic ranges, up to  $10^{10}$ , to be obtained (15). One disad-

vantage with using multiple detectors is that they take up a relatively large physical space, making it difficult to position detectors close to each other. This has been partially overcome through the use of ion lenses to increase mass dispersion (16) as well as careful arrangement of the detectors on the focal plane (17, 18). The other major disadvantage of using multiple collectors is that, for many experiments, large numbers of masses - from tens to hundreds of  $m/z$  ratios - are desired, requiring excessively large numbers of detectors.

### 1.2.3 Micro-Channel Plate Arrays

A micro-channel plate (MCP) consists of an array of up to  $10^6$  microscopic glass channels  $5 - 50 \mu\text{m}$  in diameter, each of which acts like the continuous electron multiplier described above. Each channel typically has a gain on the order of  $10^4$  (19). Gains on the order of  $10^7$  or  $10^8$  can be achieved by stacking multiple MCPs in sequence, as shown in Figure 1.3 (20). Micro-channel plates typically produce pulse widths on the order of 100s of picoseconds, making them ideal for applications requiring high temporal resolution such as time of flight mass spectrometry (TOFMS). Each channel typically has a recovery time on the order of  $10^{-2}$  s, during which electrons that were discharged due to an ion impact on the entrance must be replenished (21). When operating as a single channel detector, this is not a problem because the ion beam is typically distributed over a large area of the MCP; while one channel may be recharging, other channels can still produce electron cascades.

This is more of a problem when using MCPs as spatially resolved detectors, because each  $m/z$  ratio is only exposed to a few micro-channels.

The dark current and dark noise of an MCP detector are superior to those of the Faraday type detector, and comparable to those of an electron multiplier. Like the electron multiplier, micro channel plates suffer from some drawbacks. As the pressure increases, background gas collisions on the channel surface cause the dark current and noise to increase. These effects can be seen at pressures above  $10^{-6}$  torr. Furthermore, the gain of the device is dependent on the surface conditions of the channels, which can change over time and with usage, degrading the long-term reproducibility of the detector and making it less desirable for high precision work. In addition, variations in the channel gain across the array can produce inaccuracies in mass ratios when using spatial resolved detection. The gain is also sensitive to changes in the incident ion kinetic energy and  $m/z$  ratio like an electron multiplier.

Because the channels in a MCP array are separate, the spatial information in arriving ion signal is preserved, but the electron pulse produced by the MCP must then be read out in a spatially resolved manner. Several ways to accomplish that have been explored are described below.

#### 1.2.3.a Electro-optical Imaging Detector

One method to spatially read the current from an MCP is to use a phosphor screen (23) or scintillation crystals (15, 24) to convert the electron pulses into light. This

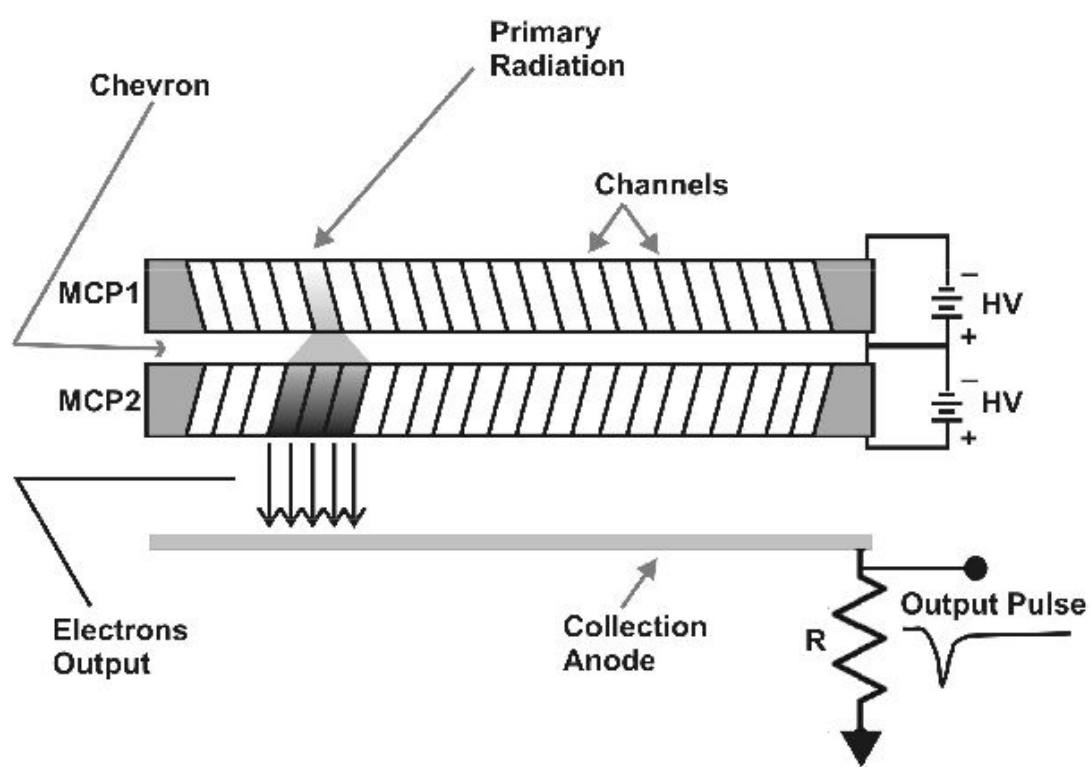


Figure 1.3: Micro-channel plate detector. (Reproduced with permission from (22))

light can then be detected using a charge coupled device (CCD) (25), as in Figure 1.4, or a photodiode array (26–28). The spatial resolution of these detectors is dependent on the pore size of the MCP, the pixel size of the optical detector, the spread of electrons as they leave the MCP and travel to the phosphor screen, and the spread of photons as they leave the phosphor screen. Spatial resolutions have been reported as small as  $50 - 100 \mu\text{m}$  (15), but these detectors are not ideal for highly precise measurements due to the presence of the MCP. In addition, the process of conversion of the signal from ions to electrons, to photons, and back into electrons is inefficient particularly at the phosphor screen, and adds noise and a loss of resolution at each stage. Finally, the MCP as well as the phosphor screen can add errors due to non-uniformity.

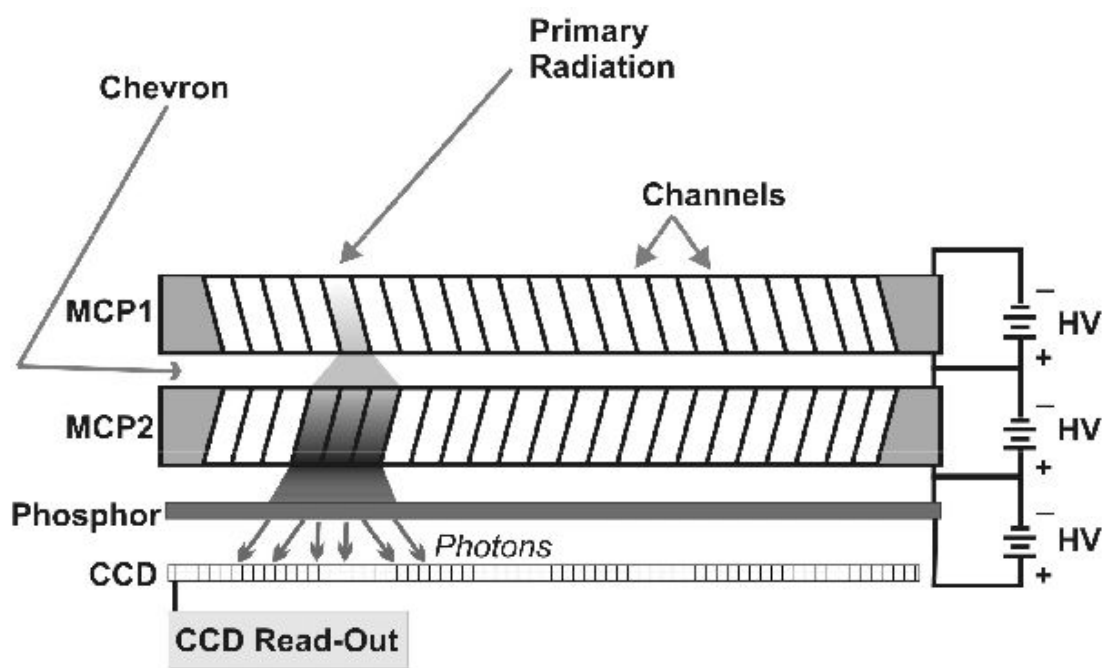


Figure 1.4: Electro-optical imaging detector. (Reproduced with permission from (22))

### 1.2.3.b Charge Division Detectors

Another method for detecting the electron cloud produced by an MCP is with a charge division detector. Charge division array detectors use an anode structure to divide the current exiting the MCP among several sensors. The signal measured by each sensor can be used to interpolate the position of the centroid of the arriving electron cloud. There are several types of anode structures used, but only a general description will be given here. An advantage of charge division detectors is they are often relatively simple to construct (15, 21). An additional advantage is that spatial resolution can be high, as good as  $20 \mu\text{m}$ , but many of these structures have difficulties detecting simultaneous events. In addition, these detectors typically do not have very high current- or charge-to-voltage gain, necessitating the current multiplication of the MCP.

### 1.2.4 Faraday Arrays

Ultimately, any detector using an MCP for front-end current multiplication will suffer from the disadvantages inherent with current multiplication. To circumvent these problems, new detector arrays have been developed that perform direct current- or charge-to-voltage conversion, forgoing the multiplication stage. These detectors are based on arrays of position sensitive anodes that are read out by back-end electronics. One such detector was developed at the Jet Propulsion Laboratory (JPL) by Sinha and Wadsworth that uses a CCD based array where the photon sensitive

elements of the CCD were replaced by capacitors, but, unfortunately, it suffered from high readout noise (29). Fuerstenau et al. have developed an Active Pixel Sensor (APS) using Complementary Metal-Oxide Semiconductor (CMOS) technology, based on pre-existing optical image sensors (30). Another array ion detector consisted of a micro-machined array of Faraday cups connected to a single amplifier, but had large detector widths and reduced spatial resolution , and the use of a single output amplifier prevented true simultaneous detection (31, 32).

### 1.2.5 Capacitive Transimpedance Amplifier Array Detectors

An ion detector that possess some powerful advantages for ion detection is the capacitive transimpedance amplifier (CTIA) array detector. The original CTIA array detector developed in the Denton laboratory used an array of charge collection strips, or micro-Faraday plates to capture ions. These micro-Faraday plates were wire-bonded to an array of multiplexed capacitive transimpedance amplifiers that was originally developed for astronomy (33). A block diagram showing the various parts of this new detector is shown in Figure 1.5. The CTIA is similar to a Faraday type detector, except it uses a capacitor in the amplifier feedback loop instead of a resistor. This change makes the CTIA a charge sensitive device, rather than a current sensitive device. The charge-to-voltage gain is controlled by the feedback capacitor: the smaller the feedback capacitance, the larger the gain. Because the gain is controlled by a passive component, it is extremely stable and reproducible,

making these detectors ideal for precision techniques like isotope ratio mass spectrometry. In addition, modern CMOS manufacturing allows fabrication of extremely small capacitors, allowing for very high gain.

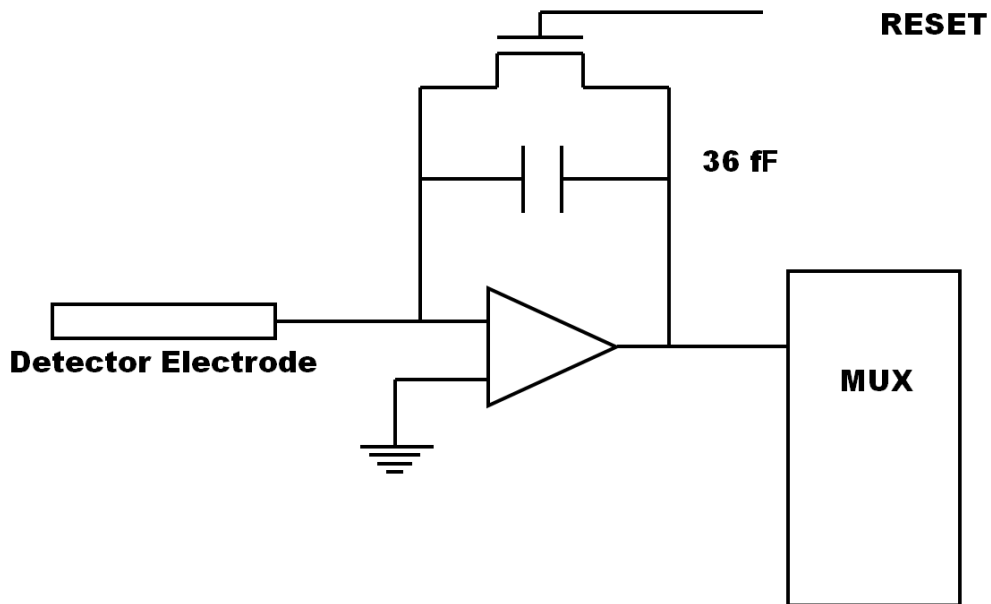


Figure 1.5: Schematic of a Capacitive Transimpedance Amplifier ion detector.

The use of a capacitor in the feedback loop, as opposed to a resistor, has implications for the noise performance of the device. The noise generated by the feedback resistor used in the electrometer in a traditional Faraday type detector increases with increasing resistor size, limiting sensitivity. The capacitor used in a CTIA produces less noise. In addition, small capacitors take up less physical space than large resistors, allowing more amplifiers to be constructed in a smaller space. Another implication of capacitive feedback is that the CTIA acts as an integrating detector, with charge stored on the feedback capacitor producing an output voltage. As will

be discussed in Chapter 3, this helps improve signal-to-noise ratios. Furthermore, because the output voltage can be read without disturbing the stored charge, the device can be read using non-destructive readouts (NDROs), which act like averaging to further improve SNR.

Capacitive transimpedance amplifier detectors have a wide range of applications. Because the detection efficiency of these detectors is independent of operating pressure, single-channel CTIA detectors have been used for high sensitivity measurements of explosives using ion mobility spectrometers at atmospheric pressure (34, 35). In contrast to an electron multiplier detector, the detection efficiency of a CTIA detector is independent of ion mass and kinetic energy, making single-channel CTIA detectors interesting candidates for high mass detection with time-of-flight mass spectrometers.

Arrays of CTIA detectors can be used for almost any charge detection application where ions are separated spatially. One example, which is the subject of this dissertation, is the use of CTIA array detectors with mass spectrometers that spatially disperse ions according to mass-to-charge. Another possible application of CTIA array detectors is for detection of ions that have been mass analyzed using arrays of ion traps (36). Finally, because CTIA detectors are sensitive to both positive and negative charges, they could be used to bring the benefits of multichannel detection to electron energy analysis techniques such as Auger, X-ray, and ultraviolet photoelectron spectroscopy when coupled with a dispersive electron energy

analyzer.

The original Denton CTIA array detector consisted of an array of 32 gold micro-Faraday plates wire-bonded to a multiplexed array of CTIAs (33). This detector was followed by a similar detector with 128 amplifiers (37). Because the micro-Faraday plates were wire-bonded to the amplifier array, the minimum micro-Faraday plate spacing was about  $50 \mu\text{m}$ , dictated by the limitations of wire-bonding. Experience with these two detectors lead to the development of the monolithic CTIA, where the micro-Faraday plates and the amplifiers were integrated on the same piece of silicon. This development lead to the creation of the 512 pixel CTIA array detector, and finally the 1696 pixel array detector that is the subject of this dissertation.

### 1.3 Instruments

To fully utilize the advantages of a CTIA array detector for mass spectrometry, the detector must be coupled with an analyzer that spatially separates ions. Some of the original mass spectrometers, including those developed by Dempster (38) and Bainbridge (39), used a magnetic field to spatially separate ions by momentum. This corresponds to separation by mass-to-charge if the ions are introduced with a narrow velocity spread.

If an ion with velocity  $v$  is introduced into a region with magnetic field  $\mathbf{B}$ , the ion experiences a force:

$$F = qv \times \mathbf{B} \quad (1.2)$$

where  $q$  is the charge of an electron. If the magnetic field is normal to the plane of ion velocity (that is, if the ion only moves in  $xy$  plane while the magnetic field is in the  $z$  direction) the force on the ion is:

$$F = qvB \quad (1.3)$$

This force is always perpendicular to both the ion velocity and the magnetic field. This perpendicular force results in a centripetal acceleration of the ion:

$$\frac{qvB}{m} = \frac{v^2}{r} \quad (1.4)$$

causing the ion to move in a circular path of radius  $r$ :

$$r = \frac{mv}{qB} \quad (1.5)$$

Bainbridge's mass spectrometer used a velocity filter to introduce ions with a narrow velocity spread into a  $180^\circ$  magnetic field, resulting in ions linearly dispersed by mass-to-charge along a focal plane (39). Dempster's original mass spectrometer used a large accelerating voltage to reduce the velocity spread of ions generated by a source (38). If an ion is accelerated by a voltage  $V$ , it gains kinetic energy  $qV$ . If the additional kinetic energy is large compared to the initial kinetic energy of the ion, its new kinetic energy is:

$$qV = \frac{1}{2}mv^2 \quad (1.6)$$

where  $m$  is the ion's mass and  $v$  is the ion's velocity. For this mass spectrometer, the radius of curvature in the magnetic field is:

$$r = \left( \frac{2mV}{qB^2} \right)^{\frac{1}{2}} \quad (1.7)$$

In contrast to Bainbridge's mass spectrometer, the radius of curvature in the magnetic field of Dempster's mass spectrometer is not linear with the mass-to-charge ratio of the ions.

These single magnetic field instruments were supplanted by Nier's sector magnetic analyzer (40) as well as by the development of the double focusing mass spectrometer, which uses both magnetic and electric fields to separate ions (39).

### 1.3.1 Traditional Double Focusing Mass Spectrometers

A radial electric field established between a pair of curved plates is referred to as an electric sector. The electric sector provides directional focusing by bringing ions from an ion source with the same energy but a small angular divergence into focus.

These ions follow a curved path with an approximate radius:

$$r = \frac{mv^2}{qE} \quad (1.8)$$

where  $m$  is the ion's mass,  $v$  its velocity, and  $E$  is the magnitude of the radial electric field.

A narrow beam of ions with identical  $m/z$  but a spread of energies that enters an electric sector is dispersed by velocity (ions with different velocities follow paths of different radius  $r$ ). If this beam then enters a homogeneous magnetic field, ions of different velocities are again deflected differently, resulting in "velocity focusing", where ions of the same  $m/z$  but different initial energy are focused at a single point after leaving the magnetic field (39). Ions with different  $m/z$  are separated by the

magnet and are thus velocity focused to different points. The locus of these points form a "velocity focusing curve" (39).

Ions with uniform energy but with an angular divergence that travel through an electric sector are brought into focus at a single point after which they begin to diverge again. This divergent beam is again brought into focus by passing through the magnetic field. If the beam consists of ions of differing  $m/z$ , each mass component is brought into directional focus at a different point after exiting the magnetic field. The locus of these points form a "directional focusing curve" (39).

For an ion beam with both an energy spread and an angular divergence entering an electric sector, ions of different velocities are brought into directional focusing at different points after passing through the electric sector. After passing through the magnetic field, ions of each velocity that have no angular divergence are brought into focus at a single velocity focusing point on the velocity focusing curve past the magnetic field. Ions with different angular divergences are brought into directional focus at a point on the directional focusing curve, which is in general different from the velocity focusing curve (39). Ions with different  $m/z$  are velocity focused at different points on the velocity focusing curve and into directional focus at different points on the directional focusing curve. Certain combinations of electric and magnetic fields cause these two curves to overlap at a single point, allowing a single selectable  $m/z$  to be simultaneously in velocity and directional focus, giving rise to the term "double-focusing". Double focusing mass spectrometers designed

by Dempster (39), Bainbridge and Jordan (41), and Nier (42) all behave in this manner.

Double focusing magnetic sectors of the Mattauch-Herzog geometry, shown in Figure 1.6, use a specific combination of electric and magnetic field such that the velocity and directional focusing curves overlap, continuously disperse ions on a focal plane according to their mass-to-charge ratio (43). This makes a Mattauch-Herzog geometry mass spectrometer an good candidate instrument for a focal plane detector. In a Mattauch-Herzog geometry double focusing mass spectrometer, the mass varies as the square of the distance along the focal plane (43), while most focal plane array detectors have detection elements with linear spacing. There is, however, another type of double focusing mass spectrometer, the cycloidal mass spectrometer, also known as the linear cycloid, which provides double focusing along a plane as well as linear mass spacing along that plane, making it an even better candidate instrument for a focal plane array detector.

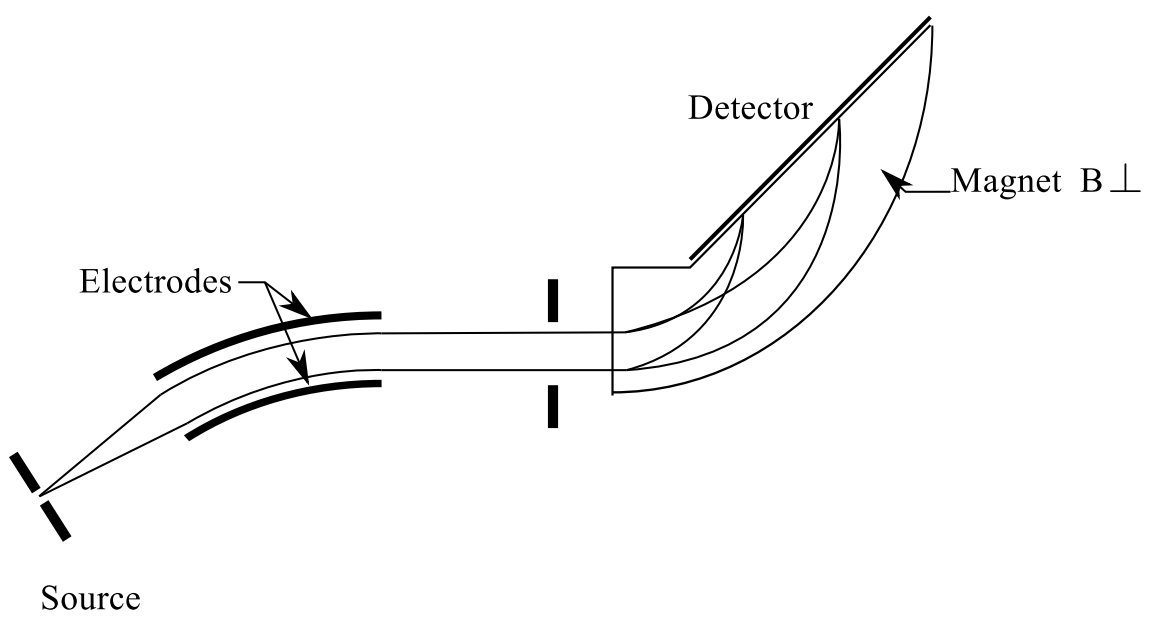


Figure 1.6: Mattauch-Herzog geometry double focusing mass spectrometer.

### 1.3.2 Cycloidal Mass Spectrometer

Cycloidal double focusing instruments are not common double focusing instruments, but ones that have some unique properties that make them excellent candidates for use with a focal plane array detector. Cycloidal analyzers consist of an electric- and a magnetic-field superimposed and set at right angles to each other. Ions are introduced with kinetic energy into this crossed field region in the direction opposite to the electric field, and undergo cycloidal trajectories due to the influence of both fields, as shown in Figure 1.7.

The equations of motion in vector notation for an ion in static electric and magnetic fields are:

$$\vec{F} = q\vec{E} + q\vec{v} \times \vec{B} \quad (1.9)$$

where  $q$  is the elementary charge, and  $\vec{F}$ ,  $\vec{E}$ , and  $\vec{B}$  are the force, electric field, and magnetic induction vectors and  $\vec{v}$  is the ion velocity vector. The trajectory described by these equations is a shape called a trochoid or cycloid (44–46). Due to the periodic nature of trochoid, charged particles that cross a plane  $y = y_0$  at some value  $x_0$  will again cross the plane  $y = y_0$  at  $x = x_0 + b$  where:

$$b = 2\pi a = 2\pi \frac{E}{B^2} \frac{m}{q} \quad (1.10)$$

A more detailed derivation of this equation can be found in Appendix A.4 and in (44).

Two things about Equation 1.10 are immediately important. First, none of

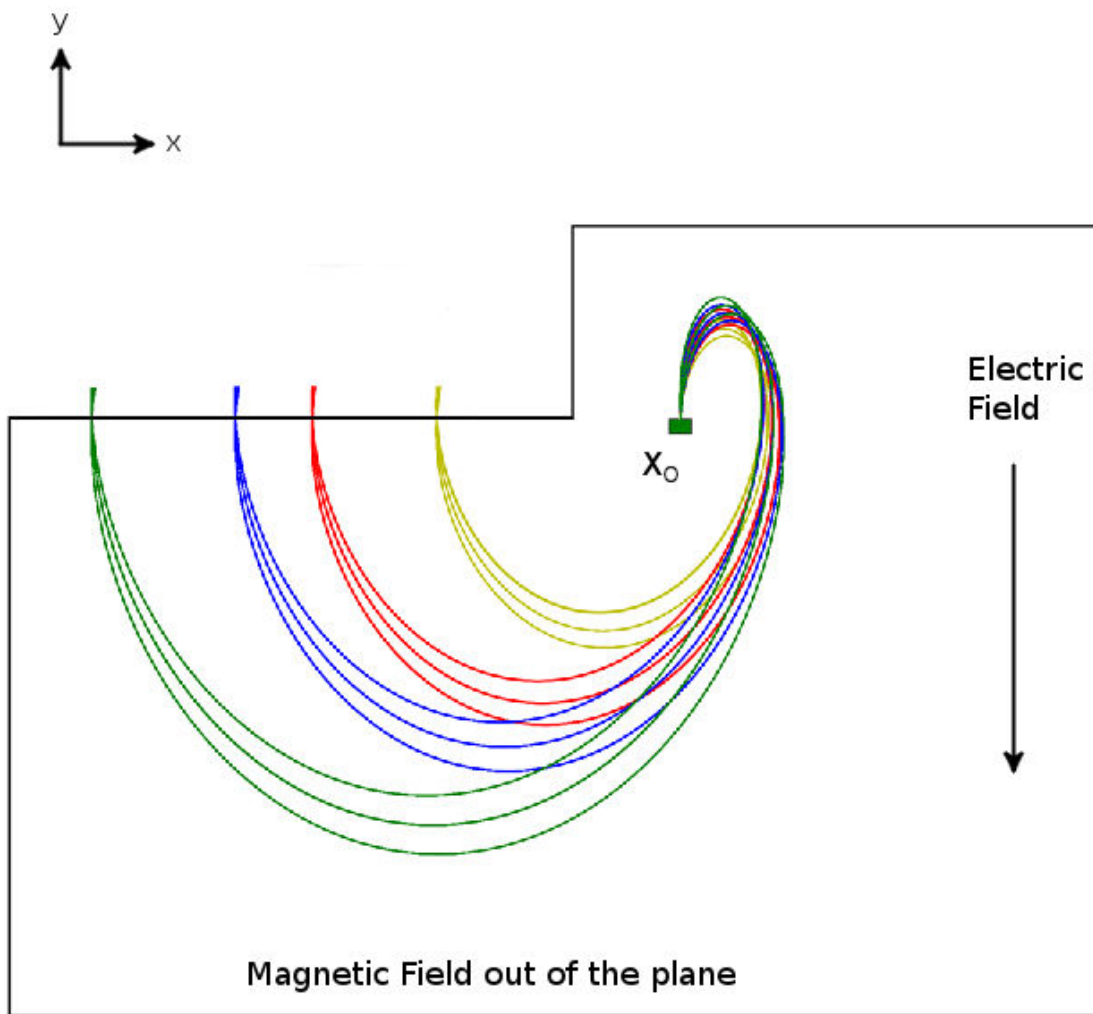


Figure 1.7: Ion trajectories in a cycloidal analyzer. Ions generated at  $x_0$  (the ion source) are refocused at the same  $y$  value, but displaced in the  $x$  depending on ion mass-to-charge ratio.

the initial conditions appear in the equation. This implies ion focusing properties are independent of initial ion velocity and angle. Second, and more importantly, the mass dispersion is linear, making cycloidal instruments ideal instruments for focal plane array detectors. Because the mass dispersion is linear, there will be a fixed number of pixels per mass unit across the whole mass range covered by the array. This means that resolution is constant across the whole array. This is in contrast to the more common Mattauch-Herzog geometry mass spectrometer, which has quadratic mass dispersion (47, 48).

The linear cycloid presents some problems for traditional electron multiplication detectors (EM and MCP). Because the focal plane lies inside both the magnetic and electric fields, the detector must also lie within these fields to obtain maximum resolution. The presence of the magnetic field induces a cyclotron motion in the secondary electrons generated in an EM or MCP detector, which complicates their use.

In addition, because the focal plane lies at the same electrical potential as the ion source, ions do not gain any net kinetic energy from passage through the analyzer, so they may not have sufficient kinetic energy to generate secondary electrons in a multiplier-type detector. The ion focal distance is unaffected by the initial kinetic energy (Equation 1.10) but the size and shape of the trajectory is affected. In the Monitor Instruments linear cycloid, ions are injected into the analyzer with only 10-15 eV of kinetic energy. Because the ions do not gain any net kinetic energy,

this is the energy of the ions arriving at the focal plane. The detection efficiency of multiplier detectors is very low at these ion energies, so detection would either require large signals or some secondary acceleration region after the focal plane. A secondary acceleration region would degrade resolution if using an MCP as an array detector, or would restrict operation to non-simultaneous detection if used in conjunction with an exit slit. In addition, because the focal plane is located at zero potential in the instrument and because a multiplier detector requires a large bias voltage, the output end of a multiplier detector would need to be at 2-3 kV. This means the current-to-voltage converter used to read out the output current from the multiplier detector would also need to be at this high potential. The output of the current to voltage converter would also be at high potential, so there would need to be a further step to convert the signal back down to a low potential compatible with the analog to digital data acquisition system, requiring extra electronics.

A CTIA array detector, on the other hand, does not suffer from any of these complications. The CTIA detector operates the same in the presence of a static magnetic field as it does with no magnetic field. In addition, because the CTIA is a charge detector, the detection efficiency is insensitive to the incoming ion kinetic energy. In fact, high kinetic energies (above 200 eV) can result in the production of secondary electrons (6), which can result in inaccuracies in detection, so it is desirable to use the CTIA to detect low energy ions. Since the CTIA does not require a large bias voltage, it can be placed in the instrument focal plane with no

additional electronics. Finally, because the DM0025 CTIA detector is a linear array, it can take advantage of the cycloid's linear mass dispersion, as well as provide truly simultaneous detection.

#### 1.4 Thesis Organization

This dissertation is intended for a chemistry audience, but makes heavy use of theories from electrical and systems engineering. Therefore, Chapter 2 presents a brief review of some of these theories that a chemist would not be expected to be familiar. These theories are used to develop a linear systems model of a CTIA amplifier in Chapter 3. A linear model was chosen because it is mathematically simple and reflects the ideal behavior of the CTIA. The actual device primarily discussed in this dissertation, the 1696 pixel CTIA array detector, is introduced in Chapter 4, and some observed deviations from ideal behavior of the device are described. Using the results derived in Chapter 3, a description of the detailed characterization of the CTIA array detector is presented in Chapter 5. Performance predictions of the 1696 pixel CTIA array detector were made, also based on the models derived in Chapter 3 are presented in Chapter 5. The performance of the 1696 pixel CTIA array detector for mass spectrometry was evaluated and the results are presented in Chapter 6, where general performance results from the combination of the detector with a linear cycloid, as well as limits of detection, are reported. These limits of detection are then compared with the performance predicted in

Chapter 5. Finally, Chapter 7 presents some general conclusions as well as future research directions.

## CHAPTER 2

### THEORY

This chapter presents a brief introduction to several important areas of electrical and communications engineering. The linear system theory reviewed here will be used in Chapter 3 to derive models of the ideal behavior for the CTIA array detector studied in this dissertation. Linear models are used primarily because linear models can typically be expressed in closed form. Non-linear models often must be solved numerically.

#### 2.1 Linear System Theory

Only a brief introduction of linear systems theory will be presented here. More detailed information can be found in any number of linear systems theory books (49).

##### 2.1.1 Linear Time-Invariant and Shift-Invariant Systems

A system can be thought of as an operator  $L[\cdot]$  that operates on an input function to produce an output function.

$$y(t) = L[x(t)] \quad (2.1)$$

Linearity means that

$$L[a_1x_1(t) + a_2x_2(t)] = a_1L[x_1(t)] + a_2L[x_2(t)] \quad (2.2)$$

for all  $a_1, a_2, x_1(t), x_2(t)$ .

Time-invariance means that if

$$y(t) = L[x(t)] \quad (2.3)$$

then

$$y(t+c) = L[x(t+c)] \quad (2.4)$$

for all  $x(t), c$ . Linear time-invariant (LTI) systems and their discrete counterparts, linear shift-invariant (LSI) systems are an important class of systems. By stipulation, this dissertation will use  $x(t)$  to represent continuous signals and  $x[n]$  to represent discrete signals.

A special input signal for continuous systems is the continuous delta function  $\delta(t)$ , defined as

$$\delta(t) = \begin{cases} \infty, & t = 0 \\ 0, & t \neq 0 \end{cases} \quad (2.5)$$

and with unit area.

$$\int_{-\infty}^{\infty} \delta(t) dt = 1 \quad (2.6)$$

For discrete systems this special input function is the discrete delta sequence, given

by

$$\delta[n] = \begin{cases} 1, & n = 0 \\ 0, & n \neq 0 \end{cases} \quad (2.7)$$

An important property of the continuous delta function is known as the sifting property,

$$\int_{-\infty}^{\infty} f(\tau) \delta(t - \tau) d\tau = \int_{-\infty}^{\infty} f(t - \tau) \delta(\tau) d\tau = f(t) \quad (2.8)$$

The result of the convolution of a function with a continuous delta is just original function. For the discrete delta sequence, any sequence  $f[n]$  may be written as a weighted sum of discrete deltas, known as discrete sifting:

$$\sum_{k=-\infty}^{\infty} f[k] \delta[n - k] = \sum_{k=-\infty}^{\infty} f[n - k] \delta[k] = f[n] \quad (2.9)$$

The output of a continuous LTI system with  $\delta(t)$  as its input is designated  $h(t)$  and is known as the impulse response function. The output of a discrete LSI system with  $\delta[n]$  as the input is designated  $h[n]$ .

Another special signal is the continuous unit step function,  $U(t)$ :

$$U(t) = \begin{cases} 0, & t < 0 \\ 1, & t > 0 \end{cases} \quad (2.10)$$

with a discontinuity at  $t = 0$ . The unit step function can be thought of as the running time integral of the continuous impulse function:

$$U(t) = \int_{-\infty}^t \delta(\tau) d\tau \quad (2.11)$$

The continuous unit step function has a discrete equivalent, the discrete unit step function,  $U[n]$  defined by:

$$U[n] = \begin{cases} 0, & n < 0 \\ 1, & n \geq 0 \end{cases} \quad (2.12)$$

Analogous to the continuous case, the discrete unit step function is the running sum of the discrete impulse function:

$$U[n] = \sum_{m=-\infty}^n \delta[m] \quad (2.13)$$

The output of a LTI system can be calculated from the convolution of the input signal and the impulse response.

$$y(t) = x(t) * h(t) = \int_{-\infty}^{\infty} x(\tau)h(t - \tau) d\tau = \int_{-\infty}^{\infty} x(t - \tau)h(\tau) d\tau \quad (2.14)$$

For a discrete system, the convolution integral in Equation 2.14 is replaced by the convolution sum given by

$$y[n] = x[n] * h[n] = \sum_{k=-\infty}^{\infty} x[k]h[n - k] = \sum_{k=-\infty}^{\infty} x[n - k]h[k] \quad (2.15)$$

### 2.1.2 Laplace Transforms

Equation 2.14 involves an integral, which can sometimes be difficult to compute. In addition, linear systems are typically modeled using differential equations containing derivatives as well as integrals of functions, which complicates determination of solutions. These complications can often be avoided by changing the domain of the

problem through the use of the Laplace transform. The Laplace transform of an arbitrary function  $x(t)$  is:

$$X(s) = \int_{-\infty}^{+\infty} x(t) \exp^{-st} dt \quad (2.16)$$

where  $X(s)$  is the s domain representation of  $x(t)$ , and  $s$  is a complex variable generally in the form:

$$s = \sigma + j\omega \quad (2.17)$$

Here the engineering convention  $j = \sqrt{-1}$  is followed instead of the mathematics convention  $i = \sqrt{-1}$ . Because Equation 2.16 involves an integral, there can be some values of  $s$  for which the integral does not converge. The range of values of  $s$  for which the integral in Equation 2.16 converges is known as the region of convergence (ROC).

The primary advantage of working in the s domain is that differentiation and integration operations in the time domain are multiplication and division operations in the s domain. For example, differentiation with respect to time in the time domain is just multiplication by  $s$  in the s domain. If

$$x(t) \xleftrightarrow{\mathcal{L}} X(s)$$

then:

$$\frac{dx(t)}{dt} \xleftrightarrow{\mathcal{L}} sX(s) \quad (2.18)$$

$$\int_{-\infty}^t x(\tau) d\tau \xleftrightarrow{\mathcal{L}} \frac{1}{s} X(s) \quad (2.19)$$

Another important property of the Laplace transform is known as the convolution property. This property states that the convolution of two functions  $x_1(t)$  and  $x_2(t)$  in the time domain is equal to the product of Laplace transforms of the two functions in the s domain:

$$x_1(t) * x_2(t) \xleftrightarrow{\mathcal{L}} X_1(s)X_2(s) \quad (2.20)$$

### 2.1.3 Transfer Functions

Applying the Laplace transform to Equation 2.14 and taking advantage of the convolution property yields:

$$Y(s) = X(s)H(s) \quad (2.21)$$

where  $Y(s)$ ,  $X(s)$ , and  $H(s)$  are the Laplace transforms of  $y(t)$ ,  $x(t)$ , and  $h(t)$  respectively. Rearranging Equation 2.21 gives:

$$\frac{Y(s)}{X(s)} = H(s) \quad (2.22)$$

The transfer function,  $H(s)$ , contains all the information about how an input function  $X(s)$  is transformed into an output function  $Y(s)$  by the system.

### 2.1.4 Continuous Fourier Transform

A useful mathematical tool for the analysis of continuous linear systems is the continuous-time Fourier transform (CTFT), given by

$$H(j\omega) = \int_{-\infty}^{\infty} h(t)e^{-j\omega t} dt = \mathcal{F}\{h(t)\} \quad (2.23)$$

By comparing Equation 2.23 with Equation 2.16, it is clear that the Fourier transform is simply the Laplace transform evaluated at

$$s = j\omega \quad (2.24)$$

where  $\omega$  is angular frequency and  $\omega = 2\pi f$  where  $f$  is ordinary frequency in hertz.

This is only true if  $s = j\omega$  lies in the region of convergence of the Laplace transform of  $h(t)$ . The symbol  $\mathcal{F}\{\cdot\}$  denotes the continuous-time Fourier transform (CTFT) operator, and  $H(j\omega)$  is known as the continuous-time Fourier transform of  $h(t)$ . The CTFT computes the projection of the function  $h(t)$  onto the orthogonal basis set  $\{e^{-j2\pi ft}, -\infty \leq f < \infty\}$ . In other words,  $\mathcal{F}\{\cdot\}$  returns the frequencies and amplitudes of the continuous set of complex exponentials that can be combined to form  $h(t)$ . The inverse Fourier transform reverses this process, and is given by

$$h(t) = \frac{1}{2\pi} \int_{-\infty}^{\infty} H(j\omega) e^{j\omega t} d\omega = \mathcal{F}^{-1}\{H(j\omega)\} \quad (2.25)$$

where  $\mathcal{F}^{-1}\{\cdot\}$  represents the inverse CTFT operator. Equations 2.23 and 2.25 represent the continuous-time Fourier transform pair.

For ordinary frequency in hertz, the Fourier transform of  $h(t)$  and the inverse Fourier transform are

$$H(f) = \int_{-\infty}^{\infty} h(t) \exp^{-j2\pi ft} dt = \mathcal{F}\{h(t)\} \quad (2.26)$$

$$h(t) = \int_{-\infty}^{\infty} H(f) \exp^{j2\pi ft} df = \mathcal{F}^{-1}\{H(f)\} \quad (2.27)$$

An important property of the continuous Fourier transform is known as Parse-

val's theorem

$$\int_{-\infty}^{\infty} g(t)h^*(t) dt = \int_{-\infty}^{\infty} G(f)H^*(f) df. \quad (2.28)$$

The energy  $\mathbf{E}$  in a signal  $h(t)$  is equal to

$$\begin{aligned} E &= \int_{-\infty}^{\infty} h(t)h^*(t) dt \\ &= \int_{-\infty}^{\infty} |h(t)|^2 dt \\ &= \int_{-\infty}^{\infty} |H(f)|^2 df. \end{aligned} \quad (2.29)$$

This is simply an expression of the conservation of energy; the energy of a signal is the same whether it is represented in the time domain or the frequency domain.

The energy density spectrum of a function  $h(t)$  is given by (50)

$$S(f) = |H(f)|^2 \quad (2.30)$$

### 2.1.5 Discrete-Time Fourier Transform

For discrete signals there exists an analogous transform pair to the continuous-time Fourier transform pair.

$$X(\Omega) = \sum_{n=-\infty}^{\infty} x[n]e^{-j\Omega n} \quad (2.31)$$

$$x[n] = \frac{1}{2\pi} \int_{-\pi}^{\pi} X(\Omega)e^{j\Omega n} d\Omega \quad (2.32)$$

An important thing to notice is that although the sequence  $x[n]$  is discrete, its discrete-time Fourier transform is a continuous function of digital frequency  $\Omega$ . (49–51)

### 2.1.6 Discrete Fourier Transform

For a finite length sequence  $x[n]$ ,  $0 \leq n \leq N - 1$ , there exists a simple relationship between the sequence  $x[n]$  and its discrete-time Fourier transform  $X(\Omega)$  known as the discrete Fourier transform, or DFT. For a sequence of length  $N$ , only  $N$  samples of the continuous discrete-time Fourier transform of the sequence are required to determine the original sequence  $x[n]$ , and thus  $X(\Omega)$ , uniquely. Essentially, the discrete Fourier transform (DFT) is the discrete-time Fourier transform (DTFT) sampled uniformly at  $N$  points. The DFT and its inverse, the IDFT, are defined as follows (49–51):

$$X(\Omega)|_{\Omega=2\pi k/N} = X[k] = \sum_{n=0}^{N-1} x[n]e^{-j2\pi k \frac{n}{N}} \quad (2.33)$$

$$x[n] = \frac{1}{N} \sum_{k=0}^{N-1} X[k]e^{j2\pi k \frac{n}{N}} \quad (2.34)$$

Analogous to Equation 2.30, the energy spectrum of a discrete sequence is (50)

$$S[k] = |TX[k]|^2 \quad (2.35)$$

where  $T$  is the sampling time. The power spectral density (PSD) of a discrete sequence is (50)

$$P[k] = \frac{S[k]}{NT} = \frac{T}{N} |X[k]|^2 \quad (2.36)$$

$$= \frac{T}{N} \left| \sum_{n=0}^{N-1} x[n]e^{-j2\pi k \frac{n}{N}} \right|^2 \quad (2.37)$$

## 2.2 Random Variables and Processes

This dissertation will be dealing extensively with the concepts of random variables and sequences as a model of noise, as well as the response of linear systems to random process (noise) inputs. Following the conventions in Papoulis (52), all random variables (RV's) will be written in boldface letters ( $\mathbf{x}$ ). A formal definition of a random variable from Papoulis (52) is as follows:

"DEFINITION. An RV  $\mathbf{x}$  is a process of assigning a number  $\mathbf{x}(\xi)$  to every outcome  $\xi$ . The resulting function must satisfy the following two conditions but is otherwise arbitrary:

**I.** The set  $\mathbf{x} \leq x$  is an event for every  $x$ .

**II.** The probability of the events  $\{\mathbf{x} = \infty\}$  and  $\{\mathbf{x} = -\infty\}$  equal 0:

$$P\{\mathbf{x} = \infty\} = 0 \quad P\{\mathbf{x} = -\infty\} = 0$$

The second condition states that, although we allow  $\mathbf{x}$  to be  $+\infty$  or  $-\infty$  for some outcomes, we demand that these outcomes form a set with zero probability."  
(52)

Two important descriptors of random variables are the (cumulative) distribution function and the density function. The distribution function of RV  $\mathbf{x}$  is defined as the function

$$F_x(x) = P\{\mathbf{x} \leq x\} \tag{2.38}$$

defined for every  $x$  from  $-\infty$  to  $\infty$ . Thus, the distribution function  $F_x(x)$  is the probability that the random variable  $\mathbf{x}$  is less than or equal to  $x$ .

The derivative of the distribution function

$$f_x(x) = \frac{dF_x(x)}{dx} \quad (2.39)$$

is called the density function. The area under the density function curve between  $x_1$  and  $x_2$  is the probability that  $x$  lies between  $x_1$  and  $x_2$ .

### 2.2.1 Important Distribution

A random variable  $\mathbf{x}$  has a Gaussian - or normal- distribution if its density function is of the form

$$f(x) = \frac{1}{\sigma\sqrt{2\pi}} \exp(-(x-\mu)^2/2\sigma^2) \quad (2.40)$$

where  $\mu$  is the mean of  $\mathbf{x}$  and  $\sigma$  is the standard deviation.

A random variable  $\mathbf{x}$  has a binomial distribution of order  $n$  if  $\mathbf{x}$  can take the values  $0, 1, \dots, n$  and the probability that  $\mathbf{x} = k$  is given by

$$P(x=k) = \binom{n}{k} p^k q^{n-k} \quad p+q=1. \quad (2.41)$$

The probability density of a binomial random variable is

$$f(x) = \sum_{k=0}^n \binom{n}{k} p^k q^{n-k} \delta(x-k) \quad (2.42)$$

The Poisson distribution is the limit of the binomial distribution with only two outcomes (i.e. the distribution of flipping a fair coin) for a large number of

trials  $k$  that have a small probability  $p$ . The probability that  $k$  events occur in a time interval  $\tau$  is given by (52)

$$P_k(\tau) = \frac{\exp^{-\lambda\tau}(k\tau)^k}{k!}. \quad (2.43)$$

The parameter  $\lambda$  can be interpreted as the density of points, or the average number of events that happen per unit time. The probability density function of a Poisson random variable is

$$f(x) = \lambda \exp^{-\lambda x} U(x) \quad (2.44)$$

and is called "exponential".

### 2.2.2 Mean and Variance

The mean, or expectation value of a random variable is given by the following integral:

$$E\{\mathbf{x}\} = \int_{-\infty}^{\infty} x f(x) dx \quad (2.45)$$

where  $f(x)$  is the density function of the random variable. The mean will be denoted by  $\mu_x$  or  $\mu$ . The variance of a random variable is given by a similar integral,

$$E\{(\mathbf{x} - \mu_x)^2\} = \int_{-\infty}^{\infty} (x - \mu_x)^2 f(x) dx = \sigma^2 \quad (2.46)$$

From this definition, it can be seen that

$$\sigma^2 = E\{\mathbf{x}^2\} - E^2\{\mathbf{x}\} \quad (2.47)$$

For any distribution, the mean,  $\mu$  can be estimated from

$$\hat{\mu} = \frac{1}{N} \sum_{n=1}^N x_n \quad (2.48)$$

The expectation value of  $\hat{\mu}$  is

$$E\{\hat{\mu}\} = \frac{1}{N} \sum_{n=1}^N E\{x_n\} = \frac{1}{N} N\mu = \mu \quad (2.49)$$

so Equation 2.48 is known as an unbiased estimator of  $\mu$ .

The variance,  $\sigma^2$  can be estimated from

$$\hat{\sigma}^2 = \frac{1}{N-1} \sum_{n=1}^N (x_n - \hat{\mu})^2 \quad (2.50)$$

The expectation value of Equation 2.50 is  $\sigma^2$  so it too is an unbiased estimator.

### 2.2.3 Independence

A pair of random variable  $\mathbf{x}$  and  $\mathbf{y}$  with probability density functions  $f_x(x)$  and  $f_y(y)$  are statistically independent if the joint probability density function  $f(x, y)$  is equal to the product of the two independent probability functions

$$f(x, y) = f_x(x)f_y(y) \quad (2.51)$$

This means that the probability of  $\mathbf{x}$  is not effected by  $\mathbf{y}$  and vice versa. For a set of independent Gaussian random variables  $\mathbf{x}_n$ , the variance of the sum is equal to the sum of the variances (52–54)

$$\mathbf{s} = \sum \mathbf{x}_n \quad (2.52)$$

$$\sigma_s^2 = \sum \sigma_n^2$$

#### 2.2.4 Random Processes

A stochastic, or random, process is "a rule for assigning to every  $\xi$  a function  $\mathbf{x}(t, \xi)$ ." (52) (see the definition of a random variable, 2.2) The random process can be thought of as a collection, or ensemble, of time functions, one for each  $\xi$ . An example of a random process is the voltage, as a function of time, measured across a resistor with its ends grounded. The voltage can be measured as a function of time, and the experiment repeated over again. Each repetition of the experiment represents a unique  $\xi$ , or sample of the random process.

A random process can also be considered to be of as a collection of random variables  $\mathbf{x}(t)$ , one for each time  $t$ . Like random variables, there exists a distribution function

$$F(x, t) = P\{\mathbf{x} \leq x\} \quad (2.53)$$

for each specific  $t$ . In addition, there exists the derivative of this distribution function,

$$f(x, t) = \frac{\partial F(x, t)}{\partial x} \quad (2.54)$$

if  $F(x, t)$  is differentiable.

The mean  $\mu(t)$  of the random variable  $\mathbf{x}(t)$  is given by the expectation value

$$E\{\mathbf{x}(t)\} = \int_{-\infty}^{\infty} x f(x, t) dx = \mu_x(t) \quad (2.55)$$

The autocorrelation  $R(t_1, t_2)$  is the expected value of  $\mathbf{x}(t_1)\mathbf{x}(t_2)$ , given by

$$E\{\mathbf{x}(t_1)\mathbf{x}(t_2)\} = \int_{-\infty}^{\infty} \int_{-\infty}^{\infty} x_1 x_2 f(x_1, x_2; t_1, t_2) dx_1 dx_2 \quad (2.56)$$

The autocorrelation evaluated at  $t_1 = t_2 = t$  is  $E\{\mathbf{x}^2(t)\}$ , which is the average power of  $\mathbf{x}(t)$ .

Similarly, the autocovariance  $C(t_1, t_2)$  of  $\mathbf{x}(t)$  is the expected value

$$C(t_1, t_2) = E[(\mathbf{x}(t_1) - \mu(t_1))(\mathbf{x}(t_2) - \mu(t_2))]. \quad (2.57)$$

Because the expectation operator is linear,  $\mu(t_1)$  and  $\mu(t_2)$  can be moved out of the integral, and the autocovariance can be written in terms of the autocorrelation.

$$C(t_1, t_2) = R(t_1, t_2) - \mu(t_1)\mu(t_2) \quad (2.58)$$

The autocovariance evaluated at  $t_1 = t_2 = t$  is  $E\{(\mathbf{x}(t) - \mu(t))^2\}$ , which is the variance  $\sigma^2(t)$  of  $\mathbf{x}(t)$ . The autocovariance will be used in Chapter 3 to determine the theoretical output variance of a CTIA with various stochastic inputs.

#### 2.2.4.a Stationary Processes

According to Papoulis, "a stochastic process  $\mathbf{x}(t)$  is called *strict-sense stationary* (abbreviated SSS) if its statistical properties are invariant to a shift in the origin. This means that the processes  $\mathbf{x}(t)$  and  $\mathbf{x}(t + c)$  have the same statistics for any  $c$ "(52). If the mean of a stochastic process  $\mathbf{x}(t)$  is constant

$$E\{\mathbf{x}\} = \mu_x \quad (2.59)$$

and its autocorrelation only depends on the time difference  $\tau = t_1 - t_2$

$$E\mathbf{x}(t + \tau)\mathbf{x}^*(t) = R(\tau) \quad (2.60)$$

then  $\mathbf{x}$  is known as a *wide-sense stationary* process (52). While an SSS process is guaranteed to be WSS, the converse is not generally true. An exception is that WSS Gaussian processes are also SSS (52).

#### 2.2.4.b Poisson Processes

Arrival events, such as ion or electron flow, can be modeled by a special kind of random process, known as a Poisson process. Events occur continuously and statistically independently from each other in a Poisson process. A Poisson process can be thought of as a collection of  $N$  points ( $N \gg 1$ ) randomly distributed over a time  $T$ . If each point is at a time  $t_n$  and if the distances  $\mathbf{w}_n$  between consecutive points are independent and exponentially distributed (2.44) then the process formed by the points is a Poisson process (52). An important property of the Poisson process that will be used in Chapter 3 is that both the mean and the variance of the process are equal to  $\lambda$  (52).

#### 2.2.4.c Power Spectral Densities

The Fourier transform of the autocorrelation of a WSS random process  $\mathbf{x}$  is the power spectrum, or power spectral density (PSD) of the process (52, 55)

$$P_x(j\omega) = \int_{-\infty}^{\infty} R(\tau) \exp^{-j\omega\tau} d\tau. \quad (2.61)$$

The power spectral density has a number of useful properties. The PSD of a real valued WSS random process is also real and even (52, 55)

$$P_x(j\omega) = P_x(-j\omega). \quad (2.62)$$

In addition, the PSD of a WSS random process is always non-negative.

### 2.3 Linear Least Squares

Because the output of a CTIA is the integral of the input current, and the current is typically the signal of interest, the derivative of the output signal must be computed. Because the input current is typically constant, the derivative of the output can be estimated using a least squares slope estimator. There are two types of least squares estimators used in this dissertation: the ordinary least squares (OLS) slope estimator and the generalized least squares (GLS) slope estimator. As explained below, the OLS slope estimator assumes the errors in the measurements used to estimate the slope have a constant standard deviation for all measurements, while the GLS slope estimator does not.

#### 2.3.1 Ordinary Least Squares Slope Estimator

The following derivation follows that in Fox (56). A general linear model with one dependent variable and two unknown parameters is given by the equation

$$y_i = \beta_0 + \beta_1 x_i + \epsilon_i \quad (2.63)$$

where  $y_i$  is the dependent variable (the measured output signal),  $x_i$  is the independent variable (typically time),  $\beta_0$  and  $\beta_1$  are the true slope and intercept, and  $\epsilon_i$  is a random error representing noise. This equation can be expressed in vector form by collecting the dependent variables  $x_i$  into a row vector with a 1 at the beginning and collecting the parameters  $\beta_0$  and  $\beta_1$  into a column vector as follows:

$$y_i = [1, x_i] \begin{bmatrix} \beta_0 \\ \beta_1 \end{bmatrix} + \epsilon_i \quad (2.64)$$

If there are  $n$  samples of  $y$  there are  $n$  such equations, and they can be collected into a single matrix equation:

$$\begin{bmatrix} y_0 \\ y_1 \\ \vdots \\ y_{n-1} \end{bmatrix} = \begin{bmatrix} 1 & x_0 \\ 1 & x_1 \\ \vdots & \vdots \\ 1 & x_{n-1} \end{bmatrix} \begin{bmatrix} \beta_0 \\ \beta_1 \end{bmatrix} + \begin{bmatrix} \epsilon_0 \\ \epsilon_1 \\ \vdots \\ \epsilon_{n-1} \end{bmatrix} \quad (2.65)$$

$$\mathbf{y}_{[n \times 1]} = \mathbf{X}_{[n \times 2]} \boldsymbol{\beta}_{[2 \times 1]} + \boldsymbol{\epsilon}_{[n \times 1]} \quad (2.66)$$

Assuming  $\boldsymbol{\epsilon}$  is normally distributed with zero mean, the expectation of  $\mathbf{y}$  is:

$$E[\mathbf{y}] = E[\mathbf{X}\boldsymbol{\beta} + \boldsymbol{\epsilon}] \quad (2.67)$$

$$= E[\mathbf{X}\boldsymbol{\beta}] + E[\boldsymbol{\epsilon}] \quad (2.68)$$

$$= \mathbf{X}\boldsymbol{\beta} \quad (2.69)$$

because  $\mathbf{X}\boldsymbol{\beta}$  is a constant vector and  $E[\boldsymbol{\epsilon}] = 0$  by assumption.

The fitted linear model can be written as:

$$\mathbf{y} = \mathbf{X}\mathbf{b} + \mathbf{e} \quad (2.70)$$

where  $\mathbf{b} = \hat{\beta}$  and  $\mathbf{e} = [E_0, E_1, \dots, E_{n-1}]$  is the vector of the errors. Here, the  $\hat{\cdot}$  symbol indicates an estimate:  $\hat{\beta}$  is an estimate of  $\beta$ . The least squares estimate  $\mathbf{b}$  is the vector that minimizes the sum of the squares of the errors as a function of  $\mathbf{b}$ :

$$S(\mathbf{b}) = \mathbf{e}^T \mathbf{e} = (\mathbf{y} - \mathbf{X}\mathbf{b})^T (\mathbf{y} - \mathbf{X}\mathbf{b}) \quad (2.71)$$

$$= \mathbf{y}^T \mathbf{y} - \mathbf{y}^T \mathbf{X}\mathbf{b} - (\mathbf{X}\mathbf{b})^T \mathbf{y} + \mathbf{b}^T \mathbf{X}^T \mathbf{X}\mathbf{b} \quad (2.72)$$

$$= \mathbf{y}^T \mathbf{y} - (2\mathbf{y}^T \mathbf{X})\mathbf{b} + \mathbf{b}^T (\mathbf{X}^T \mathbf{X})\mathbf{b} \quad (2.73)$$

Recognizing that  $[(\mathbf{X}\mathbf{b})^T \mathbf{y}]^T = \mathbf{y}^T (\mathbf{X}\mathbf{b})$  and that since each term in Equation 2.72 is  $[1 \times 1]$ ,

$$(\mathbf{X}\mathbf{b})^T \mathbf{y} = [(\mathbf{X}\mathbf{b})^T \mathbf{y}]^T = \mathbf{y}^T \mathbf{X}\mathbf{b} \quad (2.74)$$

The linear least squares estimator depends on a few key assumptions:

- *Linearity.* The expectation value of the error at each point  $x_i$  is zero, that is  $E\{\epsilon_i\} = 0$ . This means that the expectation value of  $y_i$  is  $\beta_0 + \beta_1 x_i$ .
- *Constant Variance.* The variances of the errors  $\epsilon_i$  are the same for all  $i$ .
- *Independence.* The observations  $y_i$  are sampled independently (see Section 2.2.3), so that any pair of errors  $\epsilon_i$  and  $\epsilon_j$  are statistically independent for  $i \neq j$ .

- *Normality* The errors  $\epsilon$  are normally (Gaussian) distributed (2.2).

The OLS slope estimator has a number of properties that make it useful. First of all, the slope estimate is unbiased, which mean that the expectation value of the estimate of a parameter,  $\hat{\beta}$ , is the same as the expectation of the parameter,  $\beta$  (56–58). Another important property of the OLS estimator is that if the first three assumptions are meet the estimator is the most efficient unbiased linear estimator (BLUE) (56–58). The efficiency of an estimator is the rate at which the variance of the estimator decreases as the number of samples increases (56–60). If the errors are normally distributed, the OLS estimator is the most efficient estimator out of all estimators, linear or non-linear (56–58).

The parameter vector  $\beta$  can be estimated as follows:

$$\mathbf{b} = \hat{\beta} = (\mathbf{X}^T \mathbf{X})^{-1} \mathbf{X}^T \mathbf{y} \quad (2.75)$$

The variance of the errors ( $\sigma_\epsilon^2$ ) can be estimated from the residuals as follows (56):

$$\hat{\sigma}_\epsilon^2 = s_E^2 = \frac{\mathbf{e}^T \mathbf{e}}{n - 2} \quad (2.76)$$

The variance of the estimated parameters  $\mathbf{b}$  can then be estimated using this variance:

$$\hat{V}(\mathbf{b}) = s_E^2 (\mathbf{X}^T \mathbf{X})^{-1} = \frac{\mathbf{e}^T \mathbf{e}}{n - 2} (\mathbf{X}^T \mathbf{X})^{-1} \quad (2.77)$$

For a linear regression model,  $\mathbf{X}^T \mathbf{X}$  is a  $[2 \times 2]$  matrix, so the variance of the slope

parameter is related to the second diagonal entry of  $\mathbf{X}^T\mathbf{X}$ , which evaluates to:

$$[\mathbf{X}^T\mathbf{X}]_{2,2} = S_{xx} = \sum(x_i - \bar{x})^2 = \sum x_i^2 - \frac{(\sum x_i)^2}{n}. \quad (2.78)$$

This is effectively a measure of how spread out the data points used to perform the estimate are: the larger the spread the better the estimate  $\mathbf{b}$ .

### 2.3.2 Generalized Least Squares Slope Estimator

As discussed in Chapter 3, the noise on the output of a CTIA, and thus the standard deviation of the errors, increases with time. Therefore, the assumption of constant error variance is violated. In this case, the best linear unbiased estimator is the generalized least squares (GLS) estimator (56, 61).

The parameter vector  $\boldsymbol{\beta}$  can be estimated using GLS as follows (56, 61):

$$\mathbf{b} = \hat{\boldsymbol{\beta}} = (\mathbf{X}^T \Sigma^{-1} \mathbf{X})^{-1} \Sigma^{-1} \mathbf{X}^T \mathbf{y} \quad (2.79)$$

where

$$\Sigma = \begin{bmatrix} \sigma_0^2 & 0 & \cdots & 0 \\ 0 & \sigma_1^2 & \cdots & 0 \\ \vdots & \vdots & \ddots & \vdots \\ 0 & 0 & \cdots & \sigma_{N-1}^2 \end{bmatrix} \quad (2.80)$$

and  $\sigma_i^2$  is the variance of the error  $\epsilon_i$  at  $x_i$ .

In general the parameter  $\sigma_i^2$  is unknown, so it is difficult to compute the GLS estimation of the parameter vector  $\mathbf{b}$ . Therefore, most slope estimations in this dissertation were computed using an OLS slope estimator. However, the GLS estimator

was used in conjunction with characterized noises to predict amplifier performance in Chapter 3.

## 2.4 Noise

Noise plays an important role in the measurement of signals. Noise consists of all extra signals, be they random or not, that are measured in addition to the signal of interest. Fixed noise, such as non-fluctuating backgrounds, can be easily eliminated, while random noise, due to its statistical nature, is harder to remove. These random fluctuations set the ultimate limit on the statistical confidence of a particular measurement. In chemistry, the "limit of detection" (LOD) is usually defined as the amount of sample that gives a signal with an intensity equal to three times the standard deviation of the noise. The "limit of quantitation" (LOQ) is similarly defined as the amount of sample that gives a signal with an intensity equal to ten times the standard deviation of the noise. Random noise can be viewed in either the time domain or the frequency domain. In the time domain, noise can be reported as the peak-to-peak value of fluctuations, or as the square root of mean of the squares (RMS) of the samples of a signal. In much of the statistical noise literature, noise processes are assumed to have zero-mean, for mathematical simplicity. Noise processes with non-zero mean can be modeled as a zero-mean noise process plus a non-random offset. Because the standard deviation of a zero mean random process is equal to the RMS, time domain noise can also be measured as the

standard deviation of the samples of a signal. In the frequency domain it is viewed as a power density, typically with units of volts squared per hertz.

Noise is often described by its shape in the frequency domain, as well as its source of origin. Noise with a power spectral density that has no frequency dependence is referred to as "white" noise. If the noise power density is a function of one over the frequency, it is referred to as  $1/f$  noise, "pink" noise, or "flicker" noise. Because the power spectrum is the Fourier transform of the autocorrelation, the autocorrelation of a stationary white noise process will be a delta function multiplied by the variance of that process, since a constant and a delta function are a Fourier transform pair.

#### 2.4.1 Thermal Noise

Thermal noise, also known as Johnson noise, comes from fluctuations in charge carriers due to thermal motion inside a resistor or conductor at equilibrium (62, 63).

The one-sided power spectral density of Johnson noise is

$$S_{nt}(j\omega) = 4kTR \quad (2.81)$$

where  $k$  is the Boltzmann constant in joules per Kelvin,  $T$  is the absolute temperature in Kelvin of the resistor, and  $R$  is the resistance in ohms. Because the power spectral density of thermal noise has no frequency dependence, it is "white" noise.

The RMS voltage from thermal noise is

$$v_{RMS} = \sqrt{4kTR\Delta f} \quad (2.82)$$

where  $\Delta f$  is the frequency bandwidth. By examining either Equation 2.81 or Equation 2.82 is it clear that one simple way to decrease the effect of thermal noise is to lower the temperature.

#### 2.4.1.a kT/C Noise

In the ideal case, a circuit containing a capacitor and a resistor exhibits thermal noise from the resistor and no noise from the capacitor. The thermal noise in the resistor is from random fluctuations of charge carriers, and has a spectral density of

$$S_{nt}(j\omega) = 4kTR$$

This thermal noise can come from a physical resistor, or as is the case with a capacitive transimpedance amplifier (CTIA), from the resistance of the reset FET channel. Because the spectral density of the thermal noise is white (frequency independent), the total noise measured is the square root of the spectral density multiplied by the bandwidth:

$$v_{no} = \sqrt{V_{nt}^2 \Delta f} = \sqrt{4kTR \Delta f} \quad (2.83)$$

The RC circuit acts as a low-pass filter, so the noise bandwidth is given by

$$\Delta f = \frac{1}{2\pi} \int_0^\infty \frac{d\omega}{1 + (\omega RC)^2} = \frac{1}{2\pi} \frac{\pi}{2RC} = \frac{1}{4RC} \quad (2.84)$$

Combining Equations 2.83 and 2.84 yields the expression

$$v_{no} = \sqrt{\frac{kT}{C}} \quad (2.85)$$

for the thermal noise. This noise is thermal noise from the resistance that is distributed across the capacitor. In the case of a CTIA, this noise is manifest as a random offset voltage on the output of the amplifier when the reset FET opens.

#### 2.4.2 Shot Noise

Shot noise arises from random fluctuations in the number of charged particles crossing a barrier or arriving at an electrode (62, 63). Shot noise processes are well modeled by a Poisson random process (52). The one-sided power spectral density of shot noise is

$$S_{ns}(j\omega) = 2i_s e \quad (2.86)$$

where  $i_s$  is the current and  $e$  is the elementary charge. The power spectral density of shot noise has no frequency dependence, so, like thermal noise, shot noise is white. The RMS current from shot noise is

$$i_{RMS} = \sqrt{2i_s e \Delta f} \quad (2.87)$$

where all symbols are the same as defined above.

#### 2.4.3 Flicker Noise

Another source of noise associated is flicker noise, also known as 1/f noise because its power spectrum has a  $1/f^n$  dependence, where  $n$  is close to one (62–64). It is also known as excess noise because it is noise in addition to the expected thermal and shot noise. While there is not yet a unified model for 1/f noise in metal-oxide

semiconductor field effect transistors (MOSFETs), it is generally accepted that  $n$  is dependent on the technology used for device fabrication (64).

#### 2.4.4 Fixed Pattern Noise

Another type of noise specific to imaging detectors is fixed pattern noise (FPN). Fixed pattern noise arises from differences in gain between pixels (63). Since this noise is dependent on the gain non-uniformity, it is proportional to signal level. For devices that behave linearly, FPN can be reduced through a technique known as "flat fielding", where the output of each pixel is adjusted to account for gain non-uniformity (63). In order to properly flat field an imaging detector, the gain of each pixel must be accurately and precisely measured, usually by providing uniform ("flat") illumination to all the pixels in the array.

## CHAPTER 3

### LINEAR MODELS OF A CAPACITIVE TRANSIMPEDANCE AMPLIFIER

This chapter will present a linear model of the capacitive transimpedance amplifier (CTIA). A linear systems model is used because it can be derived in closed form and reflects the behavior of a ideal CTIA. Built upon theories of random variables and processes (see Chapter 2.2), this linear model will be used to determine the output variance of an ideal CTIA given various types of input noise. These output variances will then be used to derive signal-to-noise equations as well as limit of detection equations based on the model parameters. These equations will suggest the optimal method for measuring the output of the CTIA, as well as the influence of various parameters on the ultimate sensitivity of the amplifier. Improvements to these parameters, i.e. read and dark current noise, in future generations of CTIAs will help improve sensitivity towards the goal of single ion detection.

#### 3.1 Signal-to-Noise Models

Each individual detector amplifier in an array can be modeled using the circuit shown in Figure (3.1a). Signal current, represented by the current source  $i_s$ , is integrated on the feedback capacitor  $C_f$  and  $C_g$  models input capacitance. The amplifier has an open-loop transfer function  $G(s)$ . The open-loop transfer function of the

amplifier represents how a voltage difference between the two inputs is converted to an output voltage by the amplifier in the absence of feedback. Current source  $i_n$  and voltage source  $e_n$  represent the input current noise and voltage noise of the amplifier respectively. There is a matched pair of FETs in the feedback loop to reset the device as well as another matched pair of FETs to switch gains, but these do not appear to have a significant effect on operation.

### 3.1.1 System Output with Deterministic Inputs

Because this is a linear model, the superposition principle applies. The superposition principle states that the output of a system from multiple inputs is equal to the sum of the outputs of the system from each individual input (49, 65). As explained in Chapter 2.1.2, analysis of linear systems is often easier to carry out in the s domain. Figure 3.1b shows the model in the s domain. Capital letters for current and voltage sources represent Laplace transforms of the time domain sources. The impedance of a resistor is its resistance  $R$ . The impedance of a capacitor is  $\frac{1}{sC}$ . The circuit model in the s domain with all sources removed except the signal  $i_s$  is shown in Figure 3.2b.

Applying Kirchhoff's current law to node  $a$  and assuming the amplifier has infinite input impedance results in the following equation:

$$I_s(s) + sC_g [V_g(s) - V_a(s)] + sC_f [V_o(s) - V_a(s)] = 0 \quad (3.1)$$

where  $V_g(s)$  is the voltage at node  $g$  and  $V_a(s)$  is the voltage at node  $a$ . Assuming

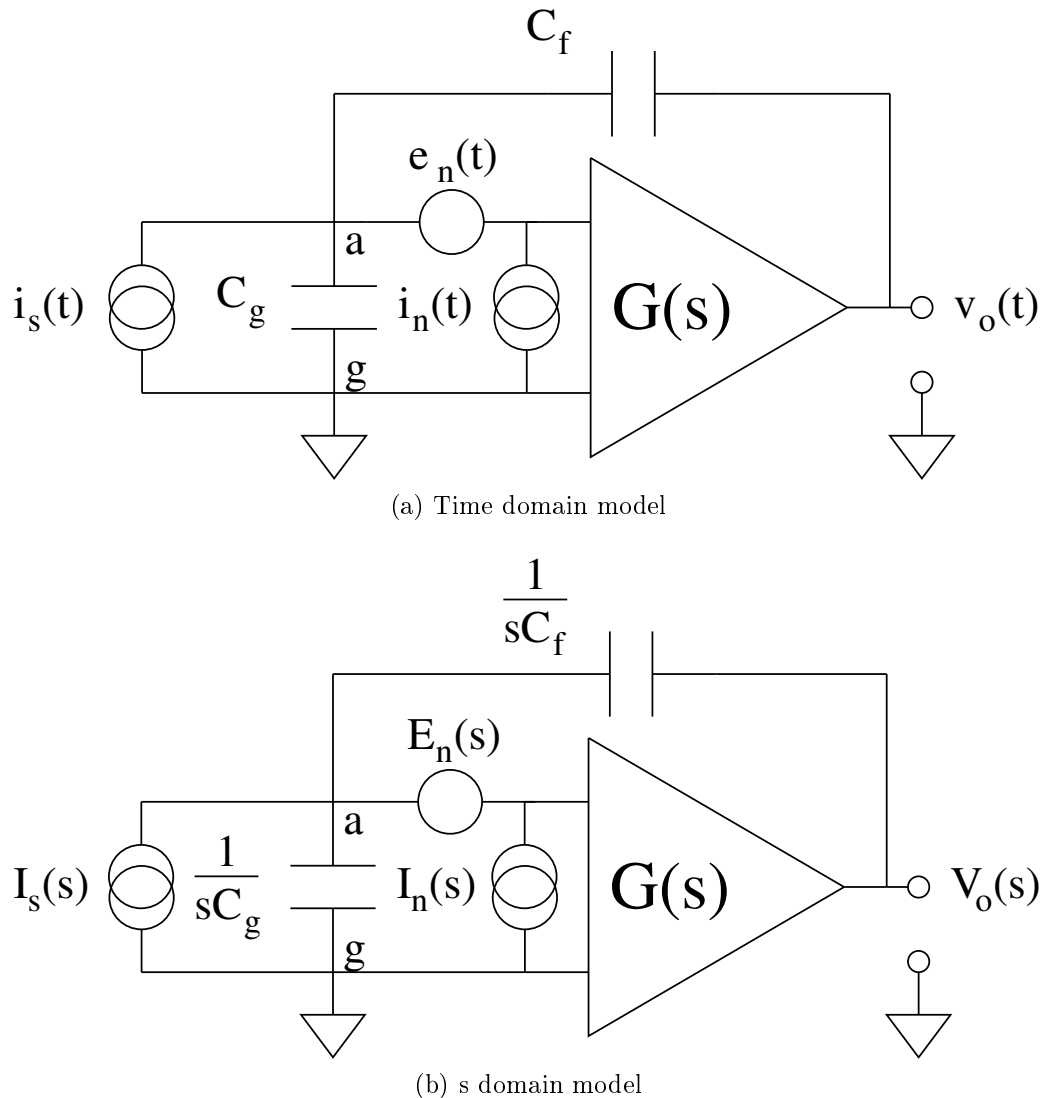


Figure 3.1: Linear models of the CTIA detector.

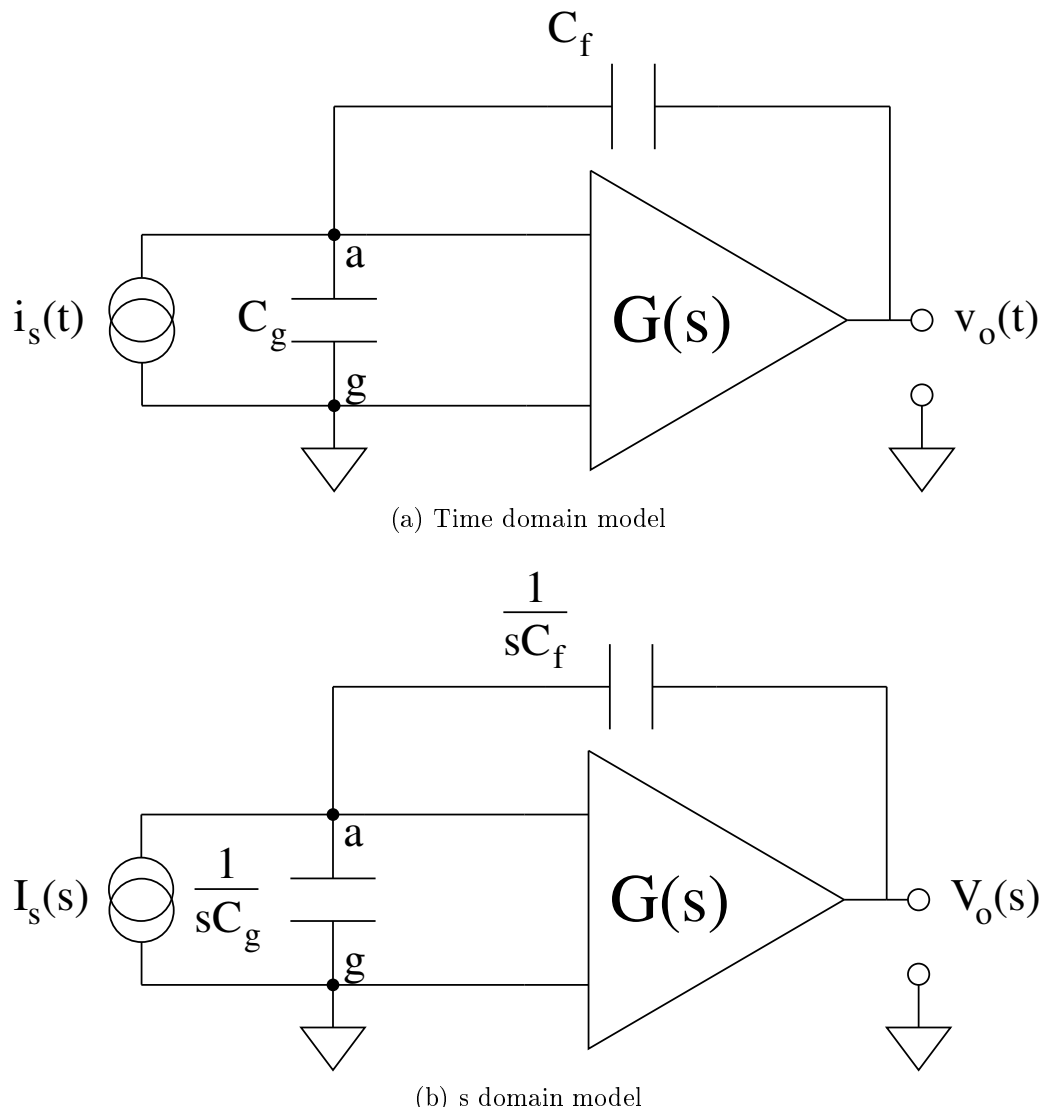


Figure 3.2: Linear model with only the source current present.

the amplifier has infinite open-loop gain so the amplifier drives the voltage difference at its input terminals to zero,  $V_a(s) = V_g(s) = 0$ . Rearranging and solving for  $\frac{V_o(s)}{I_s(s)}$  yields the transfer function for input currents.

$$H_i(s) = \frac{V_o(s)}{I_s(s)} = -\frac{1}{C_f s} \quad (3.2)$$

Taking the inverse Laplace transform of Equation 3.2 gives the impulse response function:

$$h_i(t) = -\frac{1}{C_f} U(t) \quad (3.3)$$

where  $U(t)$  is the unit step function (see Chapter 2.1). The units of this impulse response function are volts per coulomb. This impulse response function will be used to determine the output of a CTIA to an input current, as well as the noise on the output of a CTIA due to input current noise.

### 3.1.1.a Effect of Feedback

An ideal amplifier, like the one shown in Figure 3.2, operates by amplifying the voltage difference between its two inputs by an amplification factor known as its open-loop gain: the gain of the amplifier in the absence of feedback. Ideal amplifiers have infinite open-loop gain ( $G(s) = \infty$ ), whereas the gain of real amplifiers is finite and varies with frequency, temperature, and other factors (66). For the amplifier in Figure 3.2, the output voltage is

$$v_o(t) = a v_\epsilon(t) \quad (3.4)$$

where  $a$  is the open-loop gain and  $v_\epsilon(t)$  is the difference in voltage between the two inputs

$$v_\epsilon(t) = v_a(t) - v_g(t). \quad (3.5)$$

Connecting the output to one of the inputs via a feedback element adds a voltage to that input that is the output voltage attenuated by the feedback element, so the output voltage is

$$v_o(t) = a \left( v_i(t) - \frac{v_o(t)}{Z} \right) \quad (3.6)$$

where  $v_i(t)$  is the input voltage difference and  $Z$  is the impedance of the feedback element. Rearranging Equation 3.6 and solving for the output voltage divided by the input voltage gives

$$\frac{v_o(t)}{v_i(t)} = A = \frac{a}{1 + \frac{a}{z}} \quad (3.7)$$

where  $A$  is known as the closed-loop gain. Because the open-loop gain  $a$  of a real amplifier is not constant, the addition of feedback serves to linearize the amplifier output by reducing the dependence of the output voltage on the amplifier open-loop gain. If  $a/Z \gg 1$ , Equation 3.7 reduces to

$$\frac{v_o(t)}{v_i(t)} = A \approx Z \quad (3.8)$$

which depends only on the feedback element. Because the feedback element is typically a passive component like a resistor or capacitor, its impedance is stable, and thus the closed-loop gain of an amplifier with feedback is stable.

### 3.1.2 System Output with Stochastic Inputs

In reality, the inputs to the CTIA are stochastic in nature. The output random process of an LTI system with a random process as its input can be calculated using expectation values. Because expectation is a linear operator, and the LTI system is also a linear operator, the expectation can be moved inside the LTI operator:

$$E\{L[x(t)]\} = L[E\{x(t)\}] . \quad (3.9)$$

The result of this is that the expectation of the output of the LTI system is equal to the output of the LTI system with the expectation of the input random process as its input:

$$E\{y(t)\} = \mu_y = L[E\{x(t)\}] . = L[\mu_x] \quad (3.10)$$

#### 3.1.2.a Output voltage from a random current on the input

Recalling Chapter 2.1, the output of a linear, time-invariant (LTI) system with impulse response  $h(t)$  from an input  $x(t)$  can be calculated from the convolution integral:

$$y(t) = x(t) * h(t) = \int_{-\infty}^{\infty} x(\tau)h(t - \tau) d\tau = \int_{-\infty}^{\infty} x(t - \tau)h(\tau) d\tau . \quad (3.11)$$

The output voltage for a given input current can be calculated from the following convolution integral:

$$v_o(t) = i_s(t) * h(t) = \int_{-\infty}^{\infty} i_s(\tau)h(t - \tau) d\tau . \quad (3.12)$$

The input current is assumed to be a wide-sense stationary (WSS) random process, with mean  $i_{in}$  and variance  $\sigma_i^2$ . The autocovariance ( $C_{xx}$ ) of a WSS process with variance  $\sigma_i^2$  is (52):

$$C_{xx}(t, t) = \sigma_i^2 \delta(t) \quad (3.13)$$

Using Equation 3.10, the mean output of the CTIA in response to this input random process can be computed by using the mean  $i_{in}$  as the input. The CTIA is an integrator with a reset switch, so the integration has a start time  $t = 0$ , and the input random process can be represented by  $i_s(t) = i_{in}U(t)$ . Substituting this into Equation 3.12 and using Equation 3.3 gives:

$$v_o(t) = -\frac{i_{in}}{C_f} t U(t). \quad (3.14)$$

As expected, the output voltage is just the time integral of the input current.

### 3.1.2.b Output variance from a random current on the input

Computing the autocorrelation of the output random process ( $R_{yy}$ ) directly is challenging, so it is easier instead to first compute the cross correlation  $R_{xy}$ :

$$R_{xy}(t_1, t_2) = L_2 [R_{xx}(t_1, t_2)] \quad (3.15)$$

Using the notation in Papoulis, “ $L_2[\cdot]$  means the system operates on the variable  $t_2$ , treating  $t_1$  as a parameter.”(52) Using Equation 3.11 to evaluate Equation 3.15 yields:

$$R_{xy}(t_1, t_2) = \int_{-\infty}^{\infty} R_{xx}(t_1, t_2 - \tau) h(\tau) d\tau. \quad (3.16)$$

The autocorrelation of the output can be calculated from this cross correlation as:

$$R_{yy}(t_1, t_2) = L_1[R_{xy}(t_1, t_2)] . \quad (3.17)$$

This means that:

$$R_{yy}(t_1, t_2) = \int_{-\infty}^{\infty} R_{xy}(t_1 - \tau, t_2) h(\tau) d\tau . \quad (3.18)$$

In addition, the output autocovariance ( $C_{yy}$ ) is related to the input autocovariance ( $C_{xx}$ ) by the same relationship.

$$C_{xy}(t_1, t_2) = C_{xx}(t_1, t_2) * h(t_2) \quad (3.19)$$

$$C_{yy}(t_1, t_2) = C_{xy}(t_1, t_2) * h(t_1) \quad (3.20)$$

Continuing with the input random process from above, the variance is  $\sigma_i^2$  so the autocovariance is:

$$C_{xx}(t, t) = \sigma_i^2 \delta(t) \quad (3.21)$$

Substituting Equation 3.21 into Equation 3.20 and noting that  $t_1 = t_2 = t$  gives:

$$C_{xy}(t, t) = (\sigma_i^2 \delta(t)) * \left( -\frac{1}{C_f} U(t) \right) . \quad (3.22)$$

Recognizing that the convolution of a function with  $\delta(t)$  is just the function evaluated at  $t$  gives:

$$C_{xy}(t, t) = -\frac{\sigma_i^2}{C_f} U(t) . \quad (3.23)$$

Substituting this result into 3.20 yields

$$\begin{aligned} C_{yy}(t, t) &= \left( -\frac{\sigma_i^2}{C_f} U(t) \right) * \left( -\frac{1}{C_f} U(t) \right) \\ &= \frac{\sigma_i^2}{C_f^2} \int_{-\infty}^{\infty} U(t - \alpha) U(\alpha) d\alpha . \end{aligned} \quad (3.24)$$

The first unit step function,  $U(t - \alpha)$ , is zero for  $\alpha > t$ , so the upper limit of integration is  $t$ . The second unit step function,  $U(\alpha)$ , is zero for  $\alpha < 0$  so the lower limit of integration is 0. Equation 3.25 reduced to the output variance (see Chapter 2.2):

$$C_{yy}(t, t) = \sigma_y^2(t) = \frac{\sigma_i^2}{C_f^2} t. \quad (3.25)$$

Recognizing that the current gain (from the current impulse response described by Equation 3.3) is  $-1/C_f$ , the output variance is equal to the input variance multiplied by the gain squared multiplied by time.

### 3.1.2.c Output Voltage and Variance from a Random Voltage Noise on the Input

The output voltage and variance due to a random input voltage can be computed in the same manner as in Sections 3.1.2.a and 3.1.2.b. The derivations themselves are presented in Appendix A and only the results are presented here. The output voltage  $v_o(t)$  due to an input voltage  $e_n(t)$  is given by the convolution integral:

$$v_o(t) = e_n(t) * \frac{C_f + C_g}{C_f} \delta(t) \quad (3.26)$$

where the closed-loop (with feedback) impulse response function for voltage is:

$$h_v(t) = \frac{C_f + C_g}{C_f} \delta(t) \quad (3.27)$$

and the closed-loop transfer function for voltage is:

$$H_v(s) = \frac{V_o(s)}{E_n(s)} = \frac{C_f + C_g}{C_f}. \quad (3.28)$$

Assuming  $e_n(t)$  is a zero-mean, stationary, white random process with variance  $\sigma_\nu^2$ , the output autocovariance due to  $e_n(t)$  is given by:

$$C_{yy}(t, t) = \sigma_y^2(t) = \frac{(C_f + C_g)^2}{C_f^2} \sigma_\nu^2 \quad (3.29)$$

### 3.2 Mean-Variance for Gain Characterization

Gain characterization for large array detectors would be tedious if each element in the array had to be characterized independently. The gain of each element in an array detectors could be measured by using a previously characterized uniform source illuminating all elements simultaneously and equally, but such a source is difficult to construct, as well. One method for characterization of the gain of array detectors that circumvents these problems is "mean-variance analysis" (67, 68). In mean-variance analysis, the detector is illuminated with a shot noise limited source. Because shot noise is Poisson distributed, the variance of the shot noise signal source is equal to the mean in units of counts. By comparing the mean and variance at the detector output, the gain of the detector can be determined.

Sperline et al. present a derivation of the equations for mean-variance analysis based on propagation of errors (67), but this derivation makes the assumption that the gain for current noise is the same as for voltage noise. As seen in Section 3.1.2, this is not correct. A more rigorous derivation from statistical principals and linear systems theory will be presented here.

In addition to determining the gains of the system, another piece of information

obtained from mean-variance analysis is the output voltage noise, also called the read-noise. Frequently, the output read-noise is related back to the input using the gain, but this is problematic for two reasons. First, not all of the voltage noise on the output comes from voltage noise on the input; some of it comes from the output stage of the amplifier. Second, as seen in Equation 3.29, the voltage gain depends on  $C_g$ , the capacitance to ground on the input. This parameter is in general difficult to measure, so it is difficult to determine the proper gain to refer output voltage noise back to input voltage noise. In general, then, it is best to consider the voltage noise on these amplifiers at the output, rather than the input. Because output voltage noises is frequently referred back to the input using the current gain, this will be done later in this dissertation.

### 3.2.1 Output Variance from Shot Noise on the Input

From Chapter 2.2.4.b, the mean ( $\mu$ ) and the variance ( $\sigma^2$ ) of a Poisson process are equal. Campbell's theorem can be used to compute the mean and variance of the output of a system with a shot noise process as its input as (52):

$$\mu_{sn} = \lambda \int_{-\infty}^{\infty} h(t) dt \quad (3.30)$$

$$\sigma_{sn}^2 = \lambda \int_{-\infty}^{\infty} h^2(t) dt. \quad (3.31)$$

The symbol  $\lambda$  in Equation 3.30 represents the average density of points in the Poisson process, so for electron or ion shot noise,  $\lambda$  will be in units of charge per second. In Equation 3.31  $\lambda$  represents the variance of the input, so for unit consistency must

be in charge squared per second. The impulse response calculated above was for input current in amps, or coulombs per second, and so must be converted to units of charge by multiplication by  $q$ , the number of coulombs per charge. The impulse response in units of volts per charge is:

$$h(t) = -\frac{q}{C_f}U(t) \quad (3.32)$$

Alternatively, the fraction  $-\frac{q}{C_f}$  can be set as the gain  $g$  in volts per charge, and the impulse response can be simplified to:

$$h(t) = gU(t) \quad (3.33)$$

If the input shot noise current has an average density of  $i_{sn}$  in charge per second and a variance of  $i_{sn}(1charge)$  in units of charge squared per second, then the variance on the output of a CTIA with a transfer function given by Equation 3.33 is:

$$\begin{aligned} \sigma_{sn}^2(t) &= \lambda \int_{-\infty}^{\infty} h^2(t) dt \\ &= i_{sn}(1charge) \int_{-\infty}^{\infty} [gU(t)]^2 dt \\ &= g^2 i_{sn} t (1charge) \\ &= \frac{q^2}{C_f^2} i_{sn} t (1charge) \end{aligned} \quad (3.34)$$

where the units of  $\sigma_{sn}^2(t)$  are in volts squared and the factor of  $(1charge)$  has been added for unit consistency.

The presence of the reset switch introduces post-reset noise when the device comes out of reset. This post-reset noise is a random offset voltage with variance

$\sigma_{PRV}^2$  on the output, so although it does not change during the course of a single integration, it changes from integration to integration. The total output variance as a function of time is then:

$$\sigma_{out}^2(t) = \sigma_{sn}^2(t) + \sigma_{rn}^2 + \sigma_{PRV}^2 \quad (3.35)$$

The random offset due to the post-reset voltage can be eliminated by subtracting the first data point of a given integration from subsequent points in that integration. Subtraction of the first data point completely eliminates the effect of the post-reset voltage because the post-reset voltage is fully correlated within a specific integration period. The read-noise in the first sample is fully uncorrelated with the read-noise in each subsequent sample. The variance of the difference between two uncorrelated random variables is the sum of the two variances, so the post-reset voltage free output variance is:

$$\begin{aligned} \sigma_{out,CDS}^2(t) &= \sigma_{sn}^2(t) + 2\sigma_{rn}^2 \\ &= g^2 i_{sn} t \text{ (1charge)} + 2\sigma_{rm}^2 \\ &= \frac{q^2}{C_f^2} i_{sn} t \text{ (1charge)} + 2\sigma_{rm}^2 \end{aligned} \quad (3.36)$$

From Equation 3.12, the output voltage as a function of time:

$$\begin{aligned} v_{out}(t) &= -\frac{qi_{sn}}{C_f} t \\ &= gi_{sn}t \end{aligned} \quad (3.37)$$

can be rearranged to eliminate time from the output variance equation to yield the

output variance as a function of the output voltage:

$$\begin{aligned}\sigma_{out}^2 &= -\frac{qv_{out}(t)}{C_f} + 2\sigma_{rn}^2 \\ &= gv_{out}(t) + 2\sigma_{rn}^2\end{aligned}\quad (3.38)$$

A experiment then consists of measuring many separate integrations of a shot noise limited ion signal and subtracting the first sample of each integration from all subsequent samples of that integration. The variance at a specific sample time is computed from the voltage values of each integration at that sample time. The mean at each sample time is computed in the same manner. A plot of variance vs mean will, according to Equation 3.38, be linear with a slope equal to the gain of the system in volts per charge, and an intercept equal to the twice the output read variance. These parameters can be estimated using linear least squares. While the intercept term can be theoretically decomposed into the input voltage variance and the square of the system gain for input voltages, there is not enough information to separate them in practice because the input capacitance  $C_g$  is generally unknown.

### 3.2.2 Effect of Additional Source Noise on Mean-Variance Analysis

An important assumption in the derivation of Equation 3.38 is that the mean of the current  $i_{sn}$  is constant throughout all repetitions of the integration used to calculate the variance. The variance of the output  $Y$  is the expectation:

$$Var(Y) = E[(Y - \mu_Y)^2] \quad (3.39)$$

If the mean is not the same for each repetition, it is not completely subtracted out in the variance calculation. Thinking about it geometrically, if the mean input current is the same each time, each integration falls basically along the same line, with some variance due to random fluctuations in charge arrival, but if the source used is not stable, there is a different mean current for each integration. Because the CTIA acts as a current integrator, each integration will have a different expected mean slope. Because the output voltage as a function of time is linearly related to the slope, the spread in output values as a function of time gets larger linearly with time. Because the variance is the square of the difference of the output and the mean, the variance will increase quadratically with time if the mean current is not the same for all integrations. This means that the stability of the source used for the mean-variance measurements is of the utmost importance.

### 3.3 Output Measurement Considerations

Because the CTIA is an integrator, one could simply measure the amplifier voltage at the end of an integration period to determine the amount of charge that had been accumulated and divide by the integration time to determine the average current. Due to thermal noise, however, when the device is taken out of reset, a random number of charge carriers are present on the input side of the feedback capacitor, producing a random offset voltage, known as the post-reset voltage. The variance

of a single data point ( $\sigma_{sp}^2$ ) at the end of integration would therefore be:

$$\sigma_{sp}^2(t) = \sigma_{PRV}^2 + \sigma_{out}^2(t) \quad (3.40)$$

Because the post-reset voltage offset is constant during one integration, its influence can be eliminated by measuring the difference between the voltage just after reset ( $V_0$ ) and the voltage at the end of integration ( $V_T$ ). This procedure is known as correlated double sampling (CDS), because the two measurements are correlated in time by the single reset. The estimated mean current in charges/s during the integration period  $(N - 1) dt$  for CDS is:

$$\hat{i}_{CDS} = \frac{(V_T - V_0)}{g(N - 1) dt} \quad (3.41)$$

where  $g$  is the amplifier gain in V/(charge). Correlated double sampling removes the effect of the post-reset variance on the measurement but at the cost of doubling the output variance. This is because the output variance is uncorrelated in time even though the sampling is not, so when the two data points are subtracted, their uncorrelated variances add. If, however, the input current is known to be constant during the integration period, the output variance can be reduced through the use of linear least squares (see Chapter 2.3.1).

### 3.4 Signal-to-Noise Ratios and Limits of Detection Equations

The following section will present equations for the limit of detection (LOD) as well as signal-to-noise ratio (SNR) equations for a CTIA operating in a variety of noise

regimes. There are two purposes for presenting these derivations. The first is to establish the optimal estimation procedure for the signal; either correlated double sampling or least squares regression. The second is to establish relationships between the signal-to-noise ratios and thus limits of detection, and amplifier parameters such as read-noise and dark-current noise, gain, and sampling time, to determine which parameters are important for improving signal-to-noise and limits of detection. Garnett and Forrest calculated signal-to-noise expressions for an integrator in both the read-noise limited region and the shot noise limited regime for correlated double sampling, linear regression, and Fowler sampling (69). The conclusion of the authors was that in the read-noise limited case linear regression produces the best signal-to-noise ratio, while in the shot noise limited case correlated double sampling produces the best signal-to-noise ratio. The derivations presented below will show that this is not the case, and that linear regression always produces the best signal-to-noise ratio, except possibly when only a few points are used in the regression.

Because the CTIA acts as a charge-to-voltage converter, the lowest measurable signal can be thought of as a charge. Because there is always an integration time between the reset and the readout of the device, and during that time all incident charge is accumulated on the detector, the limit of detection can also be thought of as the lowest measurable charge divided by the integration time. In addition, because the device can be read without resetting, signal-to-noise, as well as the limit of detection, can be improved through longer integration times. Because current is

charge divided by time, however, so the signal-to-noise as a function of charge as well as the limit of detection in charge will have a different dependency than those for current. Here, limiting signal equations as well as signal-to-noise equations will be presented for both charge and current

The CTIA output noise on the output can be modeled as a voltage noise plus a noise component from the dark current. The total output variance can be expressed as

$$\sigma_{out}^2(t) = \sigma_{rn}^2 + \sigma_{dc}^2 t \quad (3.42)$$

where  $\sigma_{rn}^2$  is the variance from the read-noise and  $\sigma_{dc}^2$  is the variance from the dark current. The noise at the output can be divided into three regions, the first where only a short time has elapsed so the output variance is dominated by  $\sigma_{rn}^2$ , the second where the output variance is influenced by both  $\sigma_{rn}^2$  and  $\sigma_{dc}^2 t$ , and a third where a long time has elapsed so the output variance is dominated by  $\sigma_{dc}^2 t$ . The behavior in the second region will be between the other two. A summary of the SNR and LOD equations derived in the following sections are tabulated in Tables 3.1 and 3.2 respectively, found at the end of this chapter.

### 3.4.1 Correlated Double Sampling (CDS)

#### 3.4.1.a CDS, Read-noise Dominated

The signal in units of charge, estimated by CDS, is

$$v_{q,CDS} = g q_{signal} \quad (3.43)$$

where  $g$  is the gain in volts per charge and  $q$  is the number of charges accumulated during the integration time. Assuming there is no variance associated with sampling time, the standard deviation of the CDS estimation of the charge is

$$\sigma_{q,CDS} = \sigma_{rn}\sqrt{2} \quad (3.44)$$

The units of Equation 3.43 as well as of Equation 3.44, are volts. The signal-to-noise ratio for the signal (in charge) is simply Equation 3.43 divided by Equation 3.44, which gives:

$$SNR_{q,CDS} = \frac{g q_{signal}}{\sigma_{rn}\sqrt{2}} \quad (3.45)$$

where  $q_{signal}$  is the number of charges measured. The limit of detection for charge is dependent only on the read-noise, and this sets the fundamental limit of detection of the device in the read-noise dominated region. This is because the noise in this region is independent of the integration time.

The smallest detectable amount of charge is found by substituting 3 for the SNR in Equation 3.45 and rearranging to get:

$$q_{lod,CDS} = \frac{3\sqrt{2}\sigma_{rn}}{g} \quad (3.46)$$

If the charge arrives at a constant rate during the integration period, the signal in terms of current is Equation 3.43 divided by the integration time  $(N - 1) dt$ , which gives

$$i_{i,cds} = \frac{g q_{signal}}{(N - 1) dt} = g i_{signal} \quad (3.47)$$

The standard deviation of the measured current in the read-noise dominated region is Equation 3.44 divided by the integration time  $(N - 1) dt$ , resulting in:

$$\sigma_{i,CDS} = \sqrt{2} \frac{\sigma_{rn}}{(N - 1) dt} \quad (3.48)$$

The signal-to-noise ratio for the signal in current in this region is then given by

$$SNR_{i,CDS} = \frac{g i_{signal} (N - 1) dt}{\sigma_{rn} \sqrt{2}} \quad (3.49)$$

where  $i_{signal}$  is in charge per second. For a current signal, the signal-to-noise increases linearly with the integration time. This is because, as before, the noise is independent of integration time and remains constant, while the signal increases linearly with integration time.

The lowest detectable current is found in the same manner as Equation 3.46, yielding:

$$i_{lod,CDS} = 3\sqrt{2} \frac{\sigma_{rn}}{g (N - 1) dt} \quad (3.50)$$

The lowest detectable current depends on the integration period, as well as the read-noise. This is understandable because the device acts as a charge-to-voltage converter. There is some minimum detectable charge, but because charge is stored on the feedback capacitor, the longer the integration time required to collect this charge, the lower the current during that integration time must have been, and thus the lower the detectable current.

There is an upper limit to the integration time for the read-noise dominated region. For longer integration times, the contribution of the dark current variance

to the total output variance begins to become significant, and the limit of detection can no longer be described by Equation 3.46 or 3.50. The effect of this dark-current variance will be considered in the next section.

### 3.4.1.b CDS, Dark Current Noise Dominated

When the contribution from the dark current variance to the output variance is great enough, it must be factored in. In the second region, the noise using CDS is given by:

$$\sigma_{q,CDS} = \sqrt{2\sigma_{rn}^2 + \sigma_{dc}^2(N-1)dt} \quad (3.51)$$

where one factor of  $\sigma_{rn}^2$  is from the first point, and the second factor of  $\sigma_{rn}^2$ , as well as the  $\sigma_{dc}^2$  term, come from the second point. The signal is still given by Equation 3.43, so the signal-to-noise ratio is:

$$SNR_q = \frac{g q_{signal}}{\sqrt{2\sigma_{rn}^2 + \sigma_{dc}^2(N-1)dt}} \quad (3.52)$$

For a SNR of three, the smallest charge that can be detected is:

$$q_{lod,CDS} = \frac{3}{g} \sqrt{2\sigma_{rn}^2 + \sigma_{dc}^2(N-1)dt} \quad (3.53)$$

It is interesting to note that the signal-to-noise ratio for charge decreases (the charge limit of detection increases) in this region at longer integration times. This is because the noise in the second sample increases as the integration time increases due to randomness in the accumulation of dark current, but the signal charge does not. For

a charge-detection experiment, after all the charge has accumulated on the detector, there is no benefit to further integration, as the estimation only gets worse.

The signal in terms of current is still given by Equation 3.47 but the noise is now given by Equation 3.51 so the SNR is:

$$SNR_i = \frac{g i_{signal} (N - 1) dt}{\sqrt{2\sigma_{rn}^2 + \sigma_{dc}^2 (N - 1) dt}} \quad (3.54)$$

The lowest detectable current is then:

$$i_{lod,CDS} = \frac{3}{g (N - 1) dt} \sqrt{2\sigma_{rn}^2 + \sigma_{dc}^2 (N - 1) dt} \quad (3.55)$$

For longer integration times, where contribution from the dark current variance to the output variance dominates, these equation simplify to:

$$SNR_{i,CDS} \approx \frac{gi_{signal}\sqrt{dt(N-1)}}{\sigma_{dc}} \quad (3.56)$$

and

$$i_{lod,CDS} \approx \frac{3\sigma_{dc}}{g\sqrt{(N-1)dt}} \quad (3.57)$$

In this case, the limiting current decreases as the inverse square root of the integration time. The noise increases as the square root of integration time, but, if measuring a current, the signal charge increases linearly with integration time, so the estimation of the signal improves. Another way to think about it is: if there is some amount of charge accumulated during the the integration time, the current that this represents is the charge divided by the integration time. Because the noise

only increases as the square root of the integration time whereas the current decreases linearly with integration time, the net effect is that the lowest measurable current decreases as the inverse square root of the integration time.

The gain in volts per charge appears in the previously derived signal-to-noise ratio and limit of detection equations because the current and charge are expressed in charge per second and number of charges respectively, while the read- and dark-current noises are expressed in volts and volts per root second respectively. As discussed in Section 3.1.2, the current gain is different from the voltage gain and the voltage gain is difficult to characterize, so it is more mathematically rigorous to consider the variances on the output, rather than refer them back to the input. In addition, some of the voltage noise on the output is not subject to gain from the amplifier. Noises from currents on the input are subject to the same gain as the input current signal, so the noise from the dark current on the output could be expressed as the noise on the input multiplied by the gain, or:

$$\sigma_{dc} = g\sigma_{dc,input} \quad (3.58)$$

where  $\sigma_{dc}$  is in units of volts per root second as above,  $g$  is in units of volts per charge, and  $\sigma_{dc,input}$  is in units of charge per root second. When Equation 3.58 is substituted into any of the dark current noise limited equations above (Equations 3.56 and 3.57), the gain drops out. This is an important point: increasing the gain does not lead to lower limits of detection in the limit of long integration times. Because the signal and noise are subject to the same gain, that gain has no effect on the signal-to-noise

ratio.

The variance from the shot noise of the signal current has been ignored in these derivations, because the output variance is proportional to the mean of the signal current. For a CTIA detector, the dark current is actually the sum of several input bias currents that mostly cancel out, leaving the net dark current. Although these currents largely cancel, the variance from the shot noise of these currents add, yielding a dark current noise that is larger than the shot noise expected from the magnitude of the dark current. Because of this, the dark current noise will, in general, be much larger than the shot noise from the lowest detectable current.

When the signal current grows large, however, its shot noise begins to dominate, and the output variance can be written as:

$$\sigma_{CDS}^2 = 2\sigma_{rn}^2 + \sigma_{dc}^2 (N - 1) dt + \sigma_{signal}^2 (N - 1) dt \quad (3.59)$$

where  $\sigma_{signal}^2$  is the variance of the signal at the output. Ion arrivals are a Poisson process, so the variance in charge squared per second is equal to the mean in charge per second. This means that the variance on the output due to the signal is  $g^2 i_{signal}$ , so the CDS variance can be rewritten as

$$\sigma_{CDS}^2 = 2\sigma_{rn}^2 + \sigma_{dc}^2 (N - 1) dt + g^2 i_{signal} (1 \text{ charge}) (N - 1) dt \quad (3.60)$$

The signal current in charge per second is  $i_{signal}$ , but for unit consistency the variance from the shot noise from the signal must be charge squared per second, hence the multiplication by (1 charge). In the limit where the shot noise from the signal

dominates all other sources of noise, the signal-to-noise ratio can be written as

$$SNR_{i,CDS} \approx \frac{g i_{signal} (N - 1) dt}{g \sqrt{i_{signal} (1 \text{ charge}) (N - 1) dt}} = \sqrt{\frac{i_{signal} (N - 1) dt}{(1 \text{ charge})}} \quad (3.61)$$

Again, as in Equation 3.55, the noise increases as the square root of the integration time, but the signal increases linearly with the integration time, so the signal-to-noise increases as the square root of the integration time. However, there is less improvement in the signal-to-noise ratio with increasing  $N$  than there is in the read-noise dominated region, shown in Equation 3.49.

### 3.4.2 Least Squares Estimation of the Slope

If charge is arriving at a uniform rate, the current can be measured by determining the slope of the output voltage, instead of just the voltage difference divided by time. Because the signal can be read out without resetting the device, multiple samples of the output voltage can be measured which leads to a reduction in the variance of the slope estimate, and hence an improvement in the signal-to-noise and limits of detection.

#### 3.4.2.a read-noise Dominated

The covariance matrix of the least squares estimator in the read-noise dominated case is given by (56, 61)

$$V(\mathbf{b}) = \sigma_{rn}^2 (\mathbf{X}^T \mathbf{X})^{-1} \quad (3.62)$$

Carrying out this multiplication and evaluating for the variance of the slope parameter gives

$$\sigma_{i,LS}^2 = \frac{12 \sigma_{rn}^2}{dt^2 N(N^2 - 1)} \quad (3.63)$$

The signal-to-noise ratio is then given by

$$SNR_i = \frac{g i_{signal} dt (N - 1)}{\sigma_{rn}} \sqrt{\frac{N(N + 1)}{6(N - 1)}} \quad (3.64)$$

The limit of detection for current in charge per second can be obtained by substituting 3 for the SNR and rearranging to yield

$$i_{lod,LS} = \frac{3\sigma_{rn}\sqrt{2}}{g dt (N - 1)} \sqrt{\frac{6(N - 1)}{N(N + 1)}} \quad (3.65)$$

The current limit of detection is dependent again on the read-noise, but also exhibits a one over  $N\sqrt{N}$  dependency. This is better than the one over  $N$  dependence of the current limit of detection for CDS in the read-noise dominated region as seen in Equation 3.50 by a factor of  $\sqrt{N}$ . The linear regression acts like an average, where each successive point added to the regression provides a new measurement of the signal (the slope) as well as the noise. The noises are uncorrelated, but the signal is correlated, so further measurements improve the overall estimation. If there are only two points used in the regression,  $N = 2$ , then  $N(N + 1)/(6(N - 1)) = 1$  and the standard deviation of the current estimation reduces to Equation 3.48. By collecting more data points within the same integration time, the variance of the slope estimator can be reduced below the variance of CDS.

The signal-to-noise ratio for the signal in charge is obtained by substituting  $i_{signal} = q_{signal}/(N - 1) dt$  into Equation 3.64 yielding:

$$SNR_q = \frac{g q_{signal}}{\sigma_{rn}\sqrt{2}} \sqrt{\frac{N(N+1)}{6(N-1)}} \quad (3.66)$$

The limit of detection in charge is obtained in the same manner as Equation 3.65, resulting in:

$$q_{lod,LS} = \frac{3\sigma_{rn}\sqrt{2}}{g} \sqrt{\frac{6(N-1)}{(N(N+1)}}} \quad (3.67)$$

As before, the SNR and the limit of detection for charge are a factor of  $1/N$  worse than for current. In addition, like for current, if only two points are used for the regression, Equation 3.67 converges to Equation 3.46.

### 3.4.2.b Dark Current Noise Dominated

In the dark current noise dominated region, the variance of the slope estimator is no longer described by Equation 3.62. Because the variance is time dependent, generalized least squares must be used (56, 61). Instead of assuming the errors  $\epsilon$  are independently distributed, it is assumed they are drawn from a normal distribution with zero mean and variance  $\Sigma$ , which is an order- $N$  matrix that is symmetric and positive definite. The diagonal entries of  $\Sigma$  represent the variances at time  $i dt$  where  $i = 1 \dots N$  and the off-diagonal entries correspond to correlated errors (56, 61). Using this error matrix, the estimation  $\mathbf{b}$  of the parameter vector  $\beta$  is

$$\mathbf{b}_{GLS} = (\mathbf{X}^T \boldsymbol{\Sigma}^{-1} \mathbf{X})^{-1} \mathbf{X}^T \boldsymbol{\Sigma}^{-1} \mathbf{y} \quad (3.68)$$

and the variance is

$$V(\mathbf{b}_{\text{GLS}}) = (\mathbf{X}^T \boldsymbol{\Sigma}^{-1} \mathbf{X})^{-1} \quad (3.69)$$

In general, the output variance as a function of time is

$$\sigma_{out}^2(t) = \sigma_{rn}^2 + \sigma_{dc}^2 i dt \quad (3.70)$$

where  $i = 0 \dots N-1$ . However, it is mathematically difficult to construct the matrix  $\boldsymbol{\Sigma}$  for this variance, due to the presence of the  $\sigma_{rn}^2$  term. Therefore, it is easiest to consider only times where  $\sigma_{dc}^2 i dt$  is much larger than  $\sigma_{rn}^2$ . This assumption is valid for larger  $dt$  as well as when the signal current is large, so the shot noise from the signal current dominates. Because the shot noise from the signal has the same time dependence as the noise from the dark current, in the signal shot noise dominated region, the expression for the signal shot noise can be substituted for  $\sigma_{dc}$ .

Ignoring the read-noise still leaves a problem, because this makes the variance at  $i = 0$  zero. This would make the first diagonal element of  $\boldsymbol{\Sigma}$  zero, which would make it a non-invertible matrix (70). This problem is circumvented by choosing to leave the point  $i = 0$  out of the regression, and instead using only the points  $i = 1 \dots N - 1$ , which means the regression is carried out over only  $N - 1$  points instead of  $N$  points. With these assumptions and assuming there are no correlated

errors, the matrix  $\Sigma$  is given as:

$$\Sigma = \begin{bmatrix} \sigma_{dc}^2 1 dt & 0 & \cdots & 0 \\ 0 & \sigma_{dc}^2 2 dt & \cdots & 0 \\ \vdots & \vdots & \ddots & \vdots \\ 0 & 0 & \cdots & \sigma_{dc}^2 (N-1) dt \end{bmatrix} \quad (3.71)$$

The variance of the slope estimator is the second diagonal element of Equation 3.69, which evaluates to (see Appendix A.3 for the derivation):

$$V(b_1) = \frac{2\sigma_{dc}^2}{dt} \frac{H_{N-1}}{(N-1)[(H_{N-1}-2)N+2]} \quad (3.72)$$

where  $H_{N-1}$  is the  $(N-1)$ th harmonic number, given by:

$$H_{N-1} = \sum_{i=1}^{N-1} \frac{1}{i} \quad (3.73)$$

The signal-to-noise ratio is Equation 3.47 divided by the square root of Equation 3.72 which gives:

$$SNR_{i,GLS} = \frac{g i_{signal} \sqrt{dt}}{\sigma_{dc} \sqrt{2}} \sqrt{\frac{N[(H_N-2)N+H_N]}{H_N}} \quad (3.74)$$

$$\approx \frac{g i_{signal} \sqrt{dt}}{\sigma_{dc} \sqrt{2}} N \quad (3.75)$$

The current limit of detection is then:

$$i_{lod,GLS} = \frac{3\sigma_{dc}\sqrt{2}}{g\sqrt{dt}} \sqrt{\frac{H_N}{N[(H_N-2)N+H_N]}} \quad (3.76)$$

$$\approx \frac{3\sigma_{dc}\sqrt{2}}{g\sqrt{dt}} \frac{1}{N} \quad (3.77)$$

The harmonic numbers increase with increasing  $N$ , so as  $N$  increases, the square root factor converges to  $N$ , meaning as the integration time increases, the SNR

increases linearly with the number of samples. This is better than the signal-to-noise for CDS in this region (Equation 3.54) by a factor of  $\sqrt{N}$ .

Following the same procedures as above, the charge signal-to-noise ratio and limit of detection are:

$$SNR_{q,GLS} = \frac{g i_{signal}}{\sigma_{dc} \sqrt{2 dt}} \sqrt{\frac{[(H_N - 2)N + H_N]}{N H_N}} \quad (3.78)$$

$$\approx \frac{g i_{signal}}{\sigma_{dc} \sqrt{2 dt}} \quad (3.79)$$

and

$$q_{lod,GLS} = \frac{3\sigma_{dc} \sqrt{2 dt}}{g} \sqrt{\frac{N H_N}{[(H_N - 2)N + H_N]}} \quad (3.80)$$

$$\approx \frac{3\sigma_{dc} \sqrt{2 dt}}{g} \quad (3.81)$$

The signal-to-noise as well as the limit of detection converge to a constant in the limit of high  $N$ .

### 3.4.3 Influence of the Sampling Rate on SNR and LOD

For correlated double sampling, since only two data points are measured, the sampling rate does not matter. However, for linear least squares estimation it will make a difference. The SNR and LOD equations presented above assume a fixed sampling rate of  $1/dt$ . However, to examine the influence of the sampling rate it is necessary to assume a fixed integration time. The integration time  $T_{int}$ , number of samples  $N$ , and the sampling time  $dt$  are related by:

$$N \approx \frac{T_{int}}{dt} \quad (3.82)$$

assuming the integration is an integer number of sampling periods and  $N$  is large enough so  $(N-1) \approx N$ . For a fixed sampling time, Equation 3.82 can be substituted for  $N$  into all the previously derived SNR and LOD equations to show the effect of sampling time. All the SNR equations for CDS exhibit no dependence on the sampling time, while the equations for least squares all exhibit a  $1/\sqrt{dt}$  dependence. Therefore, a shorter sampling time, obtained by having a faster sampling rate, will lead to increased signal-to-noise, as well as decreased limits of detection.

### 3.5 Conclusions

The derivations above indicate that, in contrast to the conclusion of Garnett and Forrest, the SNR for linear regression is better by a factor of  $\sqrt{N}$  than that for correlated double sampling, both in the read-noise dominated regime as well as the dark current noise dominated regime. Therefore, if the input signal to a CTIA is a constant current, it is always beneficial to perform multiple non-destructive read-outs and estimate the current using least squares. An implication of this is that the quality of the slope estimation, and thus the signal-to-noise ratio increases with the number of points used in the estimation. The signal-to-noise ratio improves more with increasing  $N$  in the read-noise dominated regime than it does in the dark current or shot noise dominated regime, because while read-noise is uncorrelated in time, because the CTIA is an integrator the dark current and shot noise are correlated in time. Because dark current and shot noise variance increase linearly

with time, it is desirable to collect as many samples as possible while still remaining in the read-noise dominated region. Therefore, and as shown above, it is beneficial to make the sampling rate as fast as possible to improve signal-to-noise ratios and detection limits.

While it is ideal to operate in the read-noise limited regime, the fundamental limits of detection are achieved through long integrations, which means operating in the dark current limited regime. As the CTIA is a charge-to-voltage converter, the ultimate limits of detection are in charge. For both linear regression as well as correlated double sampling, these limits are dependent on the dark current noise and not the read-noise. In addition, because the dark current noise experiences the same gain as the input signal, there is no dependence on the gain. However, because the voltage gain is related to but not identical with the current gain, and because there are components of the output voltage noise that do not arise from the input, it is still important to make the gain as high as possible. Finally, although the read-noise does not influence the fundamental limits of detection, it does linearly effect the limits of detection in the read-noise limited case. It is therefore still beneficial to reduce it as well. Because the relationship between the read-noise and the dark current noise influences what noise regime an experiment is in, it is important to try to reduce both the read and the dark current noise so as to allow large numbers of samples to be measured while still remaining in the read-noise limited domain. In general then, increases in the CTIA gain, as well as decreases in the read and dark

current noise as well as the sampling time will lead to decreases limits of detection and therefore improved sensitivity.

Table 3.1: Summary of signal-to-noise equations

Signal-to-Noise Ratio		
CDS	Current	Charge
Read-Noise	$\frac{g i_{signal} dt (N-1)}{\sigma_{rn} \sqrt{2}}$	$\frac{g q_{signal}}{\sigma_{rn} \sqrt{2}}$
Dark-Current Noise	$\approx \frac{g i_{signal} \sqrt{dt (N-1)}}{\sigma_{dc}}$	$\approx \frac{g q_{signal}}{\sigma_{dc} \sqrt{dt (N-1)}}$
Least Squares	Current	Charge
Read-Noise	$\frac{g i_{signal} dt (N-1)}{\sigma_{rn} \sqrt{2}} \sqrt{\frac{N(N+1)}{6(N-1)}}$	$\frac{g q_{signal}}{\sigma_{rn} \sqrt{2}} \sqrt{\frac{N(N+1)}{6(N-1)}}$
Dark-Current Noise	$\approx \frac{g i_{signal} \sqrt{dt}}{\sigma_{dc} \sqrt{2}} N$	$\approx \frac{g q_{signal}}{\sigma_{dc} \sqrt{2 dt}}$

Table 3.2: Summary of LOD equations

Limit of Detection		
CDS	Current	Charge
Read-Noise	$\frac{3\sigma_{rn} \sqrt{2}}{g dt (N-1)}$	$\frac{3\sigma_{rn} \sqrt{2}}{g}$
Dark-Current Noise	$\approx \frac{3\sigma_{dc}}{g \sqrt{dt (N-1)}}$	$\approx \frac{3\sigma_{dc} \sqrt{dt (N-1)}}{g}$
Least Squares	Current	Charge
Read-Noise	$\frac{3\sigma_{rn} \sqrt{2}}{g dt (N-1)} \sqrt{\frac{6(N-1)}{N(N+1)}}$	$\frac{3\sigma_{rn} \sqrt{2}}{g} \sqrt{\frac{6(N-1)}{N(N+1)}}$
Dark-Current Noise	$\approx \frac{3\sigma_{dc} \sqrt{2}}{g \sqrt{dt}} \frac{1}{N}$	$\approx \frac{3\sigma_{dc} \sqrt{2 dt}}{g}$

## CHAPTER 4

### DM0025 1696 PIXEL MONOLITHIC CTIA ARRAY DETECTOR

The 1696 pixel CTIA array detector is the latest generation of array detectors used in the Denton research laboratory. This device was manufactured by ImagerLabs as a result of a long collaboration with the Denton laboratory. This chapter describes the 1696 CTIA array detector, as well the operating procedures used in the remainder of this dissertation. In addition, several observed deviations from ideal behavior are described.

#### 4.1 DM0025

The ImagerLabs DM0025 is a 1696 pixel capacitive transimpedance amplifier array manufactured on a single piece of silicon. The device consists of two interdigitated arrays of 6mm long electrodes, spaced 12.5  $\mu\text{m}$  apart. Each electrode is 10.5  $\mu\text{m}$  wide with 2  $\mu\text{m}$  of insulation on each side, giving an active area, also called a fill factor, of 84%. The device is fabricated using a 3.3V, 0.35  $\mu\text{m}$  minimum dimension process.

Each of the two arrays consists of 848 electrodes, or pixels, and a set of control lines, power lines, and outputs. Each electrode is connected to its own pre-amplifier with a capacitive feedback element. The block diagram of the device is shown in

Figure 4.1. Each pre-amplifier has two feedback capacitors, one nominally  $10fF$  and the other nominally  $10pF$ . Each feedback loop also includes two switches; one to switch in and out the large capacitor, and the other to short the input to the output, resetting the device. These switches consist of several field effect transistors (FETs) in a complex arrangement to reduce  $KT/C$  noise (Chapter 2.4.1.a) and feedback leakage. Each amplifier has another FET switch on its output that connects to a sample-and-hold circuit created from another  $10fF$  capacitor and a unity gain amplifier. The output of each sample-and-hold stage is connected by a shift-register multiplexer (MUX) through yet another FET switch to a unity gain output buffer amplifier, which yields the final output signal. Each pre-amplifier also has a  $10fF$  capacitor connecting its input to a parallel input line called the PAin. Voltage signals can be applied to the PAin input of the DM0025 to assist in characterization.

Each pixel in an array can be read independently by connecting the gate of the pixel READ FET to the output of a logical AND gate between the ChREAD control line and an address line for the pixel. In order to read a specific pixel, pixel 0 for example, the ChREAD line must be held high, as well as the address line for pixel 0. If both lines are HIGH, the output of the logical AND gate is also HIGH, so the read FET is closed and the output of the sample-and-hold stage for pixel 0 is connected to the output buffer. All other address lines are held LOW, so the outputs of all the other pixels' logical AND gates are LOW, keeping the READ FETs for all other pixels open. This ensures the output from only one pixel's sample-and-hold stage is

connected to the output buffer at a time, preventing conflicts.

An individual pixel in the array is addressed using a shift register. A shift register consists of a series of D flip-flops sharing a common clock, and connected together in a specific way. A D flip-flop is a circuit that has two stable states, e.g. HIGH and LOW, that is used to store state information. It has two inputs and two outputs, as depicted in Figure 4.2. The input  $D$  is the control input and the triangle is the clock input. The two outputs are  $Q$  and  $Q'$ , where  $Q'$  is the negation of  $Q$ . When the clock voltage change is positive, the  $Q$  output takes on the value of the  $D$  input. While the clock voltage change is not positive (the voltage is either decreasing or remaining the same), the  $Q$  output remains unchanged. The D flip-flop thus acts like a data storage element.

In the shift register, the output  $Q$  of each flip-flop, except the last, is connected to the input  $D$  of the next flip-flop in the series, so that when the clock line goes positive, the state of each flip-flop is copied to the next flip-flop. For example, if the initial state of each flip-flop is LOW, and the input  $D$  is held at HIGH, when the clock swings positive, the output  $Q$  of the first flip-flop becomes HIGH. All the other output  $Q$ s remain at LOW. If the input  $D$  is then set to LOW, the next time the clock swings positive, the output  $Q$  of the second flip-flop is set to HIGH, while the output  $Q$  of the first flip-flop is set to LOW. The output  $Q$  of the third, and remaining flip-flops remain at LOW. If the input  $D$  remains at LOW, each positive swing of the clock moves the HIGH from the output  $Q$  of its current flip-flop to

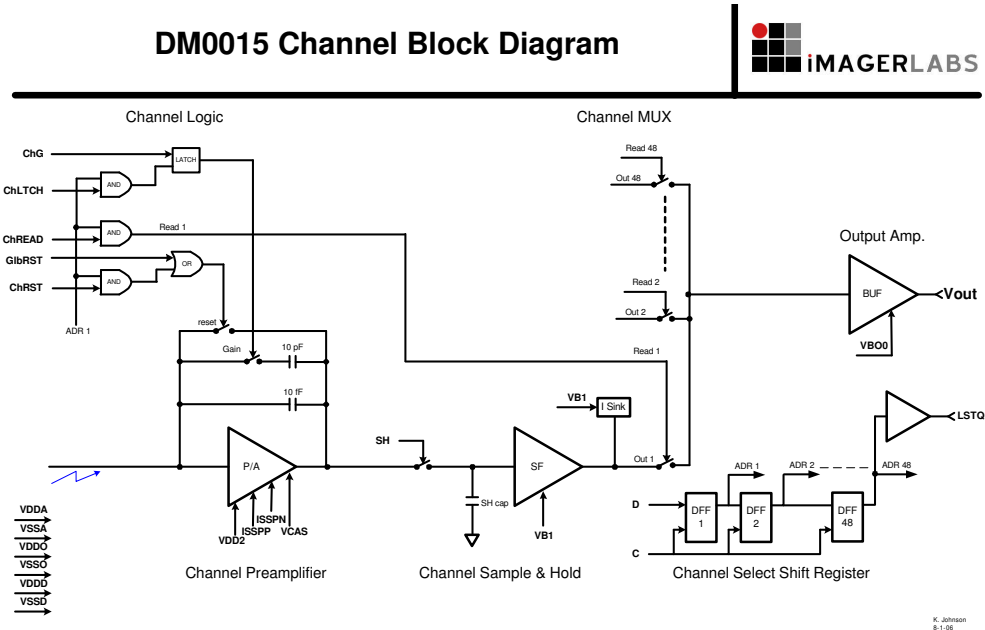


Figure 4.1: Block diagram of the DM0025 1696 pixel CTIA array detector.

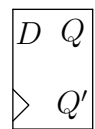


Figure 4.2: Diagram of a D flip-flop.

the next flip-flop in line. In the DM0025 device, the output  $Q$  of each flip-flop in the shift register acts as the address line for a single pixel. The device has two 848 element shift registers, one for each array of pixels.

There are two reset modes: individual reset and global reset. For each pixel, the individual reset line, ChRST, is logically ANDed with the pixel's address line, and the output is logically ORed with the global reset line, GlbRST. The output of this logical OR is connected to the gate of the pixel reset FET. In this way, each pixel can be reset, individually, or they can all be reset simultaneously. Because the shift register is typically operated so it addresses only one pixel at a time, individual resets do not happen at the same time, thus necessitating the global reset line in order to simultaneously initiate detection by all pixels.

The gain control for each pixel works in a similar fashion. The gate of the gain FET switch is connected to a LATCH flip-flop. This LATCH flip-flop will store the value on its input when its control line is held high. The control line for the LATCH flip-flop is connected to the output of a logical AND gate placed between the pixel address line and the ChLTCH control line. To set the gain for a specific pixel, the ChLTCH line is held high and the shift-register is advanced  $n$  time so the address line of the  $n$ th desired pixel is HIGH. This sets the output of the LATCH flip-flop for the selected pixel to the value of the ChG gain line, LOW for high gain and HIGH for low gain. A HIGH value on the output of the LATCH flip-flop closes the gain FET to switch the  $10pF$  capacitor into the feedback network, thus putting the

device in low gain. The output of the LATCH flip-flop stays where it is set until the control line is held HIGH again, allowing the gain to be set individually for each pixel. This is an important feature for an array detector, because it allows the gain to be independently set to low for high intensity peaks of a spectrum and to high for low intensity peaks, thus increasing dynamic range.

The gate of the sample-and-hold switch for each pixel is connected to a single control line, called the SH control line. Because each pixel has to be individually addressed using the shift register, they cannot be read out simultaneously. The purpose of the sample-and-hold stage is to sample the voltage of all pixels simultaneously so although each pixel is read sequentially, the output voltages represent simultaneous acquisitions in time.

## 4.2 Daughter Board and Motherboard

The DM0025 is not a stand-alone device; it needs support electronics to run properly. The support electronics are spread across two circuit boards: a daughter board and a motherboard. The daughter board consisted of a series of pads to which the pads of the DM0025 are wire bonded. It also included bypass capacitors for all the power lines going to the device, and a pair of voltage follower amplifiers with a gain of 2, acting as buffers for the two device outputs. These buffers are necessary because the output buffers in the DM0025 cannot supply enough current to drive most loads. This daughter board was connected to a main motherboard with a series of wires.

The motherboard was custom designed in the Denton group by Wit Wisniewski. The motherboard had a series of regulators to provide the various power lines to the device, as well as a series of buffers for the control signals. The motherboard was controlled by a National Instruments PCI-6281 18 bit Multifunction card. Because there were not enough control lines available from the multifunction card, some of the device control lines were connected together. Most importantly, the output  $Q$  from the left shift register was connected to the input  $D$  of the right shift register. The control lines for each array were tied together as well. This means that the pixels on each side of the detector were addressed sequentially; first the odd numbered pixels and then the even numbered pixels.

#### 4.3 Basic Operating Procedure

The device is powered, then the program to control the device is started. This program applies 2.9 V to VDD2 and 3.275 V to ISSPN and sets the global reset line high. The program generates a series of 8 bit commands for each acquisition loop and sends them to device to acquire data. The signal for each bit of the command is shown in Table 4.1.

The analog to digital converter (ADC) on the National Instruments PCI-6281 card used to control the device can run at up to 250 kSamples/s (kS/s) for two channels. In practice, the card is usually run at 247 kS/s. The card is used to generate the clock signal for the DM0025, so because it takes two card cycles to

generate one cycle of clock signal (one card cycle for clock HIGH and one card cycle for clock LOW), the CTIA device is run at half the card frequency, typically 123.50 kS/s.

#### 4.3.1 Acquisition of All Pixels

Each acquisition loop consists of the following series of commands. The gain line is held at the appropriate level for the chosen gain through out the whole command series, and unless otherwise stated the global reset line is held LOW. First, to ensure the shift register elements are all LOW, the input D line to the shift register is held LOW while the clock is cycled from LOW to HIGH back to LOW (one clock cycle) 1696 times. This ensures that the LOW on the shift register input D line has been copied to all the shift register elements. Then, the shift register input D line is held HIGH for one clock cycle (one LOW to HIGH to LOW) and held LOW for 1695 clock cycles while the gain LATCH is held HIGH and the gain line is held at either LOW or HIGH to set the gain to the desired level. A LOW on the gain line sets

bit	signal
0	clock
1	shift register Q
2	Sample & Hold
3	ChlRead
4	Chl Gain
5	Chl Latch
6	Global Reset
7	Chl Reset

Table 4.1: Structure of an 8 bit command

the gain to high and a HIGH on the gain line sets the gain to low, switching the 10 pF capacitor into the feedback loop. This sequence of holding the shift register input D line HIGH for one clock cycle and then LOW for 1695 clock cycles is known as "clocking a pulse" through the shift register. Optionally, the global reset line is raised to HIGH for a single clock cycle to provide a trigger pulse for external signals. Next, each pixel is individually reset by clocking a pulse through the shift register while the channel reset line is held HIGH. This channel reset cycle is performed twice to undo the effects of the device being held in global reset. If the device is in sample-and-hold mode, the sample-and-hold switch is closed at the beginning of each read cycle, then opened for the rest of the read cycle, so the read voltages for all pixels are from the same time. If the device is not in sample-and-hold mode the sample-and-hold switch is left closed throughout the entire read cycle.

#### 4.3.2 Single-Pixel Operation

A second procedure is used to characterize the device one pixel at a time. The command array is the same as the first program until after the two reset cycles. In the single pixel program, a pulse is clocked through the shift register to the selected pixel, then left there so the selected pixel is addressed for the rest of the acquisition loop. The device is read for 32384 clock cycles to move out of the warm-up phase described in the previous section. The Chl Reset line is held HIGH for 1696 clock cycles, then read again for the desired number of clock cycles. Note that during

these different phases the shift register is not actually clocked, so the pulse stays at its location in the register and continues to address the same pixel.

#### 4.4 Reset Behavior

Knowledge of the reset behavior of the DM0025 CTIA device was important because each integration period starts and ends with a reset. The average voltages measured for each pixel when the global reset line was held HIGH and the sample-and-hold switch closed are shown for high gain in Figure 4.3 and low gain in Figure 4.4. These data were collected using the basic operating procedure described above, but with the global reset line held high during the read phase. As expected, the behavior was the same for both high and low gain, but the reset voltages were not constant across all of the pixels. This behavior is surprising, because each pixel's amplifier was supposed to be biased to the same potential, so they should all have had the same reset voltage. It is possible that this spread in reset voltages is due to inconsistencies in manufacturing. This hypothesis could be tested by comparing the reset voltages of two separate DM0025s. If each device had a different reset voltage distribution, it would indicate that the reset voltage distribution was from manufacturing. If each device had the same reset voltage distribution it indicate this behavior was design related. Data collected using the single-pixel program have the same shape, indicating that this distribution of global reset voltages was not due to sampling each pixel sequentially.

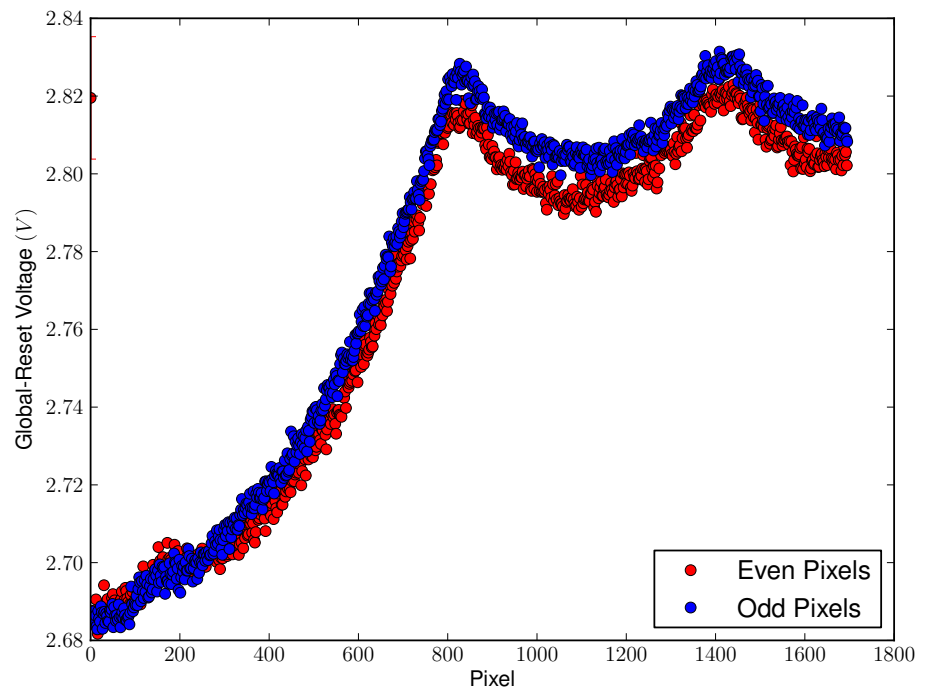


Figure 4.3: Voltage with the global reset line high, the sample-and-hold switch closed, and the device in high gain. Error bars were calculated at 99% confidence, but are not visible on the plot.

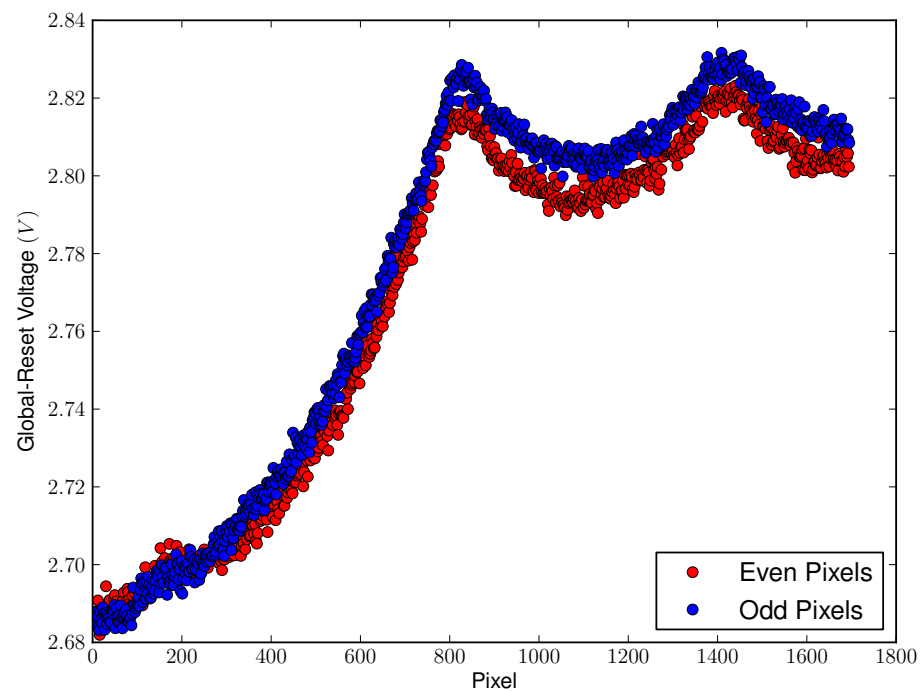


Figure 4.4: Voltage with the global reset line high, the sample-and-hold switch closed, and the device in low gain. Error bars were calculated at 99% confidence, but are not visible on the plot.

For this device, using global reset presents some problems. If the device is in high gain and global reset line is held high while the sample-and-hold switch is open, the output for each pixel oscillates between the power rails, as seen in Figure 4.5. Figure 4.6 shows the device behavior coming out of global reset in high gain. As can be seen, the post global reset voltages have a large spread, covering most of the dynamic range. The spread in initial voltages shown in Figure 4.6 was much larger than the spread shown in Figure 4.3. Because the global reset line was held HIGH while the device was idle, it became standard operating procedure to perform two cycles of individual channel resets to undo the effects of these behavior and return the starting voltages to their normal high gain spread. Neither the voltage oscillating between the power rails, nor the large spread in post global reset voltages was observed in low gain.

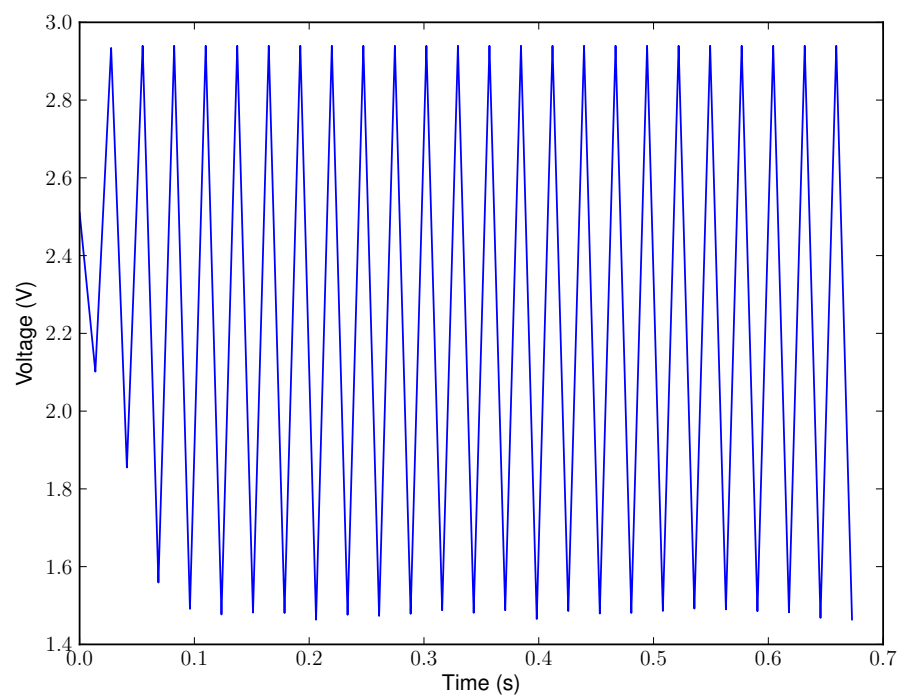


Figure 4.5: Global reset voltage with the sample-and-hold switch open in high gain for pixel 500. Because of this oscillation, global reset could not be used in conjunction with sample-and-hold operation while the device was in high gain.

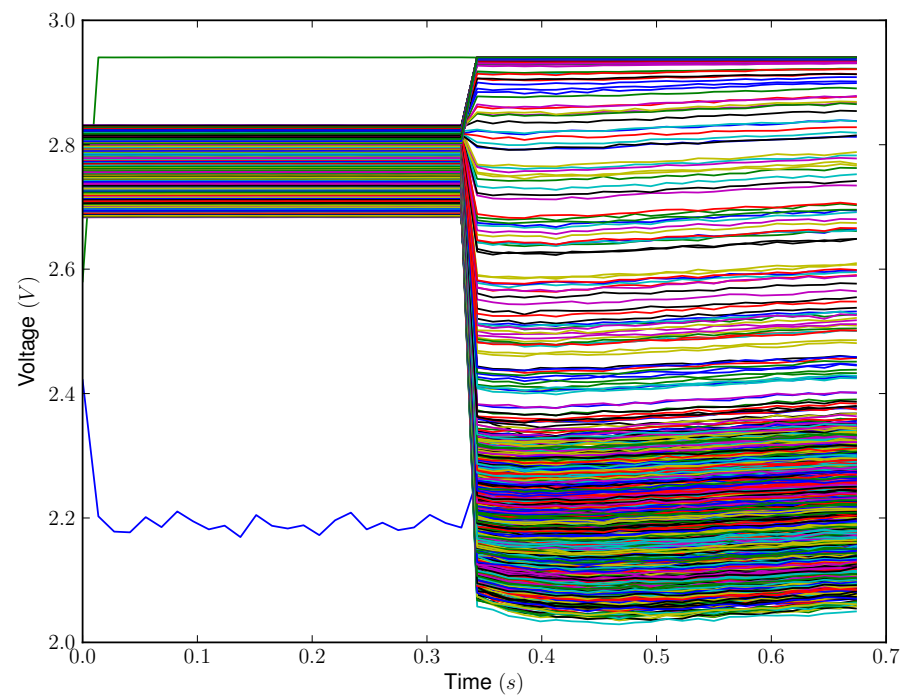


Figure 4.6: Voltage before and after lowering of the global reset line in high gain. The spread of post-global-reset voltages was much wider than the spread of post-reset voltages.

## CHAPTER 5

### CHARACTERIZATION OF THE 1696 PIXEL ARRAY DETECTOR

This chapter presents the results from a detailed characterization of the 1696 pixel CTIA array detector, also referred to as the DM0025. It is important to conduct a detailed characterization of any new detector for a number of reasons. First, a detailed characterization can be compared to the models derived in Chapter 3 in order to determine over what range of operating parameters the model matched the actual device behavior. Second, a detailed detector characterization is important for comparison of the performance of this detector to other generations of CTIA detectors, as well as to other types of detectors in general. This comparison gives insight about how future detectors should be designed to improve detector performance. Third, ion detectors are typically used in conjunction with some instrument, such as the mass spectrometer described in this dissertation. A detailed characterization of the detector separate from the instrument is important to better evaluate the performance of the combined instrument and detector. A comparison between the detector performance separate from the instrument with the detector performance when combined with the instrument gives insight about what changes need to be made to either the detector or the instrument in future generations to improve overall system performance.

To measure various parameters of the DM0025, support electronics, including an analog to digital converter (ADC) and a commercially available CTIA amplifier, the TI/Burr-Brown ACF2010, were used. These support electronics had to be characterized before they could be used to characterize the DM0025, to ensure they would provide accurate information about the CTIA. The results of the characterization of the ADC and the ACF2101 are presented in Appendix B. The ACF2101 was used in conjunction with an ion gun to characterize the 1696 pixel CTIA array gain. As discussed below, this procedure was used instead of mean-variance analysis because of deficiencies in the ion gun. Next, the behavior of the dark current and post-reset behavior, as well as the output noise are examined as a function of temperature to determine the optimal temperature regime in which to operate the device. The noise in low gain is essentially independent of temperature, while the noise in high gain decreases with temperature. A detailed characterization of the read and dark current noise at this limiting temperature is then presented. Finally, the results from this characterization are used in conjunction with the linear model, signal-to-noise ratio equations, and limit of detection equations derived in Chapter 3 to predict the performance of the DM0025. These predictions were tested in Chapter 6 using a linear cycloid mass spectrometer and the deviations from the predicted values are examined herein.

The outputs of the DM0025 CTIA array detector are connected to a pair of buffer amplifiers on the daughter board, each with a gain of  $2.00 \pm 0.01$ . The voltages on

the output of these buffer amplifiers, as a function of time, are typically the data that are collected, using an analog to digital converter. The parameters of interest, however, are either voltages or noises measured at the DM0025 outputs, which were connected to the input of these buffer amplifiers. Because the buffer amplifiers were simple non-inverting voltage followers, the voltage on the input of these amplifiers could be determined by dividing the measured buffer amplifier output voltage by the buffer amplifier gain. In this chapter, unless otherwise specified, all voltages have been converted to voltages at the output of the DM0025 (the input of the buffer amplifiers) in this manner. In addition, whenever a voltage or noise is labeled as "output referred", it indicates that that voltage or noise was converted to a voltage or noise on the output of the DM0025 CTIA array detector chip itself. Whenever a voltage or noise is labeled as "input referred", it indicates that that voltage or noise was converted to a voltage or noise on the input of the DM0025 CTIA array detector chip by dividing the voltage or noise on the output of the DM0025 by the current gain of the DM0025. Referring all voltages and noise to either the input or the output of the DM0025 allows these parameters to be compared to other amplifiers without the influence of the buffer amplifiers.

### 5.1 Flat Fielding of the 1696 Pixel CTIA Array Detector

Before characterizing the gain of the CTIA array detector, the uniformity of the pixel gain had to be determined. As discussed in Chapter 2.4.4, the variability in

the gain of the individual elements of the array constitutes fixed pattern noise. To remove the effect of this noise, the array must be "flat fielded" by measuring the gain for each pixel. Ideally, as discussed in Chapter 3.2, the device would be flat fielded using an ion gun and mean-variance analysis, but the only ion gun available for performing these experiments suffered from instabilities that, as discussed in Chapter 3.2.2, made mean-variance analysis impossible. For this reason, the device had to be flat fielded in a two step process: first by measuring the variability of the gain across the array, and second by measuring the absolute gain for a small set of pixels. The combination of these two measurements allowed the gain across the array to be characterized.

### 5.1.1 Gain Uniformity of the 1696 Pixel CTIA Array Detector

#### 5.1.1.a Experimental Procedure

An Agilent 33220A 20 MHz function generator was used to characterize the uniformity of the DM0025 pixels. The output of the function generator was connected to the PAin input of the device and a sawtooth waveform applied. Each pre-amplifier also has a  $10fF$  capacitor connecting its input to a parallel input line called the PAin (See Chapter 4.1). Because the combination of the PAin input capacitor and the feedback capacitor formed a voltage divider, this sawtooth wave was reproduced on the output, scaled by the voltage gain of the amplifiers. The duty cycle of the sawtooth wave was set so the wave consisted of a downward sloping ramp followed by

a sharp rise. The acquisition was timed so the DM0025 was in reset during the sharp rise portion of the sawtooth, so the measured output was just a downward sloping ramp. The output waveform was measured for 40 acquisitions without resetting the integrator (non-destructively), and the experiment was repeated 10 times.

### 5.1.1.b Results

A plot of the slope of the output as a function of pixel can be seen in Figure 5.1. There was some pixel-to-pixel variation in the response to the input signal. Because the input signal was the same for each pixel, this variation can be attributed to variance in the pixels' feedback capacitors. The relative standard deviation of the slopes is 3.0 % RSD. This standard deviation is due to variance in both the feedback capacitors and the PAin input capacitors. For high gain, the PAin capacitors and the feedback capacitors are the same size, so, if it is assumed that all the capacitors come from the same distribution, then the relative standard deviation of the distribution of feedback capacitors alone should be  $\sqrt{2}$  smaller, or 2.1 % RSD. The feedback capacitors are about 1000 times larger in low gain than in high gain but the PAin input capacitors are the same, so the voltage divider produced by the pair has a gain of about 1/1000. To characterize low gain in the same manner would, thus, require a sawtooth wave of over 1000 volts. Unfortunately, the device can only tolerate a maximum voltage of 3.3V on the input, so there is no feasible way to characterize the uniformity of the low gain feedback capacitors using the PAin input. A highly

uniform ion beam is needed to fully characterize the low gain pixel uniformity.

### 5.1.2 Gain of a Subset of Pixels of the 1696 CTIA Array Detector

#### 5.1.2.a Experimental Procedure

The detector was mounted in the ion gun vacuum chamber and cooled to approximately 240K. Because of the manner in which the detector assembly was mounted in the vacuum chamber, this was the minimum temperature achievable with the cooling setup. The ion gun was masked with a long brass tube with a 400  $\mu\text{m}$  slit, aligned vertically, i.e., with the long axis of the opening perpendicular to the array axis. A Faraday cup assembly, designed and build by Dr. Jan Lorincik, was mounted on a horizontal translation arm that extended between the slit and the surface of the CTIA detector. The entrance to the Faraday cup was a 1 mm diameter hole in a plate. An identical hole appeared 14.5 mm farther down the surface of the plate. The surface of the plate acted as a mask, so the ion flux that passed through the first hole into the Faraday cup was the same as the ion flux that passed through the second hole. The Faraday cup was attached, through a vacuum feed-through, to the input of the ACF2101 switched integrator, described in Appendix B.2.

Low gain of the CTIA detector was characterized by setting the ion gun to a series of beam currents and allowing it to stabilize between changes in current. The beam current was measured 60 times with each detector, first with the CTIA detector through the second hole in the Faraday assembly, and then with the Faraday cup

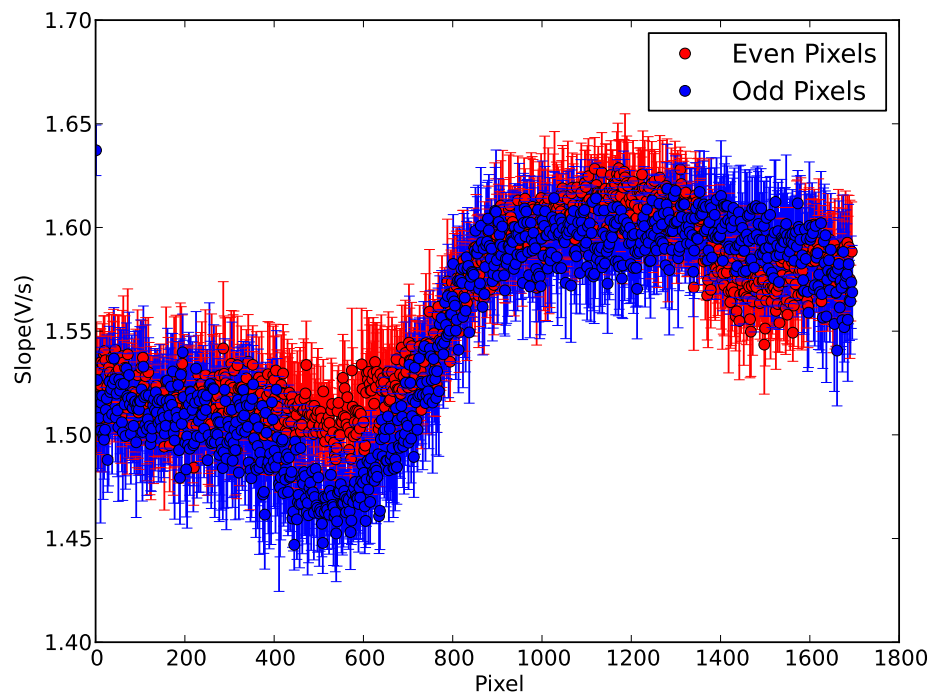


Figure 5.1: Uniformity of the DM0025 pixel gain, measured by application of a saw-tooth waveform to the PAin input capacitor in high gain. Error bars represent 99% confidence intervals for the average of 10 values. The estimated relative standard deviation of the gains was 2.1 %

and ACF2101 switched integrator. Backgrounds were collected for both detectors by moving the Faraday cup assembly so the ion beam was not directed at either hole. The gain calibration plot in Figure 5.2 is a comparison between the summation of the response of the CTIA detector across the pixels illuminated by the ion beam (pixels 930 through 1088) and the total current measured by the ACF2101. From the plot, low gain is about  $-6.3 \pm 0.3 \times 10^{10} \frac{V}{A \cdot s}$ , which corresponds to about  $-10 \frac{nV}{charge}$ . The influence of the output buffer amplifiers on the daughter board was taken into account, so this gain represents the gain of the DM0025 by itself. It was assumed that the gain was constant across the portion of the array illuminated by the ion beam. The data presented Figure 5.1 show that, within error, this assumption was valid. Using the pixel uniformity data in Figure 5.1 and the gain measured above, the CTIA can be flat-fielded if desired. The gain was not measured for any other region of pixels because there was not another sufficiently uniform region of pixels to use this gain calibration procedure.

### 5.1.2.b Results

Unfortunately, the instability of the ion gun dominated the measurements of the amplifier gains. The ion gun power supply did not regulate filament current well, and though it would come to a somewhat constant emission current within a few minutes, within a few dozen more minutes the gun would begin to overheat and lose current regulation. In addition, because the gun would also lose current regulation

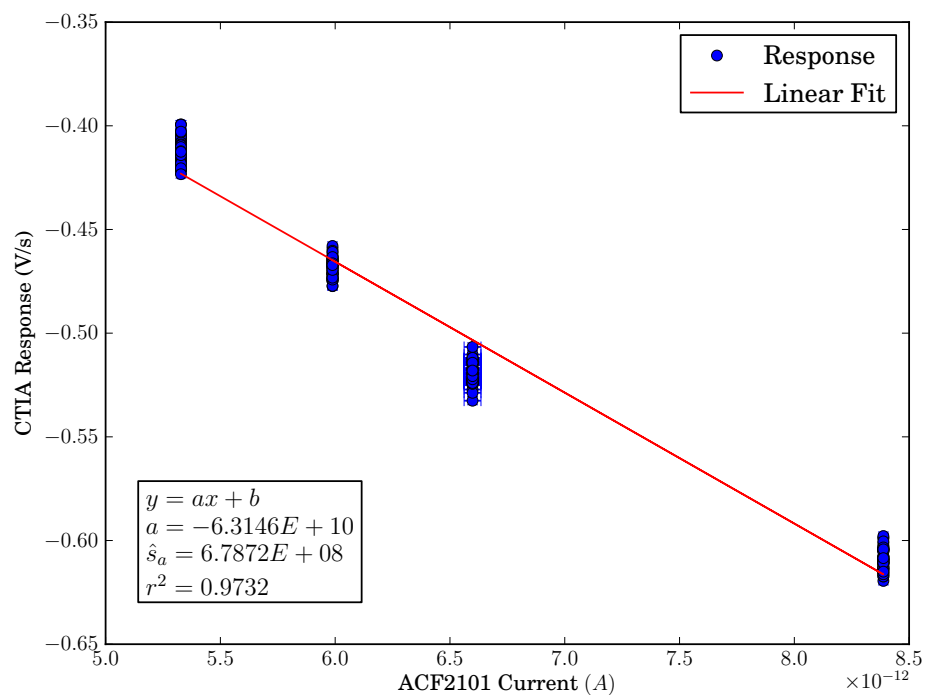


Figure 5.2: Gain calibration curve for low gain. Horizontal error bars represent a 99% confidence interval of the beam current measured by the ACF2101 amplifier. The wide spread in response is due to instability of the ion gun used to make the measurement.

-	High Gain	Low Gain
Gain $V/(A \cdot s)$ :	$-9 \pm 1 \times 10^{13}$	$-6.3 \pm 0.3 \times 10^{10}$
Gain (per charge):	$-14.5 \pm 0.9 \mu V$	$-10.1 \pm 0.6 nV$
Feedback Capacitance:	$11.0 \pm 0.3 fF$	$15.8 \pm 0.3 pF$

Table 5.1: Measured gains for the DM0025 in high and low gain. Errors are reported as 99% confidence intervals.

with higher filament currents and because lower currents were not visible in low gain, there was only a narrow range of beam currents that could be used for calibration.

High gain was characterized by setting the ion gun to a fixed beam current, illuminating the detector with the ion beam, and comparing the signal difference between high and low gain. Backgrounds were collected in the same manner as they were for low gain. The gain factor was calculated by averaging the ratio between high and low gain for the 15 pixels at the maximum of the peak formed by the ion beam. The measured gain difference between high and low gain was found to be  $1435 \pm 94$ . The final gain characterization for the DM0025 in high and low gain can be seen in Table 5.1.

## 5.2 Dark Current Characterization

The dark current is an important parameter of a detector, as it is one of the primary sources of noise. In addition, the dark current sets the maximum integration time, which is the time it takes to accumulate enough charge from the dark current to produce the maximum output signal. As with other types of silicon array detectors,

the dark current is also heavily dependent on temperature.

### 5.2.1 Experimental Procedures

Using the thermoelectric cooler, the device was cooled to a series of temperatures to study the temperature dependance of various parameters. The device output due to dark current was measured for both high and low gain at each temperature using the data-acquisition-for-all-pixels procedure described in Chapter 4.3. The device output was sampled for 40 acquisitions without resetting the integrator (non-destructively) and the experiment was repeated 100 times. The detector was allowed to come to thermal equilibrium at each temperature.

### 5.2.2 Results

The dark current magnitude was computed by calculating a linear regression fit for each loop and then averaging the slopes together for each pixel at each temperature. The dark current as a function of temperature is shown in Figure 5.3. The error bars in the plot are computed for a 99% confidence interval based on the variance of the slopes for each pixel at each temperature. At low temperatures these errorbars are small enough that they are not visible on the plot. The dark current originated from leakages at the gate of the two input transistors, so it was the same for high and low gain.

The dark currents exhibited an exponential decay as a function of temperature

with the dark current magnitude decreasing by about 50% for every 8-10 degrees C, which is similar to other silicon detectors (63). Most of the pixels converged toward the same dark current ( $\approx 0$ ), with a single exception. This pixel decreased to zero, and then changed direction. The measured dark current actually is the sum of a number of currents, the two most prominent are assumed to be the currents into the gates of the field effect transistors that make up the inputs to the pre-amplifier. The net dark current is the sum of these two currents (66). Because of random mismatch in device fabrication these currents do not cancel each other out, leading to net dark current. Because variances add, the noise from this dark current, which will be discussed later, is due to the sum of the variances from each of the separate currents. Therefore, to minimize the noise, it is important to minimize both these currents, and not just their difference.

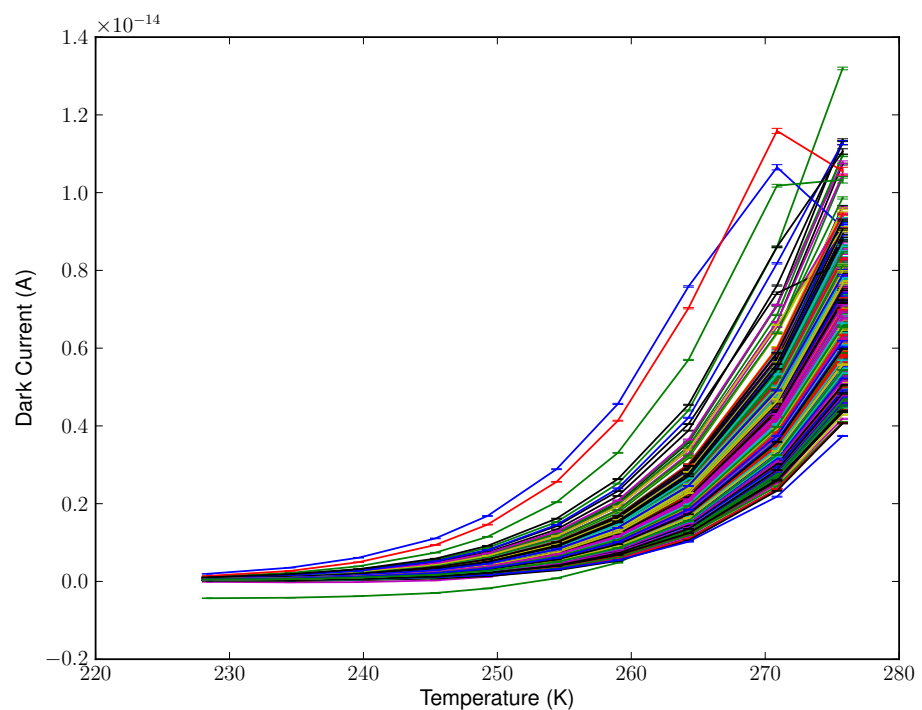


Figure 5.3: Dark current magnitude vs temperature of the DM0025. Error bars are 99% confidence intervals calculated from the variance of the slope estimator at each temperature. The dark current magnitude decreases by about 50% every 8-10 degrees C.

### 5.3 Temperature Dependence of the Post Reset Voltage

Because of inconsistencies in manufacturing, each pixel had a different bias voltage. These differences in bias voltage should have been gain independent and have an effect on the range over which each pixel could integrate, thus affecting the pixel charge capacity. The data for characterizing the post reset voltage as a function of temperature were the same data collected in Section 5.2.1.

#### 5.3.1 Results

The voltages for each pixel after reset are shown at 276K and 228K for both high gain in Figures 5.4 and 5.5, and for low gain in Figures 5.6 and 5.7. The distribution of post-reset voltages in low gain matched the distribution of global reset voltages (Figure 4.4), while those in high gain did not (Figure 4.3). Because global resets produce strange behavior, the last reset before reading is a cycle through individual channel resets. This means that the device goes through up to 1696 clock cycles between the last channel reset on a pixel and when the pixel is read out. When sample-and-hold was used, there was a different amount of time between coming out of reset and the first sample time for different pixels. In low gain, each pixel moves slowly away from its starting voltage, so this is an insufficient amount of time for a significant change in voltage. In high gain, however, each pixel moves more rapidly away from its starting voltage than in low gain, so during this time there is a significant change from starting voltage.

The post-reset voltages had a slight dependance on temperature. In high gain, there was no discernible pattern: for some pixels the post-reset voltage decreased as temperature decreased while for others the post-reset voltage increased as temperature decreased. In low gain the pattern was more clear, and the distribution of post-reset voltages became smaller as temperature decreased.

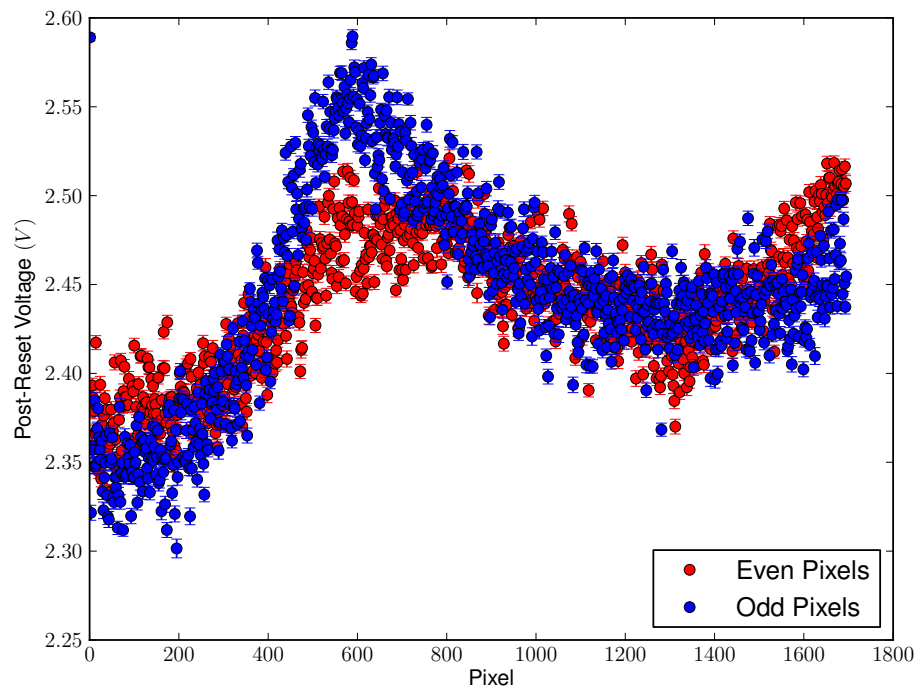


Figure 5.4: Post-reset voltage with the device in high gain at 276K. Data points were computed from the average of 100 data points, and error bars represent 99% confidence intervals. The distribution of post-reset voltages in high gain at 276K is different from the distribution of post-reset voltages in high gain at 228K, but not in a systematic manner.

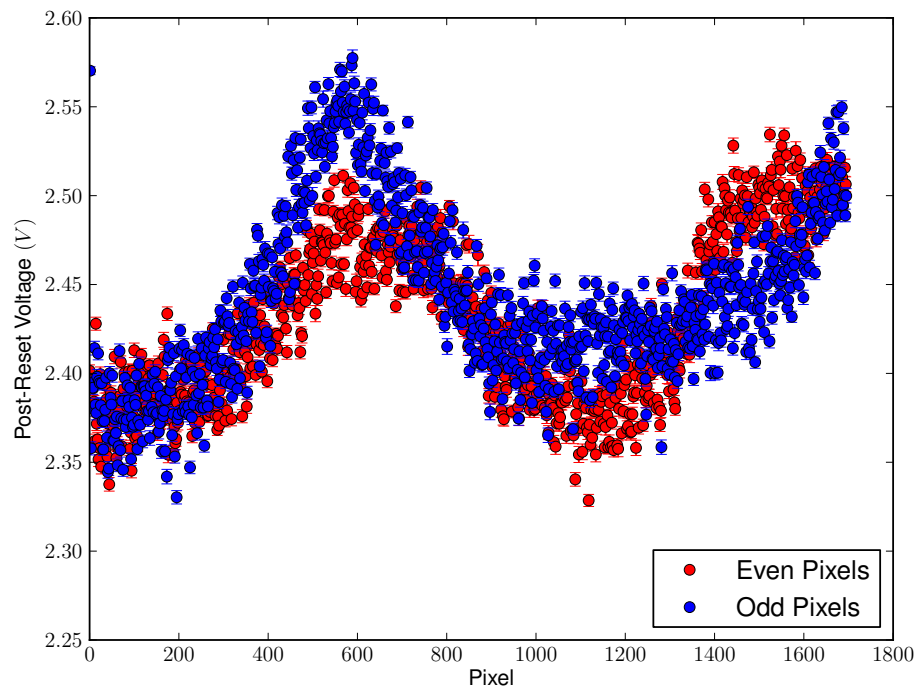


Figure 5.5: Post-reset voltage with the device in high gain at 228K. Data points were computed from the average of 100 data points, and error bars represent 99% confidence intervals. The distribution of post-reset voltages in high gain at 228K is different from the distribution of post-reset voltages in high gain at 276K, but not in a systematic manner.

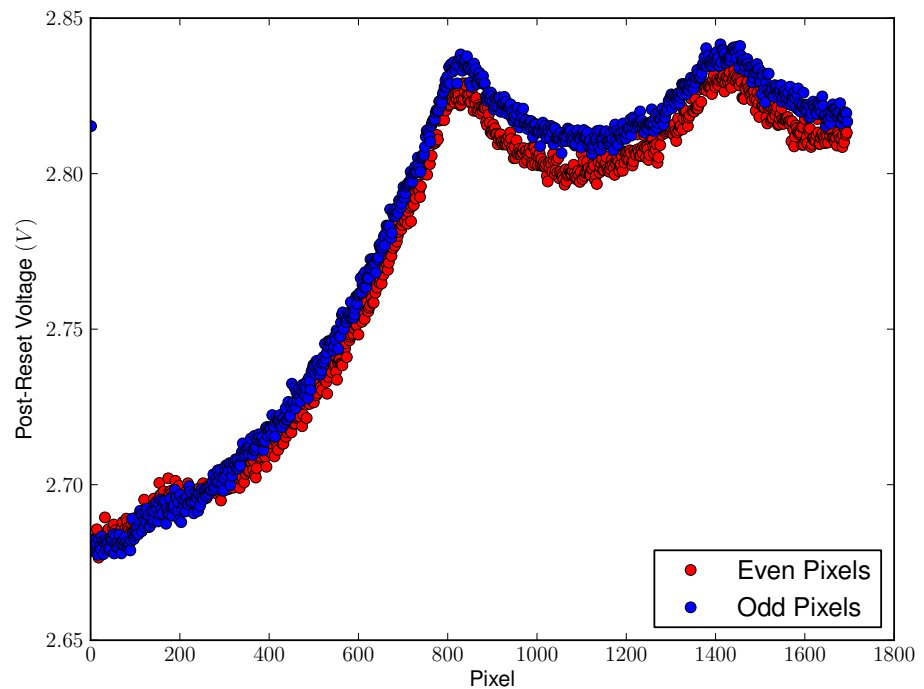


Figure 5.6: Post-reset voltage with the device in low gain at 276K. Data points were computed from the average of 100 data points, and error bars represent 99% confidence intervals. The distribution of post-reset voltages in low gain at 276K is wider than at 228K.

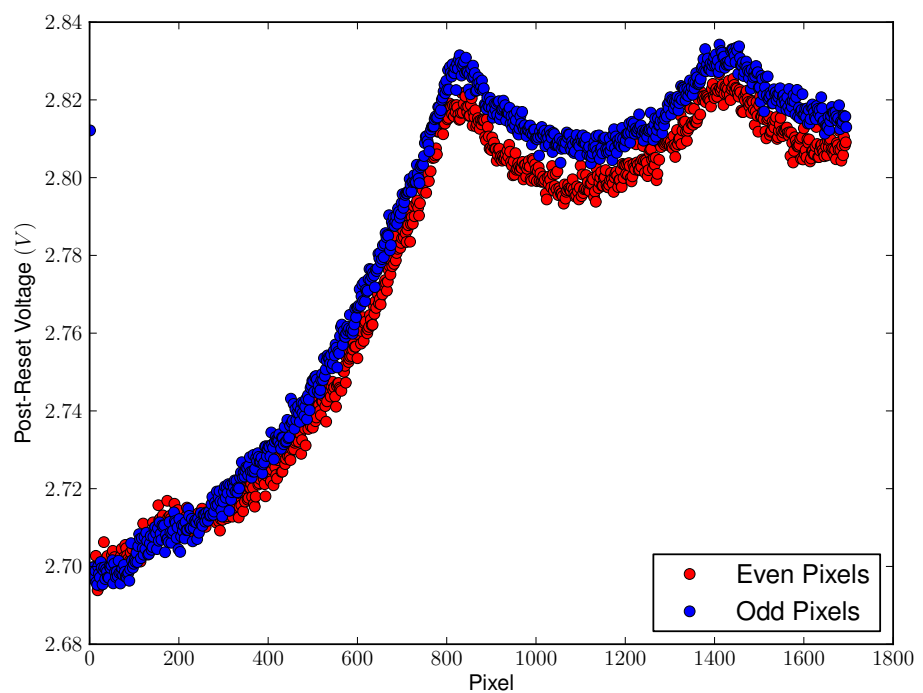


Figure 5.7: Post-reset voltage with the device in low gain at 228K. Data points were computed from the average of 100 data points, and error bars represent 99% confidence intervals. The distribution of post-reset voltages in low gain at 228K is narrower than at 276K.

To better characterize post-reset behavior, the basic operating procedure was modified so the command sequence to read a pixel consisted of an individual channel-reset immediately followed by a read, instead of just a read. The post-channel reset voltages for high and low gains are shown in Figure 5.8 and Figure 5.9. These plots show the average voltage of each pixel immediately after reset. In high gain, each pixel undergoes a rapid exponential change in voltage away from its starting voltage within the first  $20 \mu\text{s}$ , as seen in Figure 5.10. Because the device was clocked at 123.50 kHz ( $\sim 8 \mu\text{s}$  period), it took only a few clock cycles for each pixel to move away from its original post-reset voltage toward the distribution in Figure 5.5. It is also interesting to note that the odd pixels, i.e. those on the second shift register, exhibited the same post-reset distribution as they did in global reset and as they did in low gain. The distribution of the even pixels, i.e. those on the first shift register, had the same shape as the odds but was shifted down by about 0.15 V. The origins of this behavior, as well as that of the sharp exponential voltage change in high gain, are unknown.

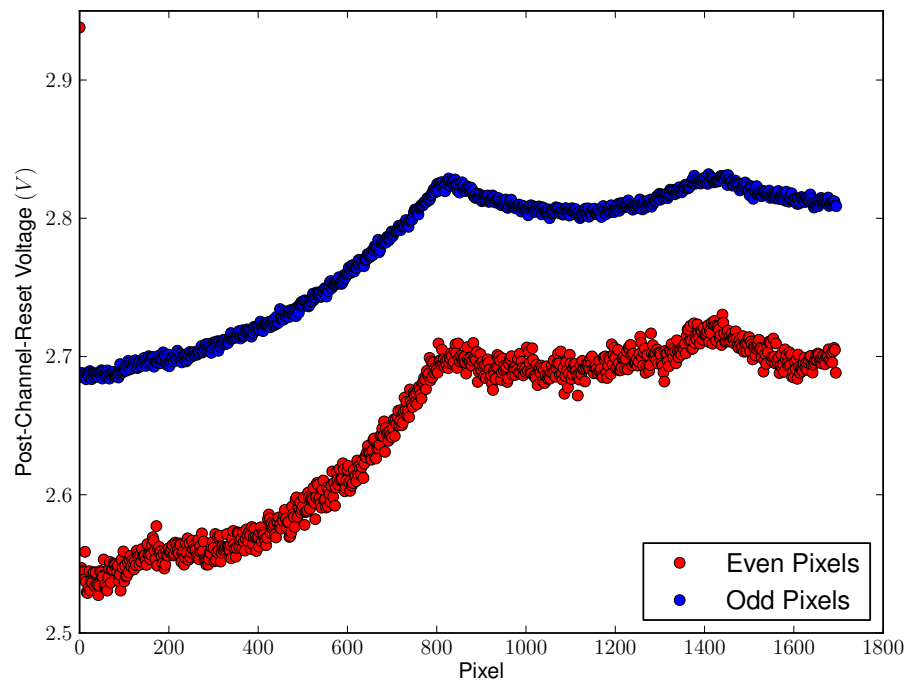


Figure 5.8: Post-channel-reset voltage with the device in high gain. Data points were computed from the average of 50 data points, and error bars represent 99% confidence intervals. Half of the pixels (the odd pixels) match the global reset voltage distribution in high gain (Figure 4.3), while the even pixels are shifted down by about 0.15 V. The origin of this behavior is unknown.

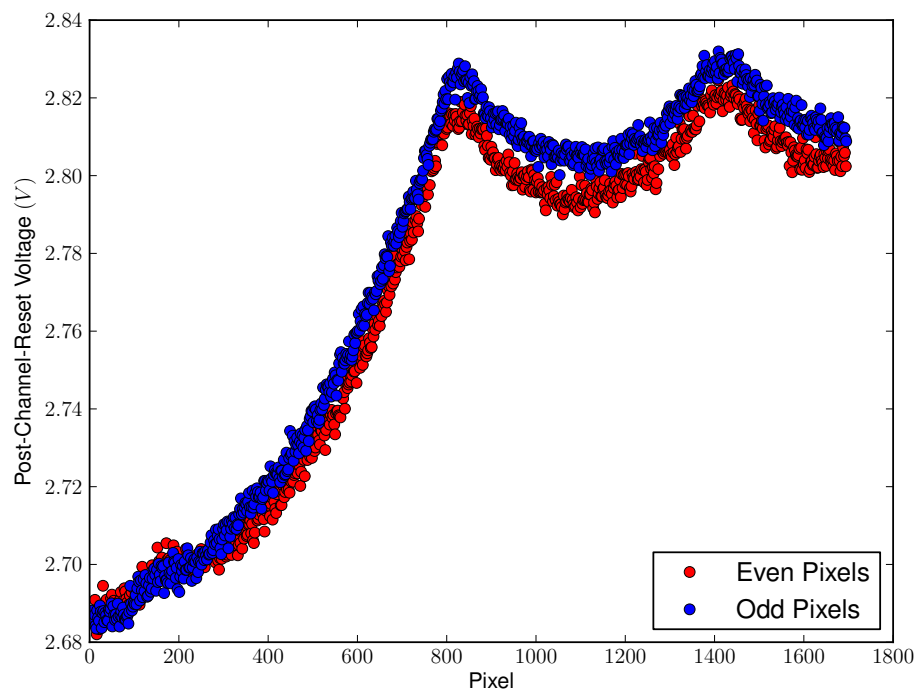


Figure 5.9: Post-channel-reset voltage with the device in low gain. Data points were computed from the average of 50 data points, and error bars represent 99% confidence intervals. This distribution matches the distribution of voltages when the device is in global reset and in low gain.(4.4)

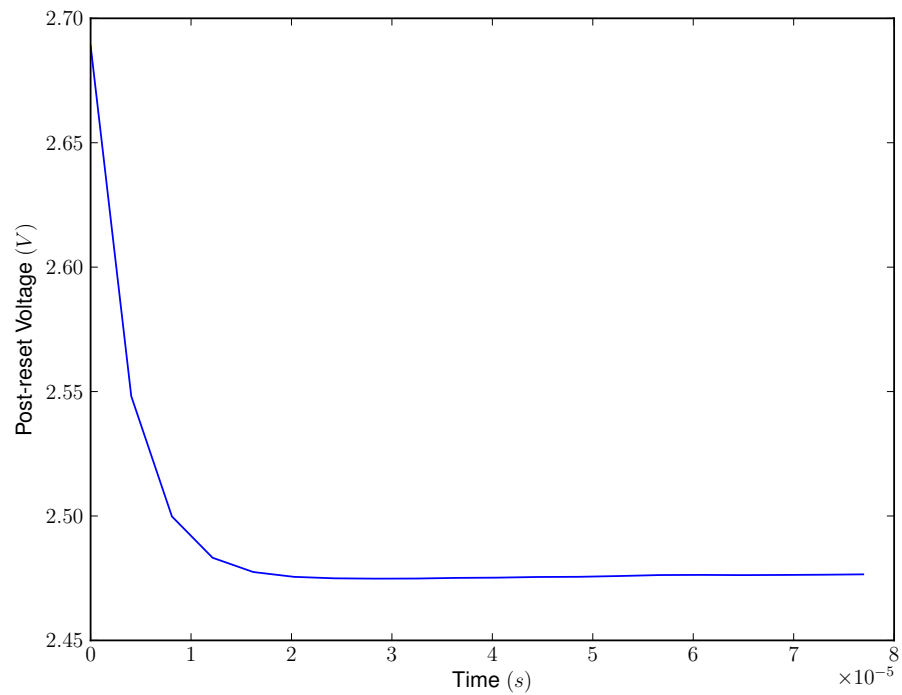


Figure 5.10: Post-reset voltage vs time for pixel 500 with the device in high gain. This rapid exponential change in voltage is responsible for the shift in voltage distribution in high gain when the device comes out of reset.

## 5.4 Sample-and-Hold Circuit Leakage

The sample-and-hold stage allows the DM0025 1696 pixel CTIA array detector to perform true simultaneous detection, even though it takes about 14 ms to read out all of the pixels. It is important to determine the maximum length of time that a sample is held accurately on the sample-and-hold capacitor.

### 5.4.1 Experimental Procedure

To characterize the sample-and-hold circuitry, the single pixel program described above was modified to read the selected pixel for two clock cycles with the sample-and-hold switch closed, then read for an additional 262142 times (about 1 second) with the sample-and-hold switch open. This experiment was repeated 10 times for each pixel.

### 5.4.2 Results

The slopes of the voltage as a function of time for each pixel are plotted in Figure 5.11 for high gain and Figure 5.12 for low gain. There is little difference between even and odd pixels in each gain, but there is a slight difference between high and low gain. It is unclear why there is a difference between high and low gain, as once the sample-and-hold switch is opened, the sample-and-hold circuitry should be disconnected from the first stage. During normal operation the sample-and-hold switch is held open for approximately 14 ms, so the maximum change in voltage due to leakage

when the device is in high gain ( $\sim 0.0002 \frac{V}{s} * 14\text{ ms} \approx 3 \mu\text{ V}$ ) is insignificant.

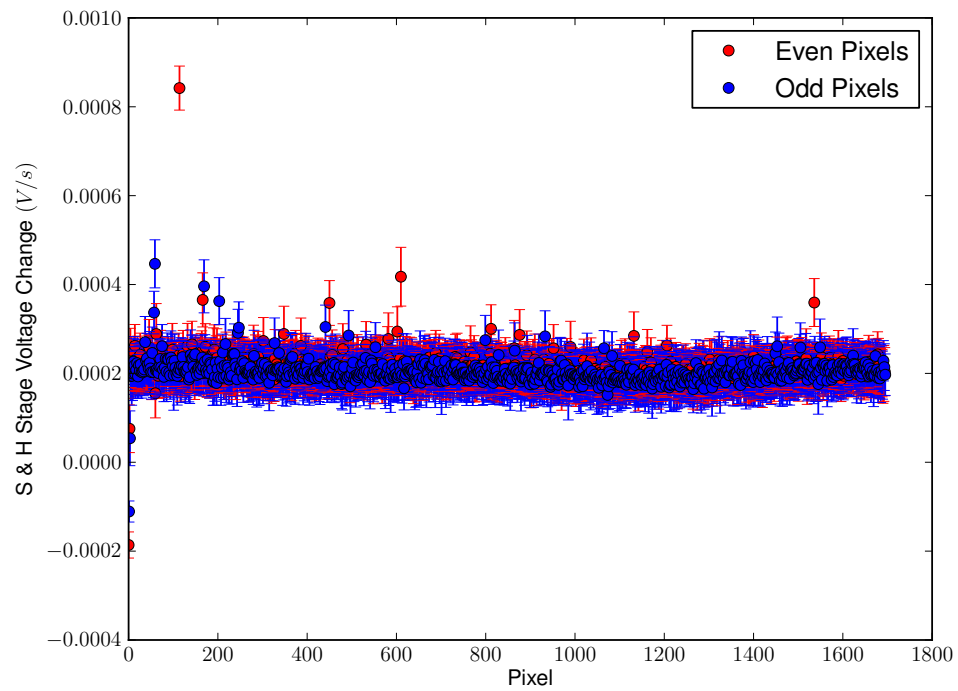


Figure 5.11: Sample-and-hold leakage with the device in high gain. Data points were computed from the average of 10 data points, and error bars represent 99% confidence intervals. While there is some voltage change while the sample-and-hold switch is open, it is insignificant due to the short time the sample-and-hold switch is open.

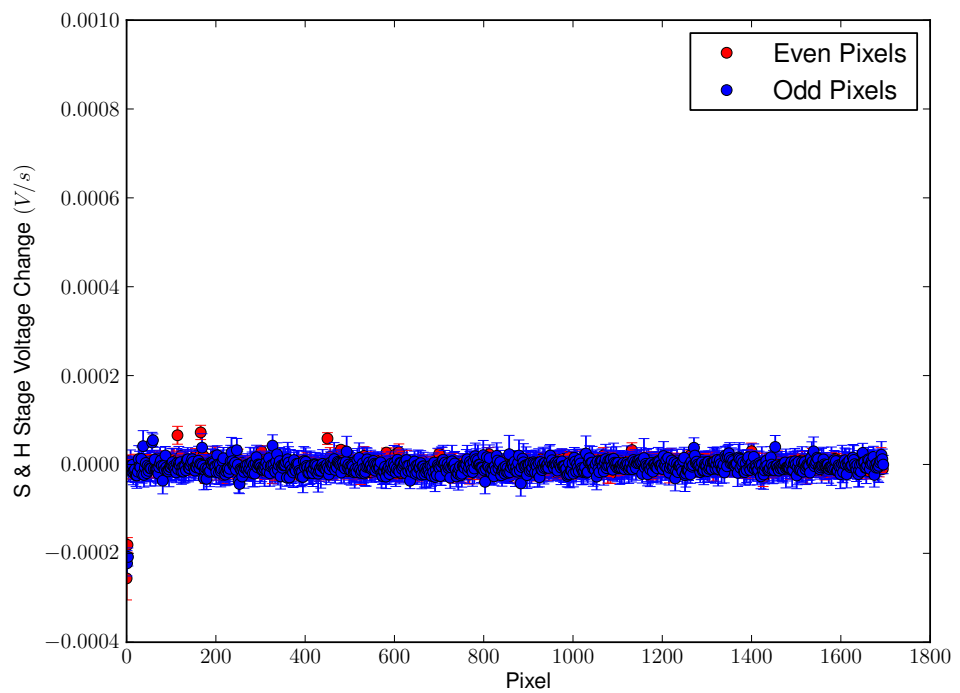


Figure 5.12: Sample-and-hold leakage with the device in low gain. Data points were computed from the average of 10 data points, and error bars represent 99% confidence intervals. There is no visible change in voltage while the sample-and-hold switch is open with the device in low gain.

## 5.5 Noise Characterization of the 1696 Pixel CTIA Detector as a Function of Temperature

Because the typical signal of interest using these devices is an ion current, the measured quantity of interest is the slope of the output, computed by linear regression. The uncertainty in this slope, used to determine the signal-to-noise ratio, is the standard deviation of the slope estimator, known as the standard error, and is calculated using Equation 2.77. It is important to examine the influence of temperature on the standard error to determine the optimal temperature at which to run the device. The standard error is affected by noise from various sources, including read noise and dark current noise. The standard error is easy to compute from an ordinary least squares slope estimator, and is used as the noise in a slope measurement to compute the signal-to-noise ratio.

### 5.5.1 Experimental Procedure

The data were collected according to Section 5.2.1. The estimations of the standard error for the slope of each loop were averaged together for each pixel at each temperature. The error bars in the plot are computed for a 99% confidence interval based on the standard deviation of all of the estimated standard errors for each pixel at each temperature.

### 5.5.2 Standard Error vs Temperature

The plots of standard error vs temperature can be seen in Figure 5.13 for high gain and Figure 5.14 for low gain. In high gain, the standard error decreased rapidly at high temperatures as temperature decreased, while below about 255 K the decrease was much slower. The primary sources of noise that affect the standard error are fluctuations in the dark current, called dark current noise, and fluctuations in voltage, both on the output as well as the input, known as read noise. These two sources of noise will be further investigated in Section 5.6. The dark current noise is highly temperature dependent, while some of the read noise is and some of it is not. In high gain, as temperature decreased, the standard error and, thus, the various noise sources, approached some lower limit. It was unclear, however, whether that limit was reached at 228 K, the lowest achievable temperature with the current cooling configuration.

There appeared to be little to no effect of temperature on the output noise in low gain. The limiting output noise in low gain was approximately 10 times lower than the noise in high gain, while the gain difference was a factor of 1435. This is not a discrepancy because the amplifier has a different gain for currents (Chapter 3.3) than it does for voltages (Chapter 3.27). Due to capacitance on the input, which comes from capacitance between the Faraday fingers and the ground plane below them, capacitance from the input FETs of the pre-amplifier, capacitance from the reset and gain switches, and other sources, the ratio between the voltage gain in

high gain and in low gain should not have been as large as the current gain ratio. For the difference seen here, the total input capacitance would have needed to have been on the order of a few hundred  $fF$ , which is possible for the sources listed. Unfortunately, there was no way to characterize the input capacitance at this time, so its influence could not be investigated further.

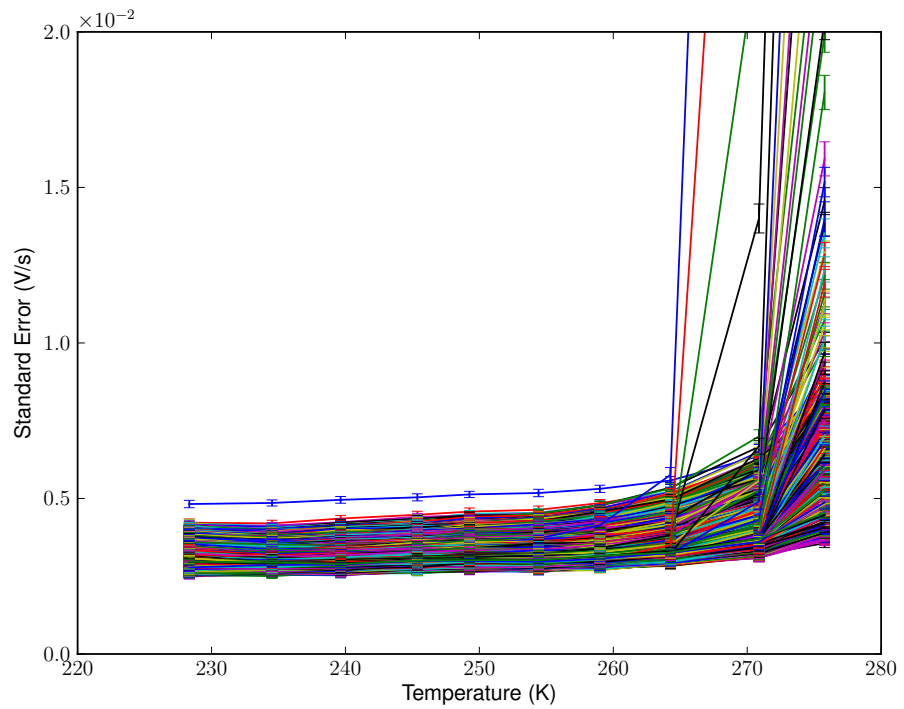


Figure 5.13: Standard error of the slope measured in the dark vs temperature in high gain. The error bars are computed for a 99% confidence interval based on the standard deviation of all of the estimated standard errors for each pixel at each temperature. The standard error is influenced by both the read noise and the dark current noise.

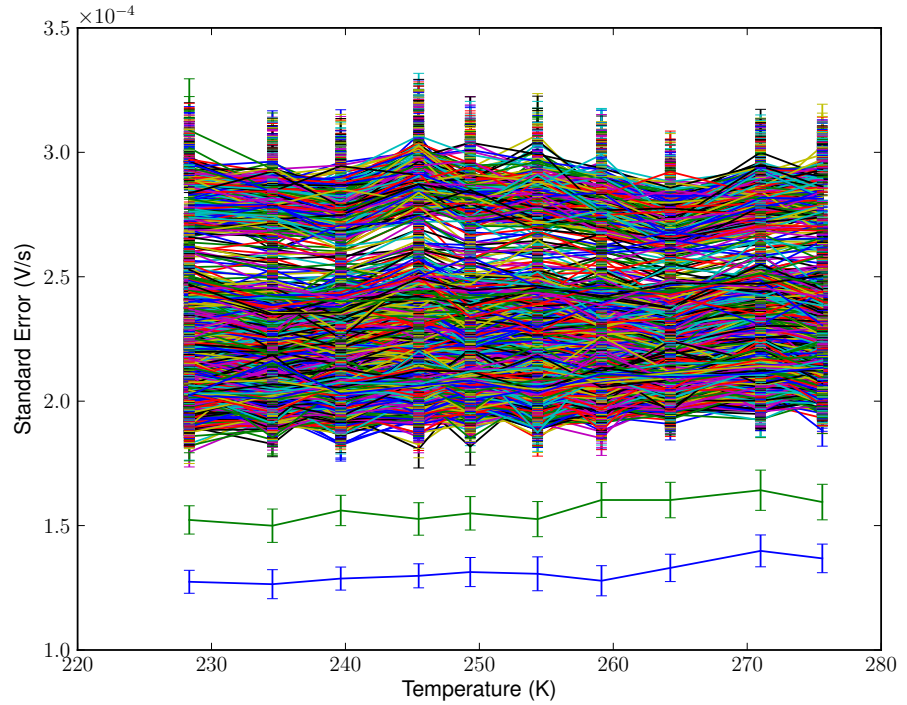


Figure 5.14: Standard error of the slope measured in the dark vs temperature in low gain. The error bars are computed for a 99% confidence interval based on the standard deviation of all of the estimated standard errors for each pixel at each temperature. The standard error is influenced by both the read noise and the dark current noise, though there is no measurable dark current noise in low gain.

### 5.5.3 Post-Reset Noise

A class of noise that does not factor into the preceding standard error, but that affects the dynamic range of the device (Section 5.7.3), is the post-reset noise. When the device comes out of reset, the voltage on the output assumes a random value, around some mean offset voltage. This randomness can arise from several sources, including kT/C noise, read noise, and charge injection noise.

For the CTIA, post-reset noise is manifested during reset. During reset, charge carriers flow back and forth randomly through the reset FET channel onto either side of the feedback capacitor, producing the noise given by Equation 2.85. When the reset switch is opened, however, charge can no longer flow through the FET channel, so some amount of charge is "stuck" on the input side of the capacitor. This random amount of charge produces a random offset voltage, that, over many repetitions, will have a standard deviation given by Equation 2.85.

A second source of post-reset noise is charge injection from the reset FET channel (71). When the reset FET is turned off, the channel does not close immediately, and as it closes, there are still charge carriers left in the channel. These charge carriers leave the channel, through the source, the drain, and the gate, so some of these carriers exit the channel on the input side of the capacitor, creating an offset voltage. The reset switch in the DM0025 actually consists of two FETs, set up in such a way that their charge injections approximately cancel, minimizing the amount of charge injection, and thus the offset voltage. This charge injection is a

random process, however, so there is some variability in the total number of charges that are deposited on the input when the switch opens. This manifests itself as a noise in the offset voltage just after reset, similar to  $kT/C$  noise.

The post-reset noise for high and low gain are shown in Figures 5.15, and 5.16 respectively. The envelope made by the dotted lines represents the spread of the noise values due to pixel variation. The measured "first sample noise" is the standard deviation of the first voltage measured after reset. The measured output noise is the estimation of the output noise from linear regression. From Equation B.1, the noise of the first measured voltage should be the sum of the post-reset voltage noise and the output noise. For high gain, the measured output noise is about a factor of ten lower than the first sample noise, indicating that most of the first sample noise is post-reset noise. The magnitude of this noise is several orders of magnitude greater than the expected  $kT/C$  noise, so it is likely that most of this post-reset noise is due to charge injection. If it were all charge injection, it would correspond to a standard deviation of about 1450 charges on the input. For low gain, there is no discernible difference between the measured output noise and the noise of the first sample, indicating that most of the noise in the first sample is due to output noise. Charge injection should result in a fluctuation of the same number of charges on the input, regardless of the gain, because the same switch is used for both. The gain does determine the magnitude of the output voltage fluctuations due to these charge fluctuations. If the post-reset noise in high gain were due to a charge injection

fluctuation of around 1450 charges, the voltage fluctuation in low gain would be about  $1.5 \times 10^{-5}$  V, which would add an insignificant contribution to the measured first sample noise. The data from low gain does not contradict the supposition that the post-reset voltage noise in high gain is caused primarily by charge injection.

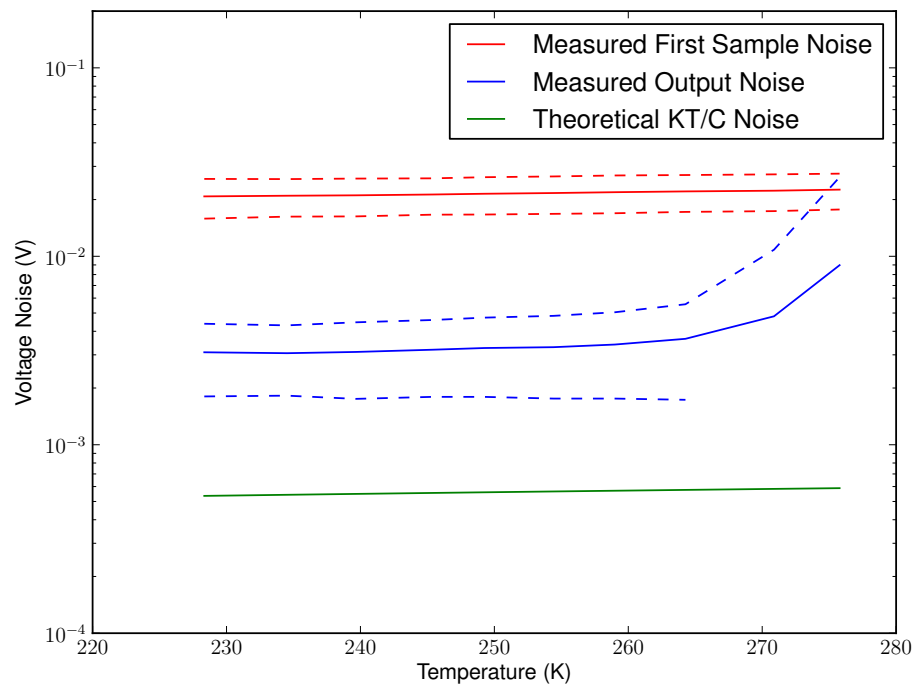


Figure 5.15: Various sources of post-reset voltage noises in high gain. The dotted lines represent the spread in noise values due to pixel variation. A large component of the measured first-sample noise believed to be due to variance in charge-injection as the reset switch opens.

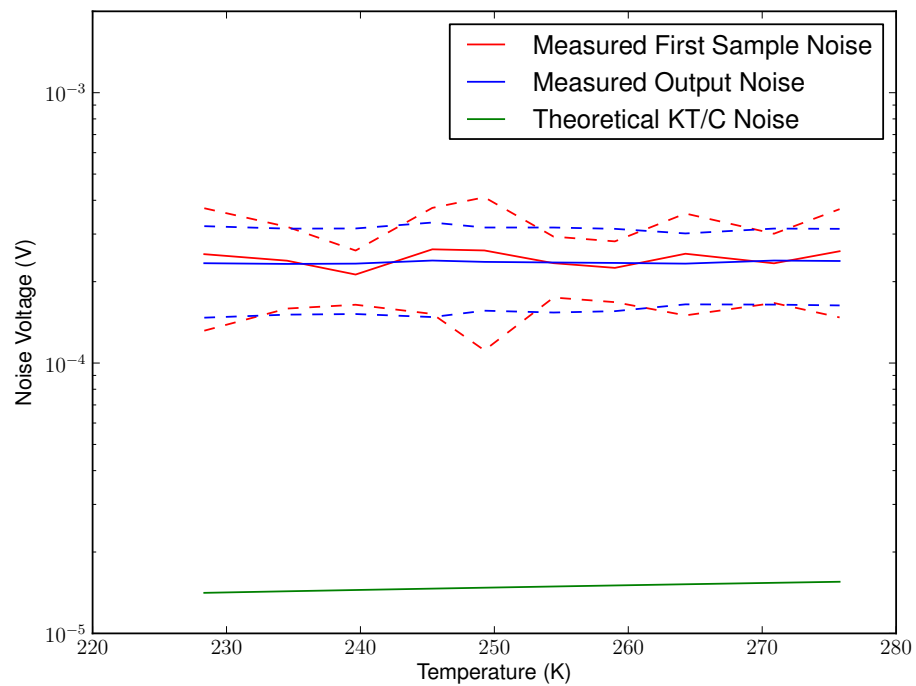


Figure 5.16: Various sources of post-reset voltage noises in low gain. The dotted lines represent the spread in noise values due to pixel variation. The measured first-sample noise comes from noise on the output.

## 5.6 In-Depth Noise Characterization of the DM0025 at 228K

The measured noise of the device comes from a variety of locations in the amplification chain, as each stage in the chain adds its own noise. The total noise measured, therefore, comes not only from the pre-amplifiers, but also from the sample-and-hold stage, the output buffers in the device, the voltage followers on the daughter board, and the analog to digital converter. To fully characterize this noise, the amplification chain must be broken at each stage and the noise measured after each stage. Ideally, first the analog to digital converter noise would be measured with the rest of the chain removed. The voltage follower plus the ADC would then be measured. The ADC noise would then be known from the first experiment, so the follower noise could be extracted from the measured noise of the follower plus ADC. In this manner, each piece of the amplification chain could be added on and the noise of the system measured to determine the noise contribution of each stage to the total noise. Unfortunately, because several of the stages are inside the DM0025 chip, they could not be separated out. Additionally, because the DM0025 was wire bonded to the daughter board, the voltage followers could not be characterized without breaking the wire bonds. Once broken, the wire bonds cannot be reattached to the DM0025, so characterizing the follower would result in a destroyed device. Because the follower amplifiers are commercial components (a Linear LTC6244HV, dual op-amp), their noise performance can be approximated from the manufacturers specification sheet (72). Based on these data, the daughter board buffer amplifiers

do not contribute a significant amount of noise to the overall amplification chain. For these reasons, the amplification chain was only divided into the following groups: 1) Analog to digital converter, 2) sample-and-hold stage plus chip output buffers plus daughter board voltage followers, and 3) pre-amplifiers. The noise contributions derived for these three groups in the amplification chain are detailed below.

### 5.6.1 Noise from the Sample-and-Hold Stage

Because the analog to digital converter (ADC) was characterized separately (see Appendix B), the first portion of the amplification chain characterized here was the sample-and-hold stage group. Noise in this group includes noise from the sample-and-hold stages themselves, noise from the DM0025 output buffers, noise from the follower amplifiers on the daughter board, as well as noise from the ADC.

#### 5.6.1.a Experimental Procedure

The noise passed from the sample-and-hold stage to the analog to digital converter was characterized using the data collected according to procedure detailed in Section 5.4. The standard deviation of the output voltage for each pixel's sample-and-hold stage is shown in Figure 5.17 for the device in high gain and Figure 5.18 for the device in low gain. This noise includes contributions from the sample-and-hold amplifiers, the device output buffers, the follower amplifiers on the support board, and the analog to digital converter (ADC). The noise of the ADC was measured

separately(see Appendix B) and was found to be  $6.99 \pm 0.01E^{-5}$  V to 99% confidence.

### 5.6.1.b Results

The measured noise from the sample-and-hold stage with the device in high and low gains is shown in Figures 5.17 and 5.18 respectively. As discussed in the introduction to this chapter, the noises presented in Figures 5.17 and 5.18 are referred to the output of the DM0025, so they were a factor of 2.00 times smaller than the noise in the signal at the input of the analog to digital converter due to the presence of the buffer amplifiers on the daughter board. This means that the noise from the sample-and-hold stage measured at the analog to digital converter was 2.00 times greater than what was presented in Figures 5.17 and 5.18. Because variances add (noise is represented as a standard deviation, or the square root of the variance), if the ADC noise were a factor of ten lower than the other noises being measured, it would only add an error of about 0.5%. In this case, however, the noise of the ADC by itself was only a factor of about 1.6 lower than the measured noise from the sample-and-hold stage. Because this measured noise included both the noise from the sample-and-hold stage and the ADC, and, because variances add, the noise from the sample-and-hold stage was only slightly larger than the noise from the analog to digital converter. This similarity made it difficult to clearly separate the noise from the analog to digital converter from the noise due to the remaining stages.

The noise from the ADC could be reduced in several ways. First, the analog to digital converter uses 18 bits with an input range of 20V, so the least significant bit(LSB) is about  $76 \mu\text{V}$ . Due to digitization noise, the output of the analog to digital converter fluctuates a few LSB. If the ADC had more bits, the LSB would have been smaller, so the fluctuations would be smaller, lowering the noise contribution from the ADC. Commercially available analog to digital converters with more than 18 bits are, however, significantly slower than 18 bit ADCs, which is not desirable (See Chapter 3.4.3). Shrinking the ADC range could also lead to a lower noise contribution from the analog to digital converter. The National Instruments 6281 (NI 6281) card is limited to bipolar input ranges, meaning its input range is always centered about zero, and extends from some positive reference voltage  $+V$  to  $-V$ . In addition, the NI 6281 has a limited number of ranges:  $\pm 100 \text{ mV}$ ,  $\pm 200 \text{ mV}$ ,  $\pm 500 \text{ mV}$ ,  $\pm 1 \text{ V}$ ,  $\pm 2 \text{ V}$ ,  $\pm 5 \text{ V}$ , and  $\pm 10 \text{ V}$ . The DM0025 requires  $+3.3 \text{ V}$  power supplies so the maximum output voltage range the device could produce is 0 to  $3.3 \text{ V}$ . The buffer amplifiers on the daughter board have a gain of 2.00 so the maximum voltage range measured at the analog to digital converter is 0 to  $6.6 \text{ V}$ . To measure all signals of interest, therefore, the NI card must be run using its  $\pm 10 \text{ V}$  range, for a total range of 20V. Unfortunately, this means more than half of the ADC range is lost, because the DM0025 never outputs negative voltage. By using an analog to digital converter with a more configurable input voltage range, the output of the DM0025 and voltage follower could have filled more of the ADC range, thus lowering

the noise contribution from the ADC.

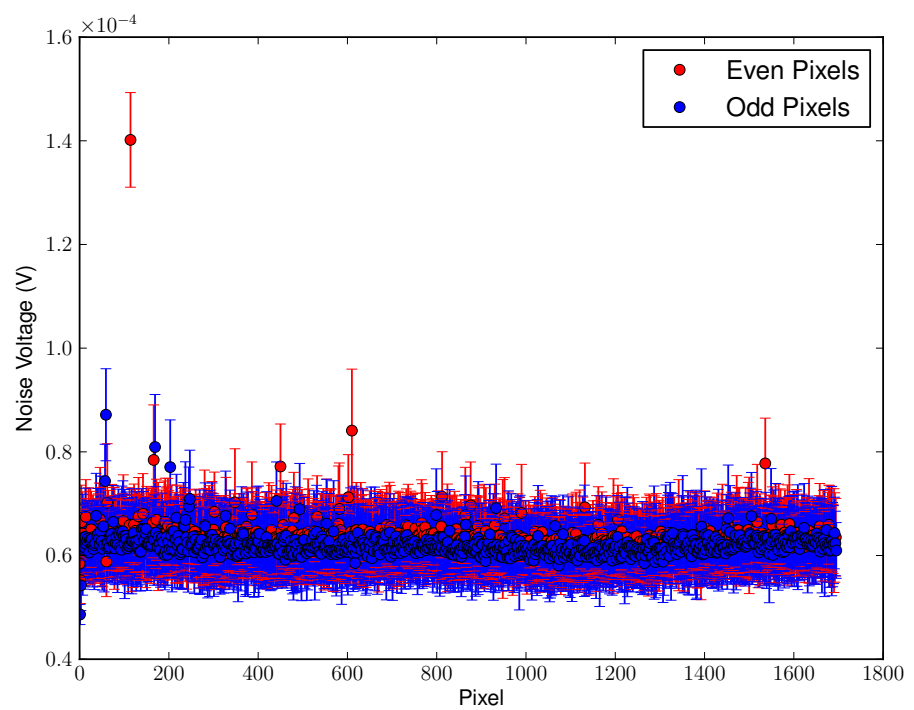


Figure 5.17: Noise from the sample-and-hold stage with the device in high gain. Error bars represent 99% confidence intervals computed from the standard deviation of 40 values. A significant portion of this noise comes from the ADC used to make the measurements.

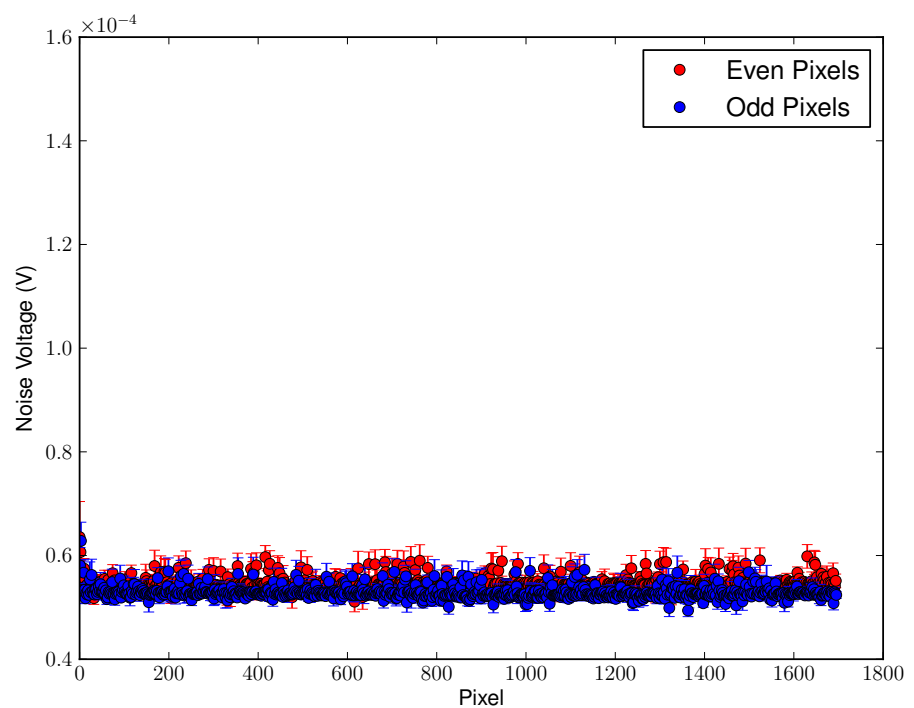


Figure 5.18: Noise from the sample-and-hold stage with the device in low gain. Error bars represent 99% confidence intervals computed from the standard deviation of 40 values. A significant portion of this noise comes from the ADC used to make the measurements.

### 5.6.2 Noise in Reset

The next break in the amplification chain was measured with the amplifiers in reset. The noise at this stage included all the previous noise from the ADC, buffers, and sample-and-hold stage, as well as the noise on the output of the pre-amplifiers, and the unamplified noise on the input of the pre-amplifiers.

#### 5.6.2.a Experimental Procedure

These data were collected using the data acquisition for all pixels procedure described in Chapter 4.3. The output of the device in global reset was sampled 40 times, and the experiment was repeated 100 times. The sample-and-hold switch was left closed, so there was no switching noise from the sample-and-hold switch. Furthermore, as detailed in Chapter 4.4, the device could not operate in high gain with both the global reset switch closed and the sample-and-hold switch open.

#### 5.6.2.b Results

By comparing Figures 5.17 and 5.18 with Figures 5.19 and 5.20, it is clear there is little difference between the noise in reset and that from the sample-and-hold stage, buffers, etc. As discussed in Section 5.6.1, the noise from the analog to digital converter contributed significantly to these measurements, making it difficult to determine the true noise in reset. The noise in reset was a little lower than the noise from the sample-and-hold stage, buffers, etc.. The sample-and-hold data was col-

lected with the device in integration mode (not in reset), so it is likely there is some noise contribution from the pre-amplifier stage present in the noise measurements of the sample-and-hold group (Section 5.6.1). This noise could have been transmitted from the pre-amplifier through the sample-and-hold FET switch, or through other circuitry in close proximity to the sample-and-hold stage or output buffers. This hypothesis could be tested by recollecting the sample-and-hold data with the device in reset. Unfortunately, this experiment cannot be performed with the device in high gain because global reset and sample-and-hold mode are incompatible in high gain (See Chapter 4.4).

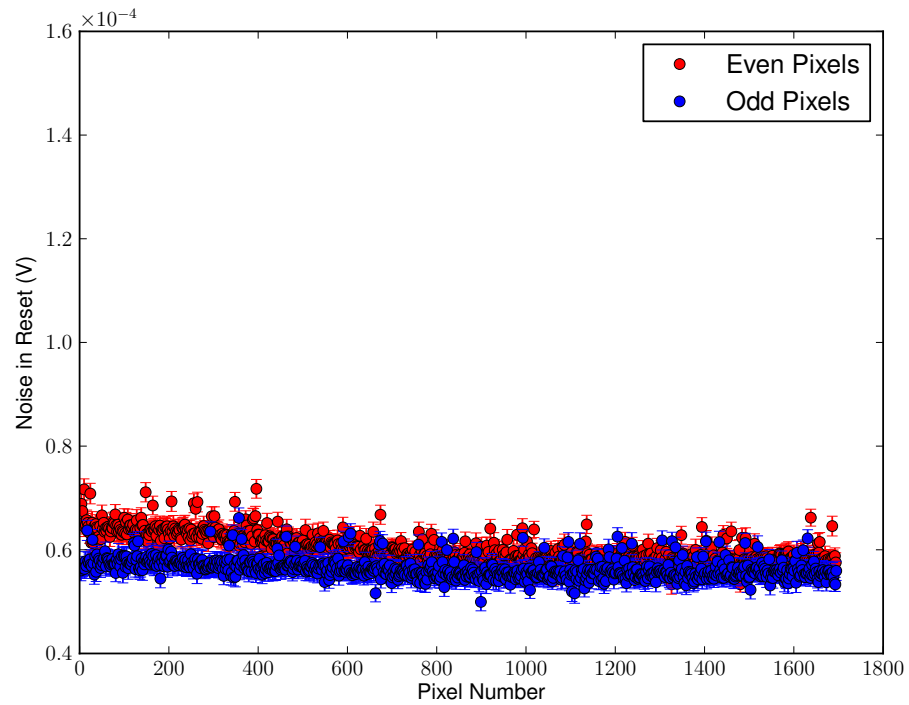


Figure 5.19: Noise with the device in reset in high gain. Error bars represent 99% confidence intervals computed from the standard deviation of 100 measurements. The noise in reset in high gain is lower than the noise from the sample-and-hold stage in high gain (Figure 5.17) because the noise from the sample-and-hold stage was measured while the device was not in reset, due to problems with global-reset and sample-and-hold operation while the device was in high gain (Chapter 4.4).

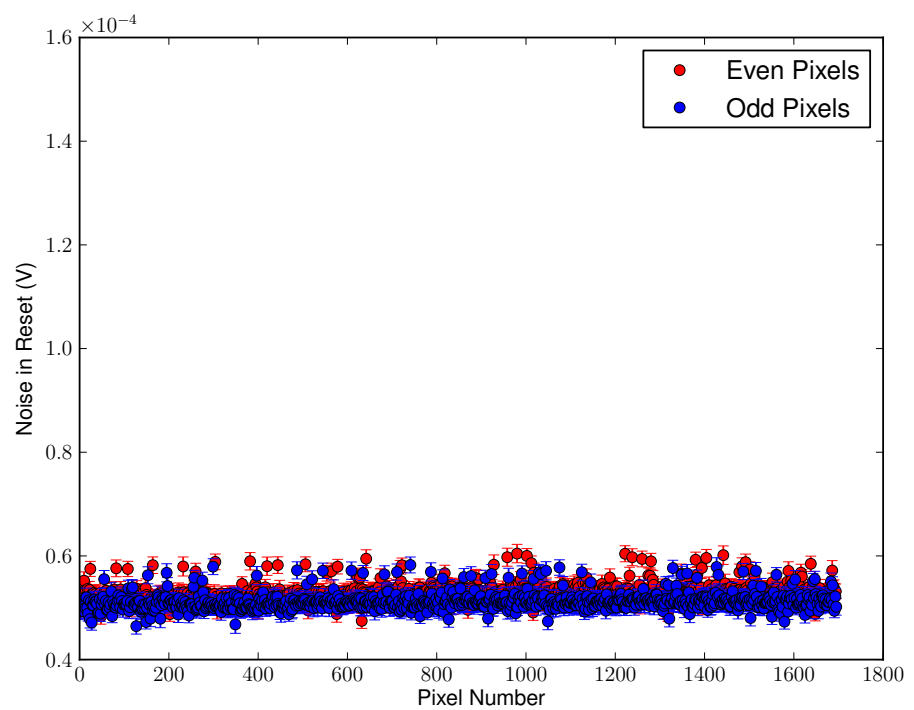


Figure 5.20: Noise with the device in reset in low gain. Error bars represent 99% confidence intervals computed from the standard deviation of 100 measurements.

### 5.6.3 Read Noise and Dark Current Noise

The output voltage at time  $t$  with no input signal can be modeled as

$$V(t) = gi_{dark}t + V_{PR} + \epsilon_{read} \quad (5.1)$$

where  $g$  is the gain,  $i_{dark}$  is the dark current,  $V_{PR}$  is the post-reset voltage, and  $\epsilon_{read}$  is the read noise. The read noise is assumed to come from some statistical distribution with zero mean and unknown variance  $\sigma_{read}^2$  that is independent of output voltage and time. The post-reset voltage offset can be eliminated by normalizing the voltage at time  $t$  with respect to the voltage at time  $t_0$  to obtain:

$$V_{norm}(t) = gi_{dark}t + \epsilon_{read,t} - \epsilon_{read,t_0} \quad (5.2)$$

where the  $t$  and  $t_0$  subscripts on the read noise indicate the sample of the read noise at that time. This normalization totally eliminates the post-reset voltage but doubles the contribution of the read noise to the total variance. From Equation 3.25, the variance of the normalized output as a function of time can be expressed as

$$Var[V_{norm}(t)](t) = g^2\sigma_{dark}^2t + 2\sigma_{read}^2. \quad (5.3)$$

By measuring the output voltage as a function of time due to the dark current, and repeating the experiment multiple times, the variance at each time can be estimated by computing the variance of the normalized repetitions at each sample time. The slope of the variance vs. time is equal to the gain squared times the variance of the dark current and the intercept is twice the read variance.

### 5.6.3.a Experimental Procedure

The dark current noise and read noise of the DM0025 were only characterized at 228K. The output voltage was sampled for 40 acquisitions and the experiment was repeated 1000 times to obtain good statistical estimates of the variance as a function of time. Each repetition was normalized with respect to the first sample of that repetition, and the variance of all the repetitions at each sample time was plotted.

### 5.6.3.b Results

The read noises in volts for high gain and low gain are shown in Figures 5.21 and 5.22. The shape of the read noise as a function of pixel number in high gain closely resembles that of the pixel uniformity in Figure 5.1. This indicates that a large portion of the read noise was noise on the input that was amplified by the feedback capacitors. The read noise in high gain was about 20 times larger than the other characterized noises, so those noises did not contribute significantly to this measurement, making the high gain read noise at the output about 1 mV. The measured read noise in low gain was only about twice the noise measured from the sample-and-hold stage. As discussed in Section 5.6.1, this means that there was a significant contribution from other noises to these measurements. By assuming that the measured read noise in Figure 5.22 is the sum of the actual low gain read noise and the noise measured from the sample-and-hold stage, buffers, etc., in Figure 5.18, an estimation of the average read noise in low gain was  $70 \mu\text{V}$ . This means that the

read noise in high gain was only about 15 times greater than the read noise in low gain, while the gain factor was 1435. As explained before (Section 5.5), this is not unexpected, because the input capacitance plays a large role in the voltage gain but no role in the current gain. Additionally, there are multiple sources that contribute to the read noise on the output, some of which are not influenced by either the voltage gain or the current gain.

Even though the voltage gain is different from the current gain, it is common to convert the output read noise into an equivalent input charge using the charge gain. This enables better comparison between amplifiers with different gains. The input referred read noise and dark current noise for high gain are shown in Figures 5.24 and 5.26. The gain was assumed to be constant across the array, so the read noise in Figure 5.24 has the same shape as in Figure 5.21. The read noise was around 70 charges, which is low, but not nearly as low as for some reported CMOS imagers (73–77). The dark current noise was also fairly low. Dark current noise is a shot noise process, so its noise should be equal to the square root of the number of charges flowing. The average dark current at 228 K was about 100 charges/s, so the shot noise from this should have been about 10 charges/s, but, as previously discussed (Chapter 3.4.1.b), the net dark current is actually a sum of much larger dark currents which partially cancel. Though the dark current magnitudes cancel, their variances add, so the noise in the net dark current is expected to be much larger than just the square root of the net dark current. The contribution of dark

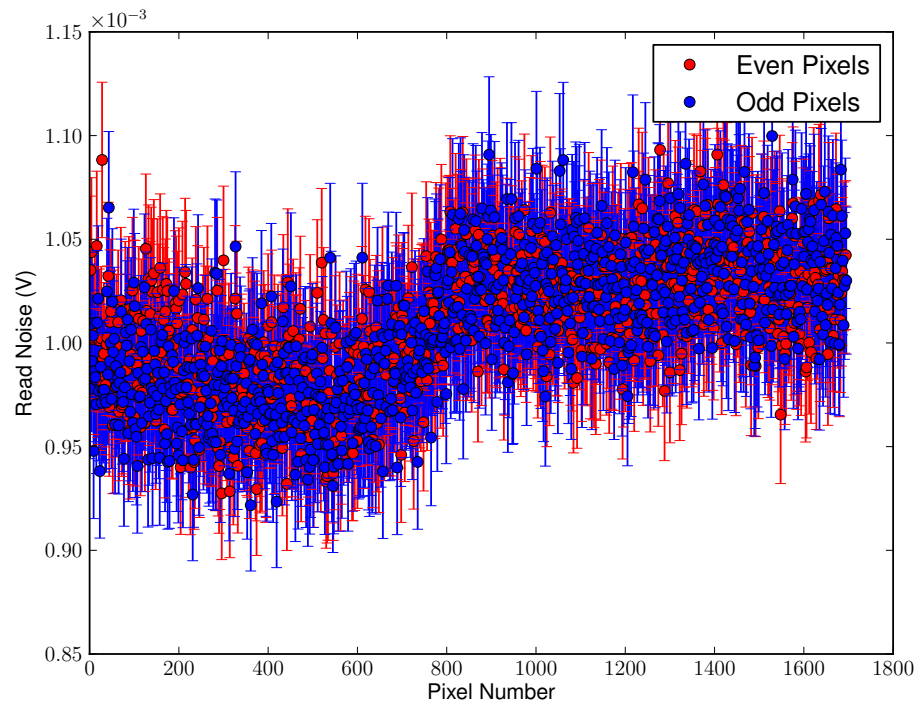


Figure 5.21: Output referred read noise vs pixel for the DM0025 in high gain. Error bars represent 99% confidence intervals computed from the standard deviation of 100 measurements. The shape of the output referred read noise closely matched that of the pixel gain uniformity (Figure 5.1), indicating the source of most of the output read noise is voltage noise on the input of the DM0025 amplifiers.

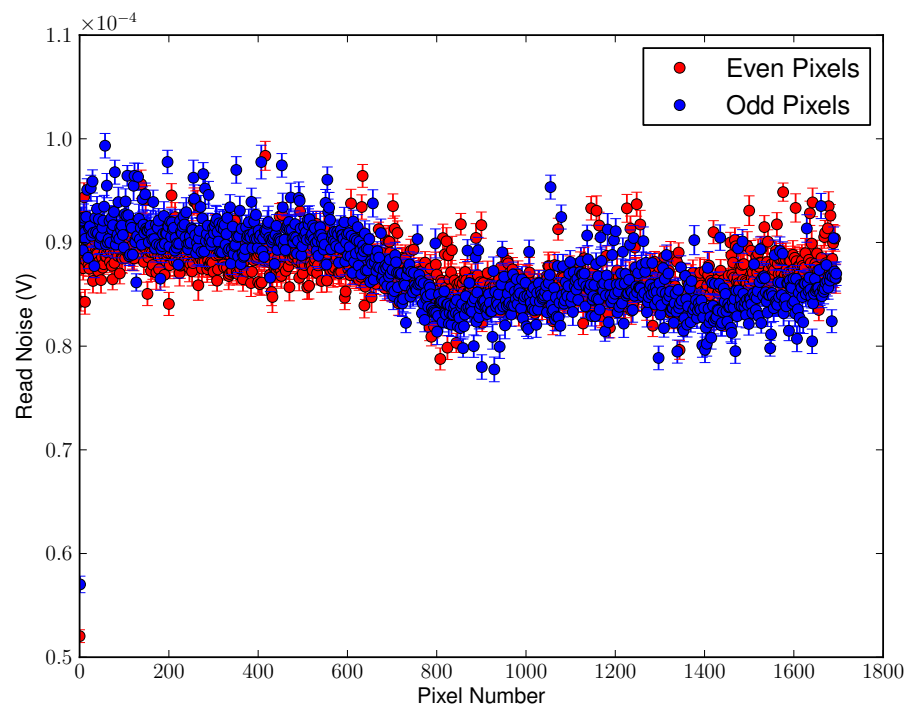


Figure 5.22: Output referred read noise vs pixel for the DM0025 in low gain. Error bars represent 99% confidence intervals computed from the standard deviation of 100 measurements. These measurements are influenced by noise from the sample-and-hold stage, the output buffer amplifiers, and the ADC.

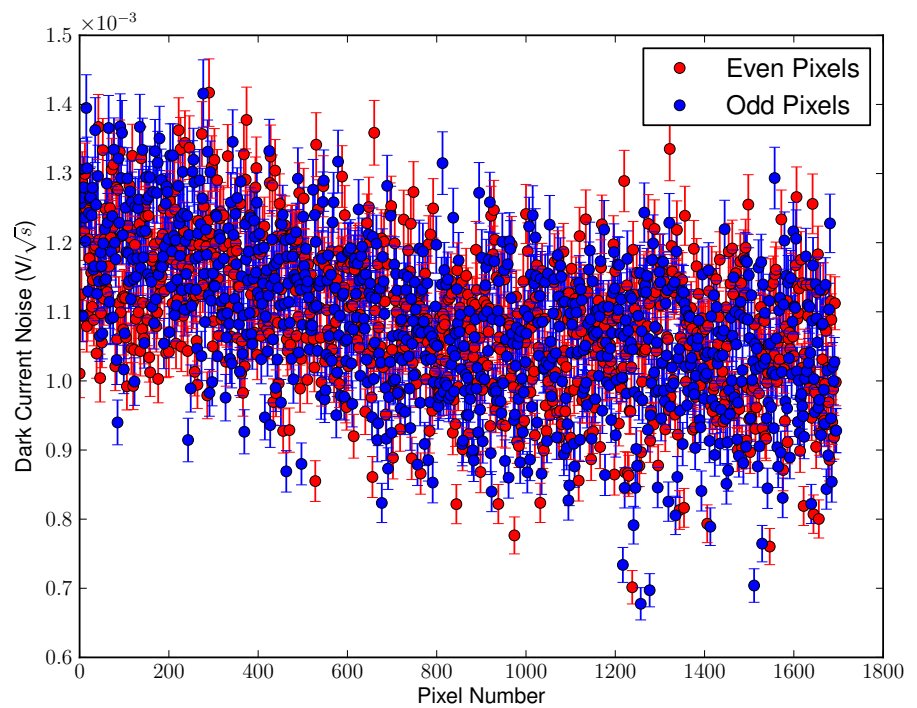


Figure 5.23: Output referred dark current noise vs pixel for the DM0025 in high gain. Error bars represent 99% confidence intervals computed from the standard deviation of 100 measurements.

current noise to the total output noise in low gain was not measurable, so no plot is shown.

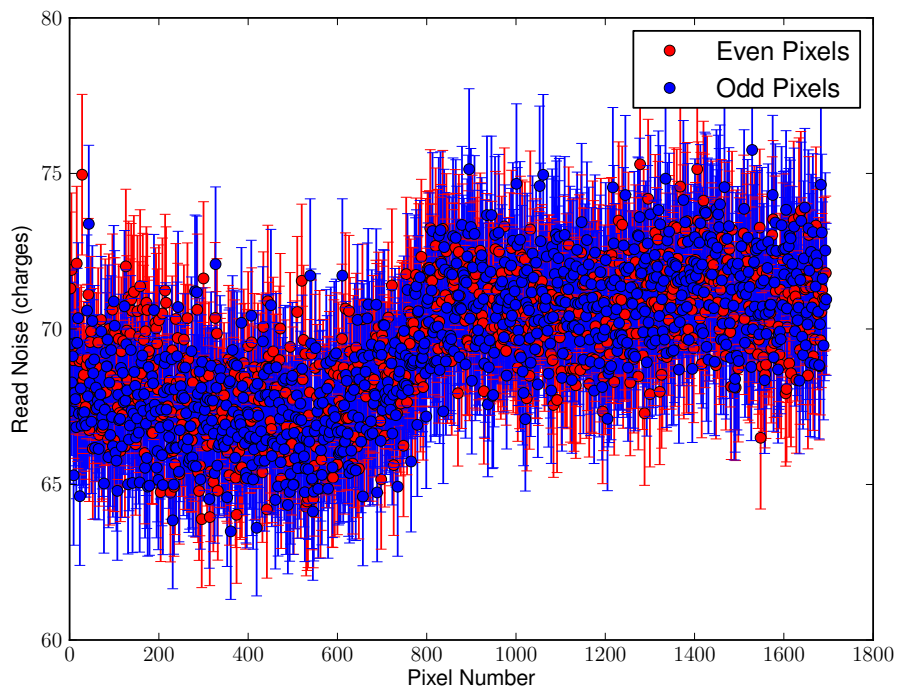


Figure 5.24: Input referred read noise vs pixel for the DM0025 in high gain. Error represent 99% confidence intervals computed from the standard deviation of 100 measurements. The output referred read noise was converted to input referred read noise using the gain determined in Section 5.1, so the shape of the plot is the same as Figure 5.21.

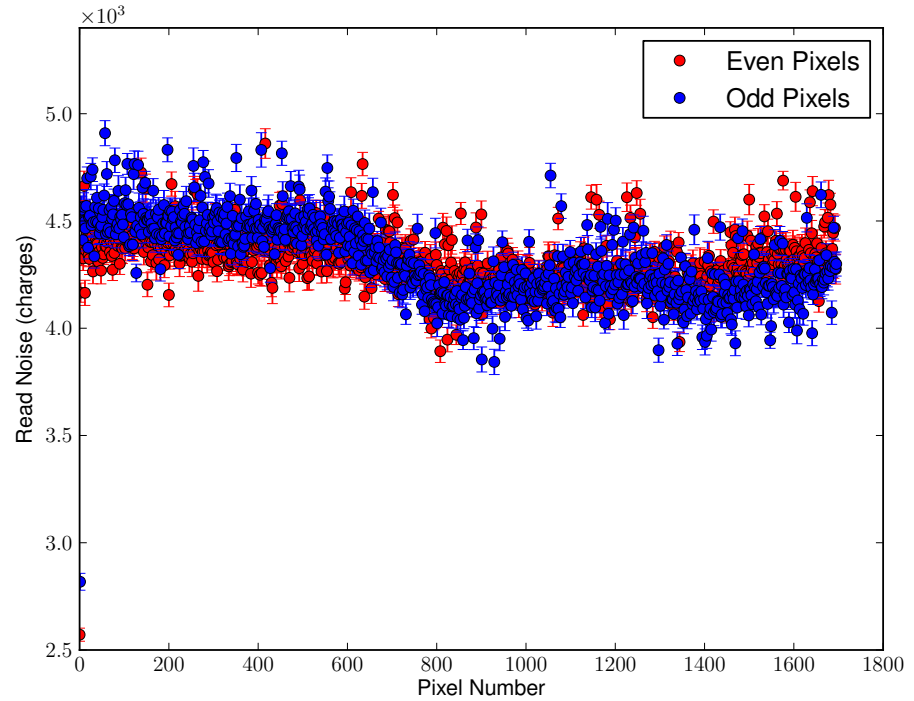


Figure 5.25: Input referred read noise vs pixel for the DM0025 in low gain. Error represent 99% confidence intervals computed from the standard deviation of 100 measurements. The output referred read noise was converted to input referred read noise using the gain determined in Section 5.1, so the shape of the plot is the same as Figure 5.22.

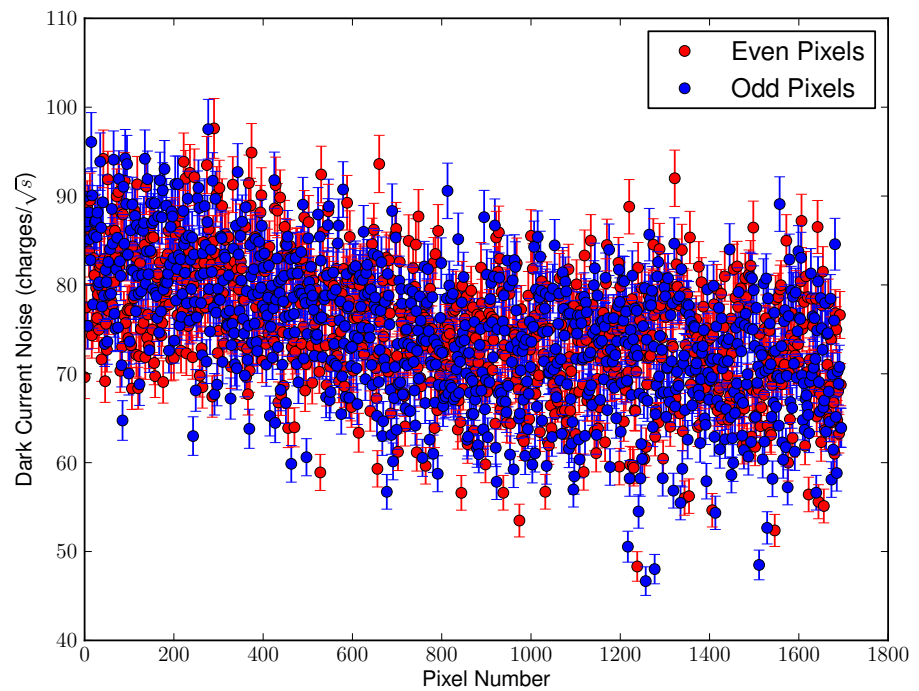


Figure 5.26: Input referred dark current noise vs pixel for the DM0025 in high gain. Error represent 99% confidence intervals computed from the standard deviation of 100 measurements.

## 5.7 Linearity of the 1696 Pixel CTIA Detector

The linearity of the DM0025 was investigated using the previously described ion gun. The linearity of the device is of particular importance for a number of reasons. Foremost is the device should be operated in its linear range for maximum reproducibility. Because post-reset noise exists, each integration starts at a slightly different output voltage offset.

### 5.7.1 Experimental Procedure

The DM0025 was mounted in the ion gun vacuum chamber as previously described in Section 5.1.2.a. The long axis of the mask on the ion gun was oriented parallel with the axis of the detector (perpendicular to the long axis of an individual electrode) to prevent ions from hitting the amplifiers themselves. Each pixel was integrated for 40 acquisitions according to the procedure described in Chapter 4.3 and 60 loops were collected for statistical averaging.

### 5.7.2 Results

A plot of the integration of the ion gun signal in high gain is shown in Figure 5.27. The large spread of slopes was due to the spatial non-uniformity of the ion gun beam. Qualitatively, it is evident that the device was reasonably linear for only part of the output range. For output voltages below about 1.5 V, the slope changes dramatically. It is interesting to note that after about 1.5 volts, the output was still

linear, but with a much lower gain. Because it is difficult to use the second region for quantification, the full scale range of the device must be restricted to the first region.

A plot of the integration of ion signal for selected pixels in low gain is shown in Figure 5.28. In contrast to Figure 5.27, the DM0025 in low gain appeared linear for a larger part of the output range. Whereas in high gain there were two different gain regions, in low gain was only one.

As discussed in Chapter 3.1.1.a, if the open-loop gain of an amplifier is sufficiently high, the closed-loop gain of an amplifier with feedback is determined only by the impedance of the feedback element. The open-loop gain is also dependent on many other factors, including the output voltage of the amplifier (66). If  $a/Z$  in Equation 3.7 is no longer much greater than 1, i.e. the ratio of open-loop gain of the amplifier  $a$  is not much greater than the feedback impedance  $Z$ , then the closed-loop gain will be dependent on the open-loop gain as well as the feedback impedance. A large feedback impedance, such as the impedance provided by the small feedback capacitor of the DM0025 CTIA array detector in high gain, will require a large open-loop gain to maintain linearity. The change in gain with the device in high gain indicates that the open-loop gain of the pre-amplifiers was not enough to keep the DM0025 linear through out its entire output voltage range in high gain. This suggests that future devices should have higher open-loop gain than the DM0025 in order to use the entire output voltage range and to increase their dynamic ranges.

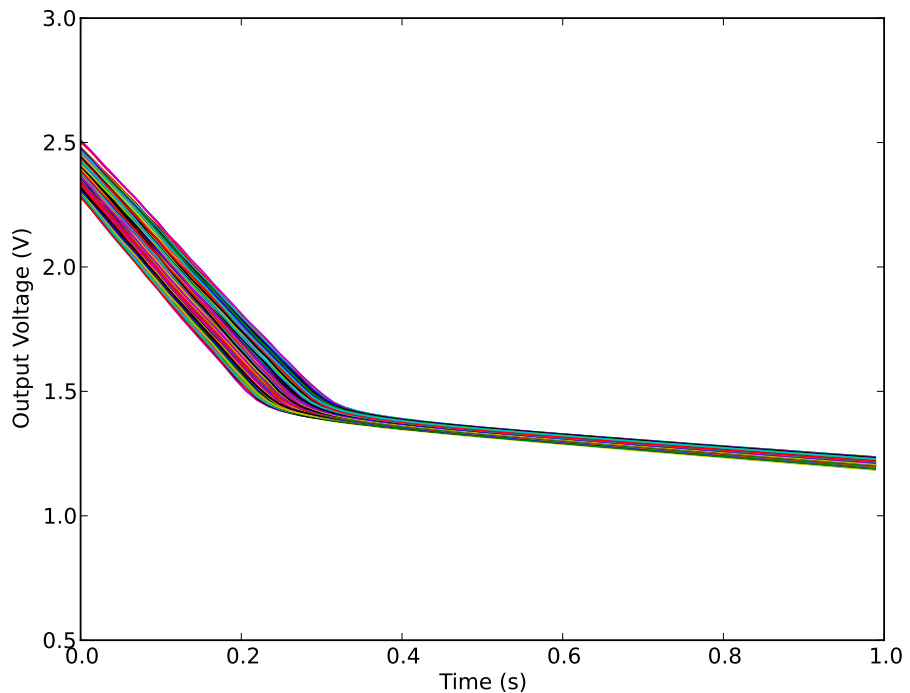


Figure 5.27: Output linearity of the DM0025 CTIA detector in high gain for selected representative pixels. The change in output slope below 1.5 V is likely due to the amplifiers of the DM0025 having insufficient open-loop gain to maintain linearity through the entire output range in high gain.

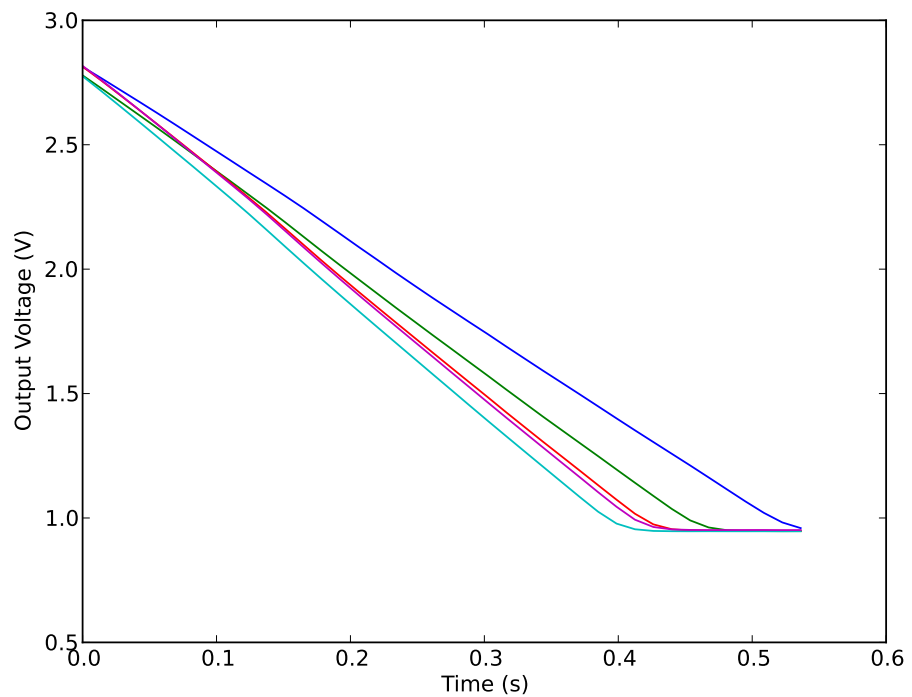


Figure 5.28: Output linearity of the DM0025 CTIA detector in low gain for selected representative pixels. In low gain, the DM0025 amplifiers have enough open-loop gain to maintain linearity through out the entire output range of the device.

One method for quantifying linearity is known as "independent linearity". In the independent linearity method, a least squares best-fit line is constructed across the full-scale range of the output, and the largest residual is used as the measure of the maximum deviation from linearity. Deviations from linearity are often expressed as a percentage of full scale range (%FSR). Because the DM0025 was not uniform across its entire output range in high gain, the first gain region was used as the full scale range. Linear fits were computed for a selection of pixels with the highest slopes when illuminated with the ion gun. These pixels were selected because the error in the measurements due to drift in ion gun beam current was minimized with short integration time. For each pixel, a linear fit was computed ending at successively longer integration times. The maximum residual for each linear fit for each pixel is plotted against the output voltage at the end of the linear fit in Figure 5.29. This plot shows that for output voltages above about 1.5 V, the maximum residual is relatively constant. Below this voltage, the maximum deviation begins to increase. By 1.4 V, the maximum deviation increases sharply, corresponding with the change in slope seen in Figure 5.27. Therefore, for maximum linearity, the lower end of the full scale range in high gain was chosen to be 1.5 V. The upper end of the full scale range was determined by the post-reset voltage for a specific pixel.

A plot of maximum residual with the device in low gain is presented in Figure 5.30. These data were produced using the same linear fitting procedure as for high gain. When the device was in low gain, the maximum residual increased at one

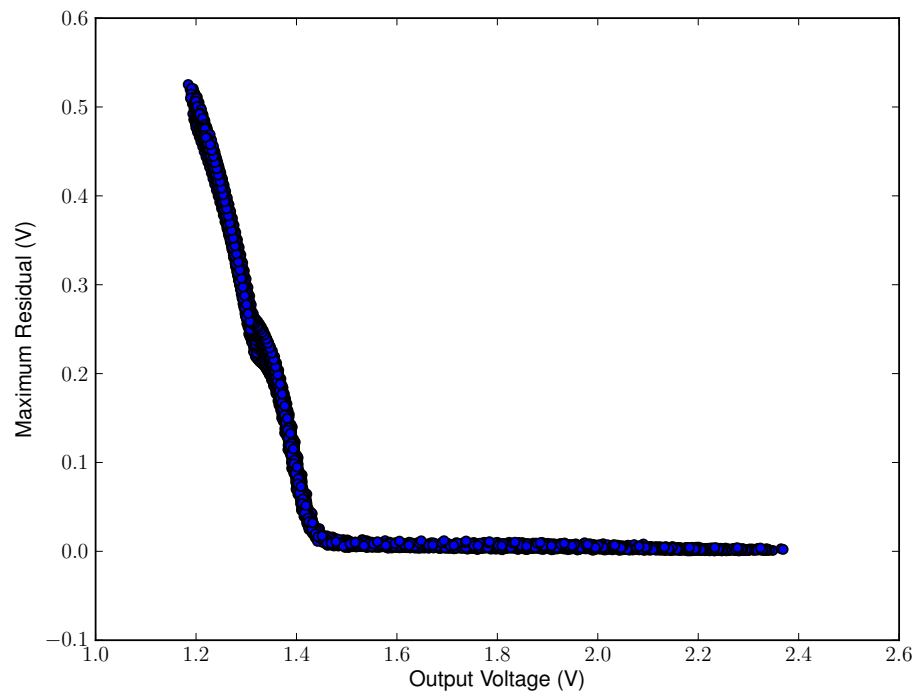


Figure 5.29: Maximum residual to determine the full scale range in high gain for the DM0025 CTIA detector. The knee in the plot determine the output voltage at which the device stops behaving linearly. For high gain the device stops behaving linearly when the output voltage is below 1.5V.

Parameter	High Gain	Low Gain
Max %FSR	$0.88 \pm 0.05$	$0.044 \pm 0.002$
Mean %FSR	$0.58 \pm 0.05$	$0.032 \pm 0.002$
Min %FSR	$0.44 \pm 0.05$	$0.024 \pm 0.002$

Table 5.2: Non-linearity for the DM0025 expressed as %FSR for high and low gain. Higher %FSR represents higher non-linearity. Errors are reported as 99% confidence intervals computed from the standard deviation of 60 measurements.

rate until about 1.0 V on the output, whereupon it began to increase rapidly. This output voltage corresponded with the minimum output voltage of the device's internal power supplies. The lower end of the full scale range in low gain was therefore set at 1.0 V.

The ion gun was noisier than the device by itself, so the maximum residues computed from the integration of the ion gun current would result in an overestimation of the %FSR non-linearity. In order to better estimate the non-linearity, the estimated variance of the output in the dark was used. Assuming the errors follow a t-distribution, for a variance computed from 40 acquisitions, 99.9% of the expected values should lie within 3.566 times the standard deviation (57), so the %FSR non-linearity in high gain was computed using:

$$\%FSR = 100 \frac{3.566 \sigma_{noise}}{\hat{\mu}_{PRV} - 1.5} \quad (5.4)$$

The minimum, maximum, and average values of the %FSR non-linearity for the DM0025 in high and low gain can be found in Table 5.2.

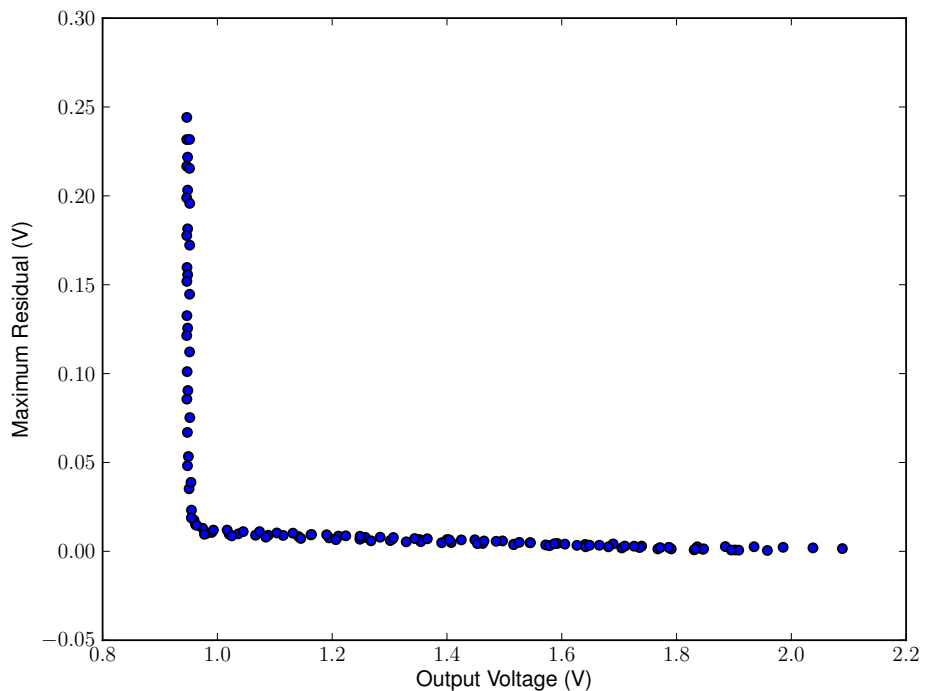


Figure 5.30: Maximum residual to determine the full scale range in low gain for the DM0025 CTIA detector. The knee in the plot determine the output voltage at which the device stops behaving linearly. For low gain the device stops behaving linearly when the output voltage is below 1.0V.

### 5.7.3 Dynamic Range and Charge Dynamic Range

A parameter related to the linearity of the device is the dynamic range. The dynamic range is the ratio of the full-scale range to the read noise. The average dynamic range for the DM0025 is  $940 \pm 150$  in high gain and  $1.5 \pm 0.3 \times 10^4$  in low gain. The error in these measurements represents the standard deviation of the dynamic ranges of all the pixels in the array. These dynamic ranges can also be expressed as a charge dynamic range, which is the ratio of the amount of charge that produces the maximum amplifier signal (known as the full well capacity) to the read noise (63). For a device with multiple gain settings it is important to examine the charge dynamic range because it is desirable for the charge dynamic ranges of the different gain settings to overlap. If the charge dynamic ranges do not overlap, there will be a dead zone between gain settings where a signal is too large to be detected with the high gain setting but too weak to be detected by the low gain setting. If, however, the dynamic ranges of the two gain settings do overlap, there is no such dead zone. This overlap region can be used for calibration purposes when monitoring samples over the entire device dynamic range. It is desirable to have some overlap, but too much overlap can result in a decrease of the overall dynamic range of the device.

A plot depicting the charge dynamic range of the DM0025 in both high gain and low gain is shown in Figure 5.31. There were about 54,000 charges of overlap between the two dynamic ranges. Because there was some overlap, the device could continuously measure signals with magnitudes from the limit of detection in high

gain all the way to the full well capacity in low gain. The full charge dynamic range of the DM0025 was therefore 6.2 orders of magnitude, calculated from the read noise in high gain and the full well charge capacity in low gain. The typical signal measured in a mass spectrometry experiment is current (charge per time), not charge. A low current signal can be integrated for a long time to accumulate the minimum detectable charge, while a high current signal can be measured for a short integration time to avoid filling the detector's full well charge capacity. Because the output voltage of a CTIA can be read out without disturbing the charge stored on the feedback capacitor (non-destructive readouts), multiple samples of the output can be measured during an integration period. Examining the limit of detection equations derived in Chapter 3.4, the current limit of detection can be extended by either measuring a larger number of samples during a fixed integration time, or by extending the integration time to acquire the desired number of samples. These factors mean that the dynamic range for detection of currents is wider than the dynamic range for charge. Schilling et al., and Felton et al., have demonstrated a dynamic range for current detection of 9 orders of magnitude - including the limit of detection - with CTIA array detectors (the 512 pixel CTIA array detector and the 1696 pixel DM0025 CTIA array detector respectively) coupled to a Mattauch-Herzog mass spectrometer (78, 79).

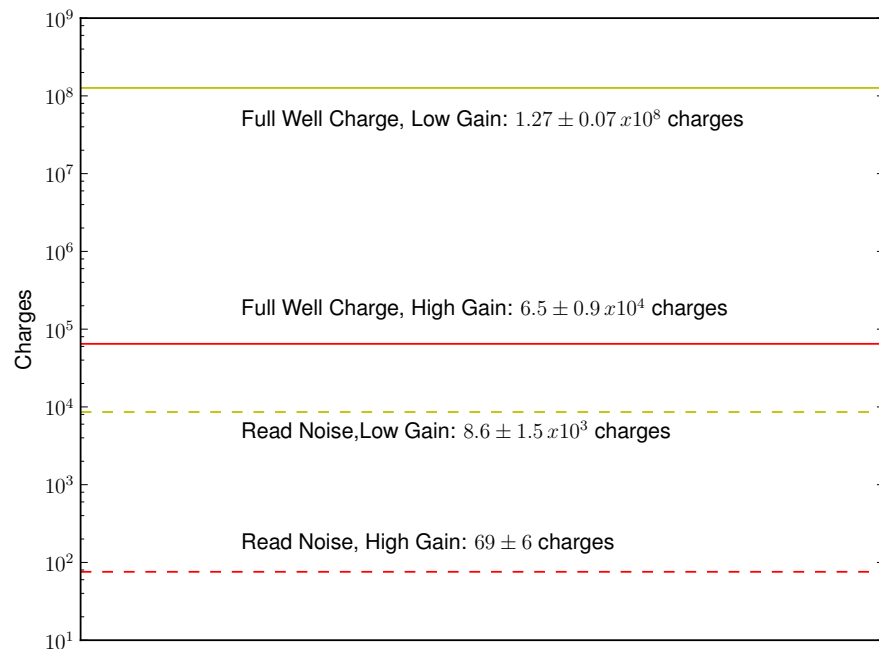


Figure 5.31: Charge dynamic range of the DM0025 CTIA array detector for both high and low gain. Errors represent the spread in values due to pixel non-uniformity. There is an overlap of the charge dynamic ranges of high and low gain, meaning there is a range of signals that can be measured in both high and low gain.

## 5.8 Predicted Limits of Detection in High Gain

The values for gain, read noise and dark current noise can be used in conjunction with the linear models developed in Chapter 3 to predict the limit of detection for the 1696 pixel CTIA array detector. The measured values of the read and dark current noises, and thus of  $\sigma_{rn}^2$  and  $\sigma_{dc}^2$ , can be used to determine the matrix  $\Sigma$  numerically (See Chapter 3.4.2.b). The variance from a generalized least squares (GLS) estimation of the slope can be computed by using:

$$\Sigma_N = \begin{bmatrix} \sigma_{rn}^2 & 0 & \cdots & 0 \\ 0 & \sigma_{rn}^2 + \sigma_{dc}^2 dt & \cdots & 0 \\ \vdots & \vdots & \ddots & \vdots \\ 0 & 0 & \cdots & \sigma_{rn}^2 + \sigma_{dc}^2 (N-1) dt \end{bmatrix} \quad (5.5)$$

The variance for a specific number of samples  $N$  was computed directly using Equation 3.69 and used to compute the limit of detection as a function of number of samples according to:

$$\hat{i}_{LOD}(N) = \frac{3\sqrt{\sigma_N^2}}{g} \quad (5.6)$$

A plot of estimated limit of detection as a function of number of acquisitions  $N$  is shown in Figure 5.32 for high gain and Figure 5.33 for low gain. For 20 acquisitions, the expected limit of detection is about 610 ions per second in high gain. The estimated limit of detection in low gain is about 73,000 ions per second, or a factor of about 120 times greater.

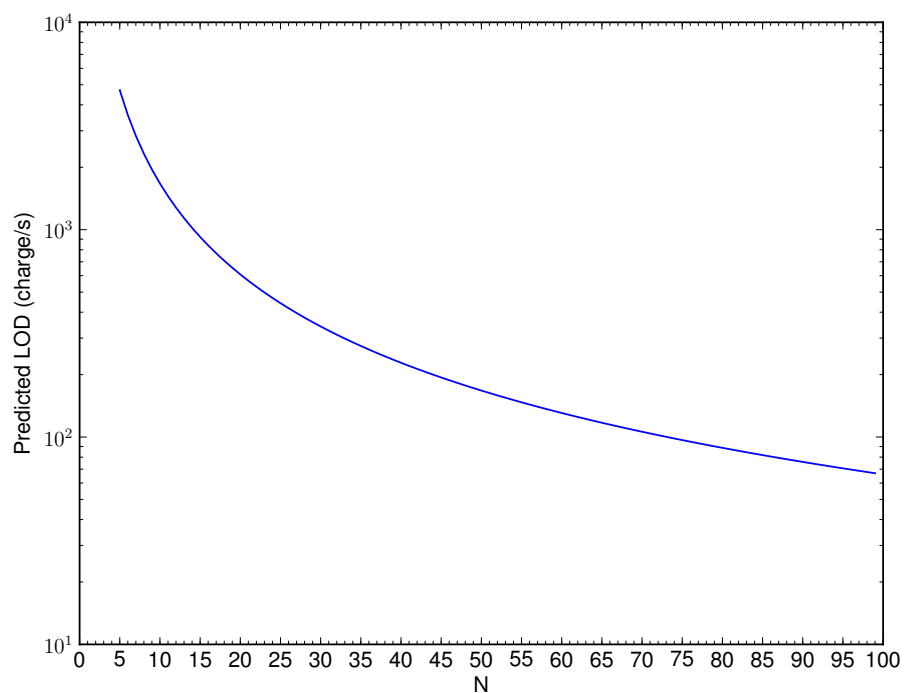


Figure 5.32: Estimation of the limits of detection of the DM0025 in high gain as a function of number of samples, computed using a GLS estimator using the read and dark-current noises measured in Section 5.6.3.

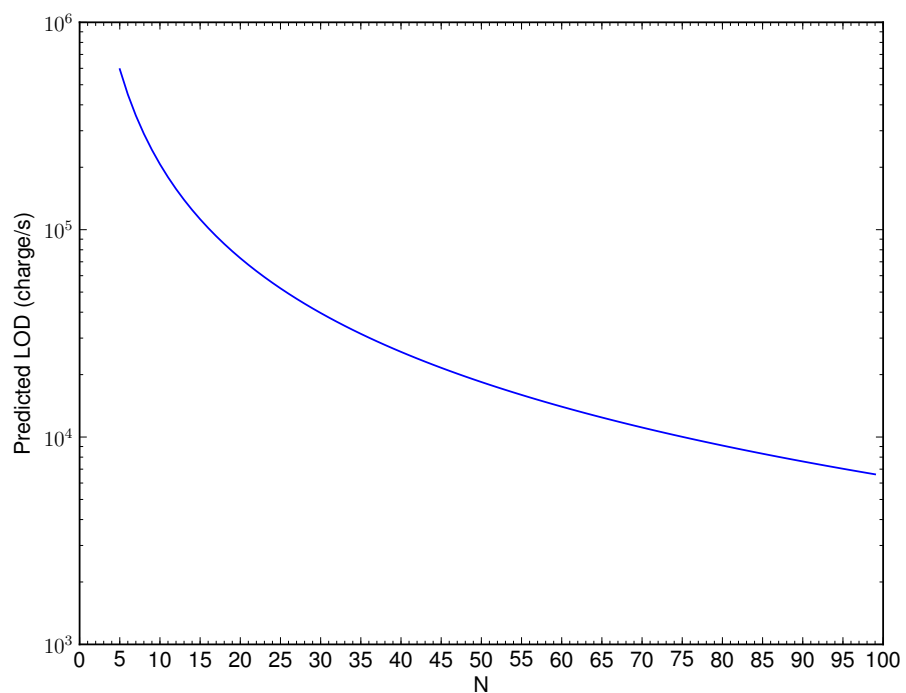


Figure 5.33: Estimation of the limits of detection of the DM0025 in low gain as a function of number of samples, computed using a GLS estimator using the read and dark-current noises measured in Section 5.6.3.

## 5.9 Conclusions

A detailed characterization of the DM0025 1696 pixel CTIA array detector was presented. Some of the more important results from this detailed characterization were used to predict limits of detection for the detector. The results of this characterization can be used in conjunction with the linear models derived in Chapter 3 to determine what improvements need to be made to the next generation of CTIA array detectors, in order to progress toward the goal of single ion detection. The two parameters that affect the limit of detection the most are the read noise and the dark current noise. From the models derived in Chapter 3, the read noise has more influence on the limit of detection for short integration times, while the dark current noise has more of an influence on the limit of detection for long integration times. It is therefore desirable to reduce both noises in order to increase detection limit for a wide range of integration times.

The combined dynamic range of the DM0025 array detector could be improved by increasing the open-loop gain of the pre-amplifiers so high gain has the same full scale range as low gain. This by itself would not increase the combined dynamic range of the device because the upper end of the combined dynamic range depends on the full well charge capacity in low gain. Increasing the full-scale range in high gain coupled with a decrease in the voltage-to-charge gain in low gain would increase the combined dynamic range of the device. The dynamic range of a particular gain more (high or low gain) depends on the ratio of the read noise to the full scale

range. How much the high gain and low gain dynamic ranges overlap depends on the gain factor between high and low gain. If the full well capacity in high gain were increased by raising the full scale range in high gain, the gain factor difference between high and low gain could be increased by raising the value of the low gain capacitor (thereby decreasing the voltage per charge gain in low gain) to maintain some overlap between the two dynamic ranges. A decrease in the voltage-to-charge gain in low gain would increase the full well charge capacity in low gain, thus increasing the detector's combined dynamic range.

Another way to increase the dynamic range of the device would be to switch to a different manufacturing process. The present devices are manufactured using a 3.3 V process, which limits the output voltage to a range of 0 to 3.3 V. There are other, higher voltage processes, including 9 V processes, that would allow the fabrication of devices with higher output voltages. The noise performance of devices fabricated with a different process might be different from the present devices manufactured with a 3.3V process, so detailed a detailed characterization like that presented here must be performed on any new devices.

Parameter	High Gain	Low Gain
Gain	$-15 \pm 1 \text{ } \mu\text{V}/e^-$	$-10.1 \pm 0.3 \text{ nV}/e^-$
Dark Current at 228K		-0.08 to 0.1 fA
Output Read Noise at 228K	$1.0 \pm 0.1 \text{ mV}$	$87 \pm 15 \text{ } \mu\text{V}$
Output Dark Current Noise at 228K	$1.1 \pm 0.4 \text{ mV}$	not measurable
Input Read Noise ( $e^-$ ) at 228K	$69 \pm 6$	$8600 \pm 1500$
Input Dark Current Noise( $e^-$ ) at 228K	$75 \pm 22$	not measurable
FSR (V)	$0.94 \pm 0.12$	$1.28 \pm 0.07$
Linearity (%FSR)	$0.58 \pm 0.22$	$0.032 \pm 0.010$
Dynamic Range (orders of magnitude)	$2.9 \pm 0.1$	$4.2 \pm 0.2$
Combined Dynamic Range		6.2

Table 5.3: Summary of characterized detector parameters. Errors represent spread of measured parameters across the array

## CHAPTER 6

EVALUATION OF THE 1696 PIXEL ARRAY DETECTOR FOR MASS  
SPECTROMETRY

This chapter presents the results of the combination of the DM0025 1696 pixel CTIA array detector characterized in Chapter 5 with a linear cycloid mass spectrometer produced by Monitor Instruments. The linear cycloid has some properties that make it challenging to use with electron multiplier (EM) as well as micro-channel plate (MCP) ion detectors, but not with CTIA array detectors. In addition, the mass dispersive properties of the linear cycloid make it an ideal instrument to take advantage of simultaneous detection using an array detector. The first linear cycloid was reported by Bleakney and Hipple in 1938, but the instrument never achieved widespread use (44). A brief introduction to the theory of linear cycloid instruments is presented first. Because a significant portion of the work that lead to the results reported in this dissertation involved the design and construction of the components necessary to successfully combine the DM0025 CTIA array detector with the Monitor Instruments linear cycloid, a brief description of these components as well as of the combined instrument are then presented. The performance of the combined instrument was greatly influenced by some of the choices made during its construction. Finally, the results from evaluation of the combined instrument

are presented. The ability of the combined instrument to measure multiple masses simultaneously was influenced by the way in which the detector was adapted to the instrument. The quantitative performance of the combined instrument was evaluated through measured limits of detection. These limits of detection were greater than those predicted in Chapter 5, due to noise produced by the support electronics supplied with the cycloid instrument. The results from this performance evaluation lead to a number of ideas for improving the next generation of combined instrument, discussed in Chapter 7.

## 6.1 Adapting the 1696 Pixel CTIA Array Detector to the Monitor Instruments Cycloidal MS

To adapt the 1696 detector to cycloidal MS, a custom detector assembly had to be constructed, shown in Figure 6.1. The core of this assembly was a custom machined copper block to which the detector die was epoxied. Surrounding the detector was the detector daughter board, which had the bypass capacitors for the various power lines going to the detector, as well as the output buffer amplifiers. There were also pads for all the digital control lines needed to control the detector. This daughter board attached to the copper block with screws as well as epoxy, for stability. The pads on the detector die were wire-bonded directly to pads on the daughter board. Wires from this daughter board connected to the main detector support board, mounted on the opposite end of the copper block from the detector. The main

detector support board was mounted to a custom machined heat sink with a built-in water reservoir. A thermoelectric heat-pump was mounted between the copper block and this heat sink to cool the detector. The heat sink also provided heat dissipation for the main detector support board, which generated several watts of excess heat. A pair of custom machined brackets were attached to the top of the heat sink to mount and position the entire detector assembly on a support structure around the cycloidal MS.

The Monitor Instruments linear cycloid mass spectrometer was supplied mounted on a 4.5" CF vacuum flange that included several vacuum feedthroughs for the mass spectrometer control voltages and the sample inlet capillary. There was not enough room on this supplied flange to accommodate the 81 signal and power lines as well as water for cooling the hot side of the thermoelectric cooler required by the CTIA detector. Therefore, a custom NW200 vacuum flange was designed and constructed with electrical, as well as fluid feedthroughs, to which the linear cycloid's original flange was attached. This custom flange was part of a custom vacuum chamber built in the Denton laboratory. The entire detector assembly was positioned on the Monitor Instruments linear cycloid mass spectrometer using a support structure made from aluminum that was attached to this custom vacuum flange. The instrument, mounted to the vacuum flange, as viewed from above, is shown in Figure 6.2. The detector, as well as the magnet, were removed for this picture. In normal operation, the magnet sits on the solid aluminum plate underneath the instrument. The

brackets on the detector assembly rest on the four brass screws, which allow the detector assembly to be raised and lowered with respect to the magnet/electric sector assembly. The focal plane of the linear cycloid was in the center of the instrument, so Monitor Instruments cut a hole in the center support (the ground plane) to allow better access to the focal plane. This hole can be seen in the middle of Figure 6.2. The combined instrument and detector assembly can be seen in Figure 6.3.

This assembly arrangement resulted in some problems with the combined instrument. First of all, it was difficult to see the detector surface because it was buried inside the magnet gap. This made it difficult to position the detector on the focal plane. The ramifications of positioning the detector outside of the focal plane are discussed in greater detail below. In addition, because the magnet was inside the vacuum chamber, adjusting the position of the magnet to improve instrument resolution was time consuming, as it required breaking vacuum, manually adjusting the magnet position, and re-pumping the system before the effects of the adjustment could be evaluated. In addition, the presence of the magnet inside the vacuum chamber meant that the vacuum chamber could not be baked out for fear of damaging the magnet, resulting in long pump-down times to reach operating pressure.

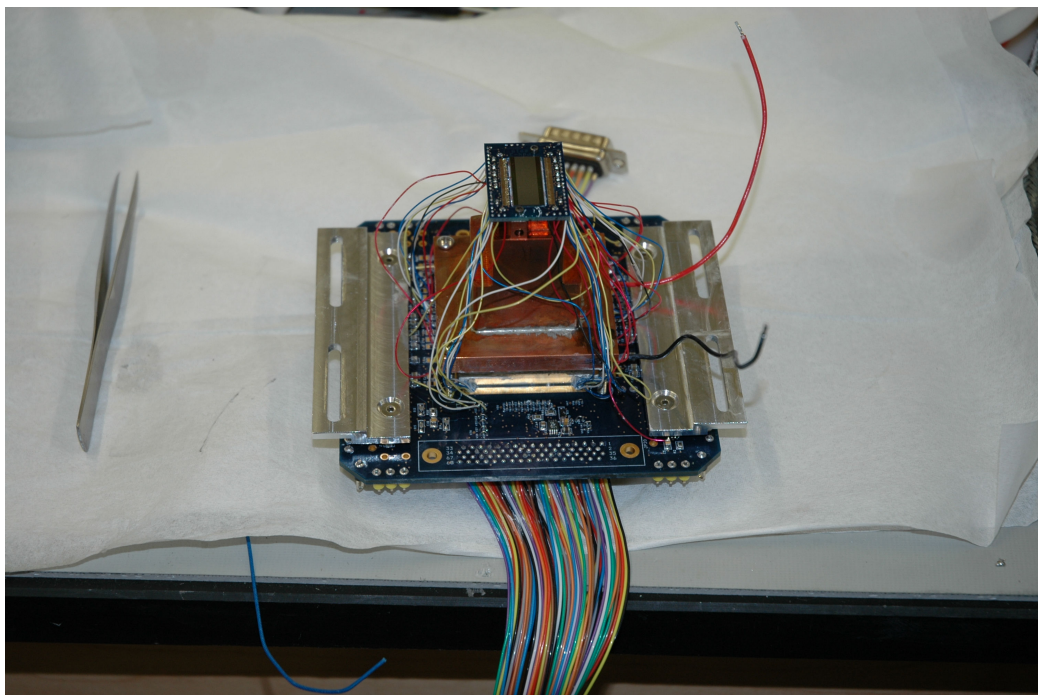


Figure 6.1: Detector mounted on the copper finger with the thermoelectric cooler and support board.

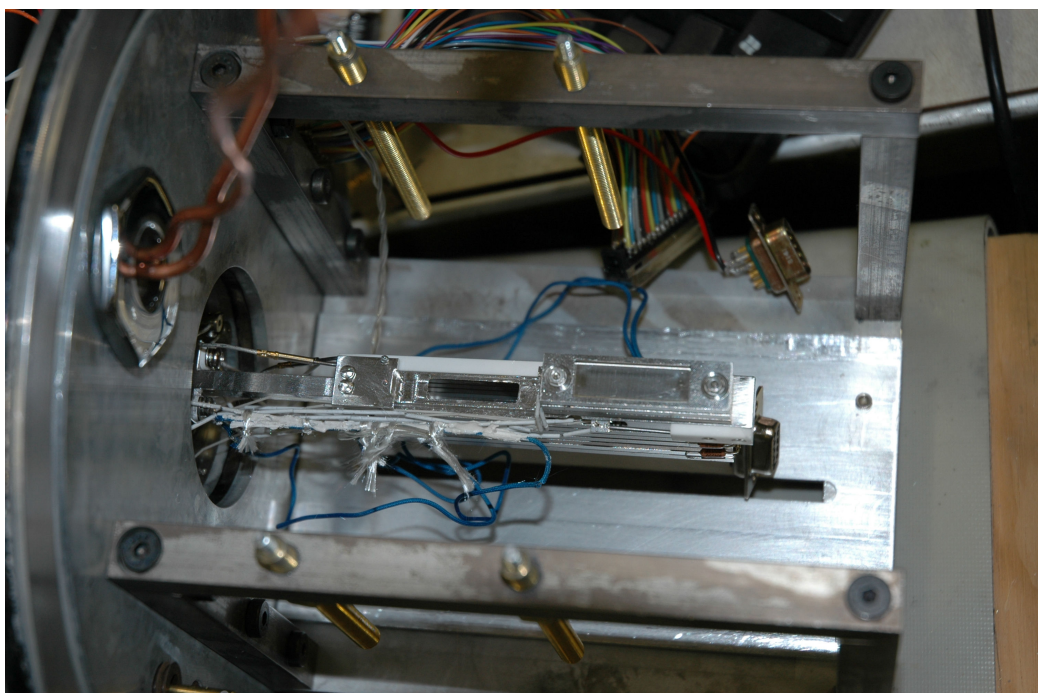


Figure 6.2: Closeup of the Monitor Instruments linear cycloid mounted on the vacuum flange, viewed from above. The support structure for the detector and the custom hole for the CTIA detector are visible.

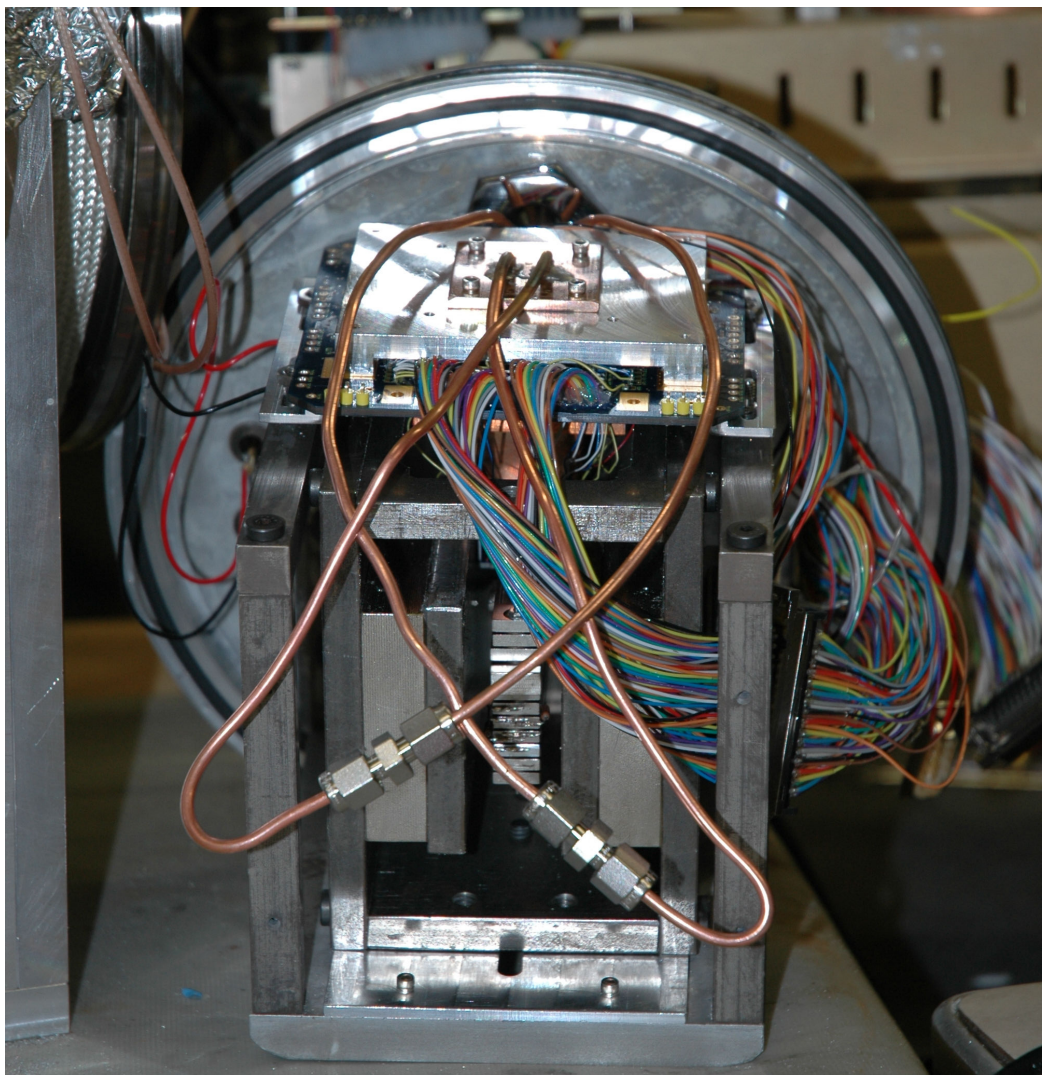


Figure 6.3: Detector mounted on the linear cycloid. The heat sink and motherboard are visible on top. The detector itself is hidden inside the instrument.

## 6.2 Performance of the Array Detector/Cycloidal MS System

### 6.2.1 Instrument Control and Procedure

Due to the size of the DM0025 CTIA array detector, as well as the instrument geometry, and electric and magnetic fields, the entire instrument mass range (1-200 amu) could not be focused simultaneously on the detector. Instead, the detector was used to sample a small mass window, the size of which and center mass depended on the electric field used. The electric field was controlled by adjusting a control voltage on the instrument's high voltage power supply, referred to as the "mass control" voltage. The multi-pixel control program described in Chapter 4.3 was modified to control the linear cycloid mass spectrometer by adjusting the mass control voltage. For all experiments described in this chapter, the instrument was set to a specific mass control voltage before data were acquired, ensuring that the ions experienced a static electric field. The Monitor Instruments linear cycloid used an electron impact source. The filament current and the electron energy were controlled by electronics supplied by Monitor Instruments. This hardware was in turn controlled by a supplied control computer program that interfaced with the instrument through a serial port. The Monitor Instruments control computer program was not modified for any of the work presented here. The default value of 70 eV was used for electron energy in all experiments.

### 6.2.2 Maximum Number of Samples

There were limitations to the number of samples that could be acquired due to limitations in the data acquisition system. The software used to control the analog to digital converter and the detector - National Instruments LabView - can only acquire a certain number of samples before running out of memory. Experiments conducted in this chapter were repeated multiple times during the same acquisition loop in order to compute statistical averages and standard deviations. This, combined with the large size of the array, places a practical limit on the number of samples that could be acquired.

The typical use for a CTIA detector in mass spectrometry is as a current detector. Because the output of the CTIA is the integral of the input current, the output signal must be differentiated to determine the input current. Here that differentiation was accomplished through ordinary least squares (OLS) slope estimation. From the results in Chapter 3, it is desirable to acquire as many samples as possible, to reduce the variance of the estimated slope. Ordinary least squares estimation assumes the errors have a constant variance (Chapter 2.3.1), while, as explained in Chapter 3.1.2, the CTIA has a time dependent variance. Because of this, the best linear unbiased estimator to estimate the slope is the generalized least squares (GLS) estimator, not the OLS estimator (Chapter 2.3). For a set of output data, the GLS estimator relies on the true variance as a function of time for that data, which is in general unknown, while the OLS estimator can be readily computed directly from the data.

Even if the OLS assumption of uniform error variance were invalid, the OLS slope estimator would still provide an unbiased estimate of the slope, just not the most efficient (lowest variance) estimation. An integration period of 20 acquisitions at 72 Hz corresponded to an average increase in variance, from points at the beginning to the end of integration, of about 15%. The maximum number of samples was thus chosen to be 20 as a compromise between maximizing the number of samples and preserving the assumption of constant error variance for the OLS slope estimator.

### 6.2.3 Array Detection on a Linear Cycloid

#### 6.2.3.a Experimental Procedure

The performance of the detection of multiple mass peaks with the CTIA array detector and the linear cycloid was evaluated using a mixture of ambient air and carbon dioxide. The inlet capillary was placed in a glass vial through a septum. Carbon dioxide vapor from evaporating dry ice was sampled using a Hamilton GasTight syringe and injected into the vial. Forty non-destructive readouts were collected using the program described in Section 6.2.1

#### 6.2.3.b Results

The mass spectrum of ambient air mixed with  $CO_2$  measured in low gain is shown in Figures 6.4 and 6.5. Figure 6.4 shows the ion current plotted as a function of detector pixel, while Figure 6.5 shows the same ion current plotted as a function of

mass. Comparing the two figures, the linear mass dispersion of the linear cycloid can be seen. For this mass range, the mass dispersion was about 73 pixels per mass unit, which corresponded to a little over 900  $\mu\text{m}$  per mass unit. The peaks from dinitrogen-14 and dioxygen-16 are off scale in the plot to better show the lower intensity mass peaks, but neither of these two peaks (dinitrogen-14 and dioxygen-16) were intense enough to fill the full well charge capacity during the integration time.

Several features of the mass spectrum are notable. First, the resolution is not as good as expected based on either the theoretical performance of the instrument or experiments conducted by Monitor Instruments. The expected baseline peak width was about 8 pixels, or about 100  $\mu\text{m}$ . These peaks are all over 50 pixels wide at the base, some over 200 pixels, which is equivalent to about 2.5 mm. There are several reasons for this degradation in resolution. First, because of mechanical and physical constraints, the detector could not be placed directly on the instrument focal plane, and was instead located behind the focal plane, as depicted in Figure 6.6. Ions are focused as they pass through the focal plane but then begin to defocus, so their spread was wider once they reached the detector. In addition, as ions come into focus, they begin to experience a repulsive force from other ions due to space charge, which exacerbates the decrease in resolution behind the focal plane. Because the Monitor Instruments linear cycloid was originally designed for a single channel detector, the range of ion paths that pass through uniform magnetic and electric

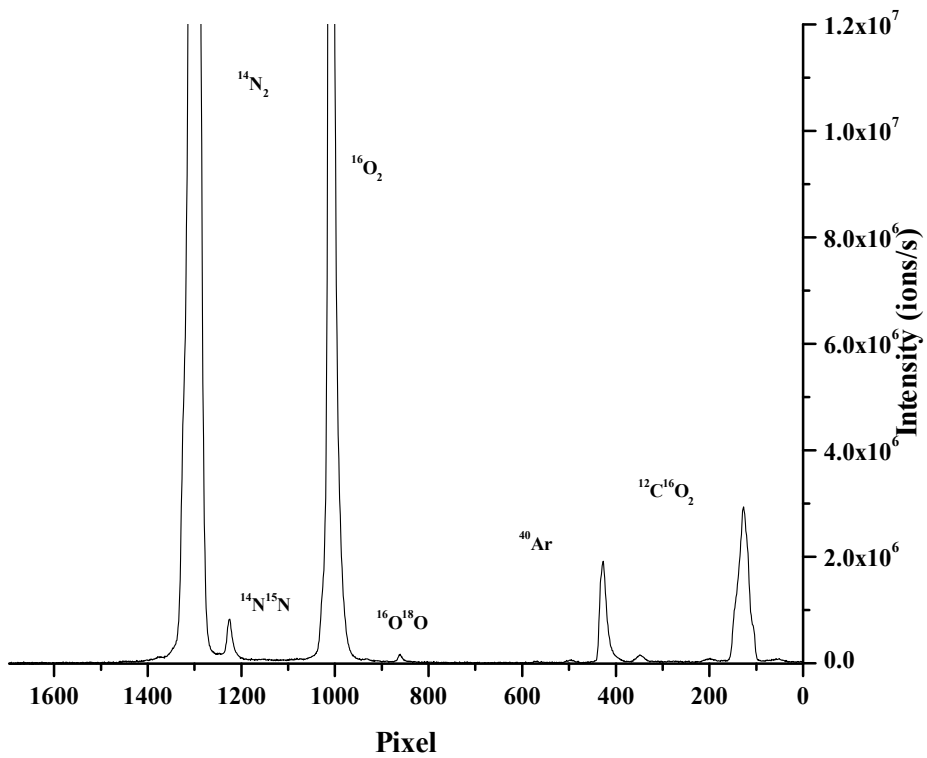


Figure 6.4: Mass spectrum of air with added  $\text{CO}_2$ . The signal is the slope of 40 non-destructive readouts of the output of the detector. The mass dispersion is linear, with approximately 73 pixels per mass unit.

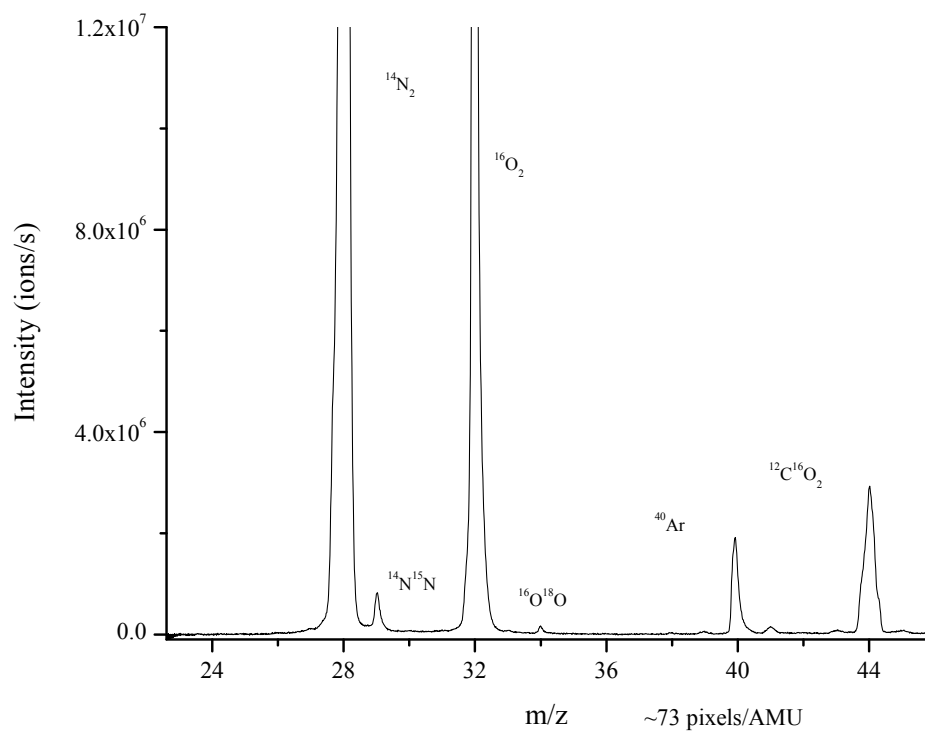


Figure 6.5: Mass spectrum of air with added  $\text{CO}_2$ . The signal is the slope of 40 non-destructive readouts of the output of the detector. Peak broadening from space charge effects as well as peak distortion from fringing fields in the instrument are visible.

fields is small. Fringing fields due to the plates that produce the electric field, as well as inhomogeneities in the magnetic field toward the edges of the magnet, meant that many ion trajectories were not focused according to Equation 1.10. This resulted in a degradation of resolution for all peaks in the spectrum, as well as peak distortion that can be seen for the argon and carbon dioxide peaks in Figures 6.4 and 6.5. This behavior has been observed for previously constructed linear cycloids as well (80, 81)

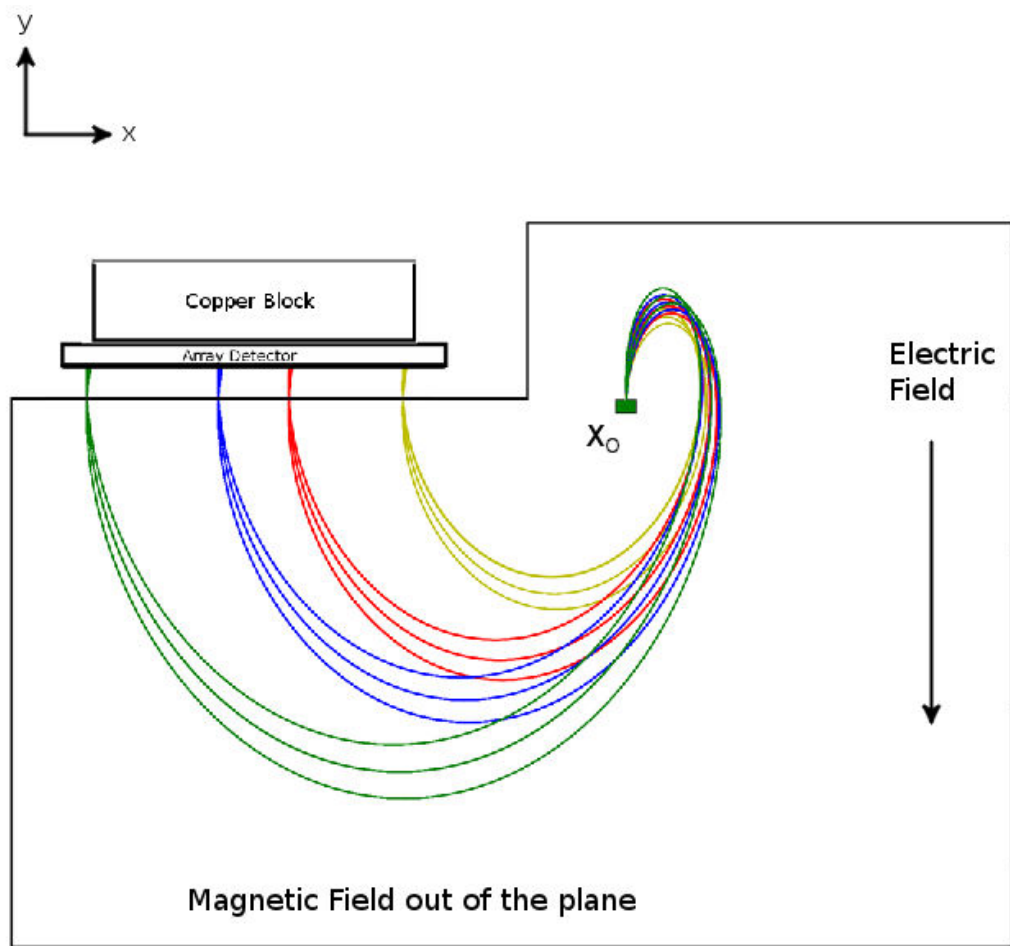


Figure 6.6: Effect of positioning the array detector behind the focal plane. The ion source is located at  $x_0$ . Resolution is degraded due to defocusing of the ion beam after it passes through the focal plane.

#### 6.2.4 Limits of Detection

The response of the mass spectrometer with the CTIA detector was characterized using perfluoro(methylcyclohexane) ( $C_7F_{14}$ ). This compound was chosen because its most abundant fragment, at  $m/z = 69$ , was well removed from any peaks due to ambient air. The vapor pressure of perfluoro(methylcyclohexane) is very high, so the compound passed through the instrument quickly and did not remain on any of the sample preparation glassware, reducing the influence of previously measured concentrations.

##### 6.2.4.a Experimental Procedure

Samples for the response studies were prepared using volumetric dilution. Volumes of liquid perfluoro(methylcyclohexane) were added using a Hamilton GasTight syringe to a glass bottle sealed with a septum. The volume of the glass bottle was  $311 \pm 1$  mL. Ten minutes were allowed to elapse to allow the perfluoro(methylcyclohexane) to fully evaporate. Volumes of perfluoro(methylcyclohexane) gas were then extracted from the glass bottle and added to a septum-capped vial using a different Hamilton GasTight syringe. The mass spectrometer's inlet capillary was inserted through the septum into the vial. The volume of the septum vial was  $5.6 \pm 0.2$  mL. Four minutes were allowed to elapse before the data were recorded. The data were collected using the program described in Section 6.2.1. Thirty repetitions of 20 non-destructive readout acquisitions were recorded. The concentrations of perflu-

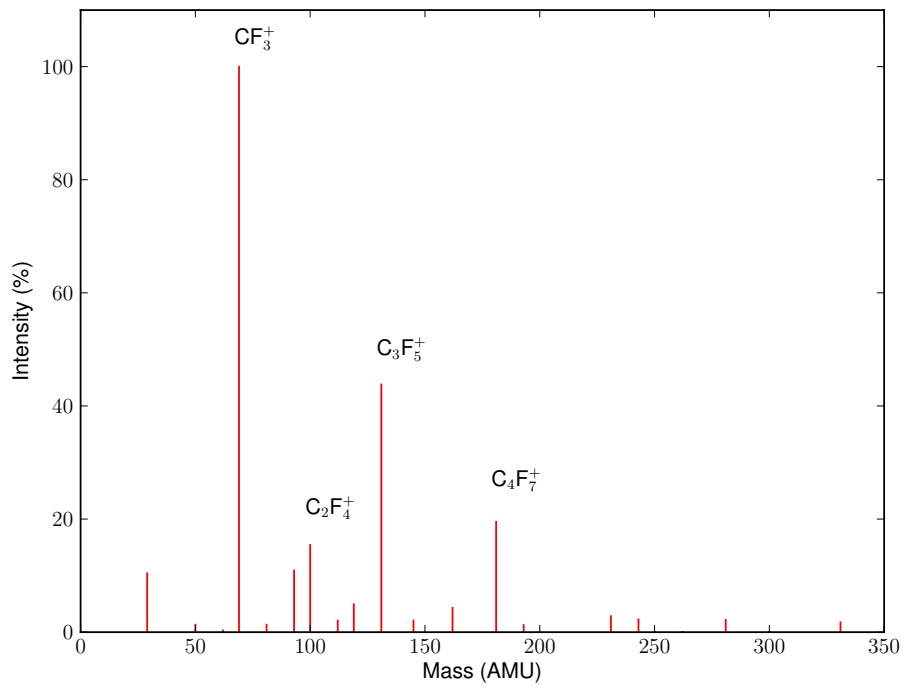
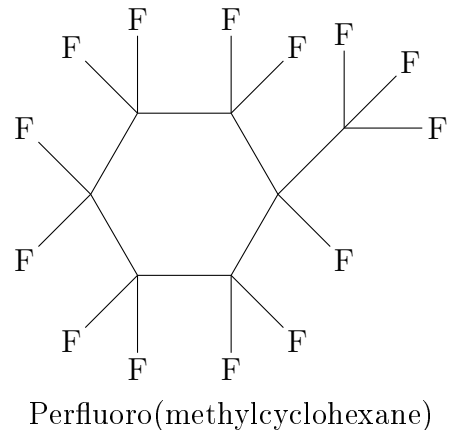


Figure 6.7: Mass spectrum of perfluoro(methylcyclohexane) with electron impact ionization and an ionization energy of 70 eV. Intensities referenced to  $\text{CF}_3^+$  ion (intensity of  $\text{CF}_3^+ = 100 \%$ ). Intensity data taken from Dibeler et al. (82).

Volume of liquid: $1.0 \pm 0.1\mu L$		
Volume of Vapor ( $\mu L$ )	Concentration ( $mol/L$ )	Concentration error ( $\pm mol/L$ )
10	$3.0e - 8$	$3e - 9$
20	$5.9e - 8$	$6e - 9$
30	$8.9e - 8$	$1e - 8$
40	$1.2e - 7$	$1e - 8$
50	$1.5e - 7$	$2e - 8$
60	$1.8e - 7$	$2e - 8$
70	$2.1e - 7$	$2e - 8$
80	$2.4e - 7$	$3e - 8$
90	$2.7e - 7$	$3e - 8$
100	$3.0e - 7$	$3e - 8$

Table 6.1: Concentrations of perfluoro(methylcyclohexane) used for high gain with errors.

oro(methylcyclohexane) used in the limits of detection study are shown in Tables 6.1 and 6.2. The slope of the output voltage of the pixel at the maximum of the most abundant peak,  $CF_3^+$  at  $m/z = 69$ , was measured for all experiments. With the mass control voltage set to center this peak on the array, no other mass peaks were visible, and since the mass spectra used for the limits of detection are just single peaks, they are not shown. The response was the slope of the signal measured at the pixel at the peak maximum.

Volume of liquid: $10.0 \pm 0.1\mu L$		
Volume of Vapor ( $\mu L$ )	Concentration ( $mol/L$ )	Concentration error ( $\pm mol/L$ )
10	$3.0e - 7$	$2e - 8$
20	$5.9e - 7$	$3e - 8$
30	$8.9e - 7$	$4e - 8$
40	$1.18e - 6$	$5e - 8$
50	$1.48e - 6$	$6e - 8$
60	$1.77e - 6$	$7e - 8$
70	$2.07e - 6$	$8e - 8$
80	$2.36e - 6$	$9e - 8$
90	$2.7e - 6$	$1e - 7$
100	$3.0e - 6$	$1e - 7$

Table 6.2: Concentrations of perfluoro(methylcyclohexane) used for low gain with errors.

#### 6.2.4.b Method Validation

To validate the methodology used to determine the limits of detection and linear dynamic range, a sample of perfluoro(methylcyclohexane) was prepared as described above, injecting  $1\mu L$  into the glass bottle, and  $100\mu L$  of gas from the glass bottle into the septum vial. Figure 6.8 shows the amplitude of the  $CF_3^+$  peak in the perfluoro(methylcyclohexane) spectrum as a function of time. Time zero was just after the volume was injected into the septum vial. It took a few dozen seconds for the perfluoro(methylcyclohexane) to travel down the capillary tube. There was initially a rapid rise in signal followed by an exponential decay over a few minutes to a steady signal value with superimposed noise. This initial decay was attributed to incomplete mixing of the perfluoro(methylcyclohexane) vapor during the first two minutes after it was injected into the septum vial. This conclusion was supported by

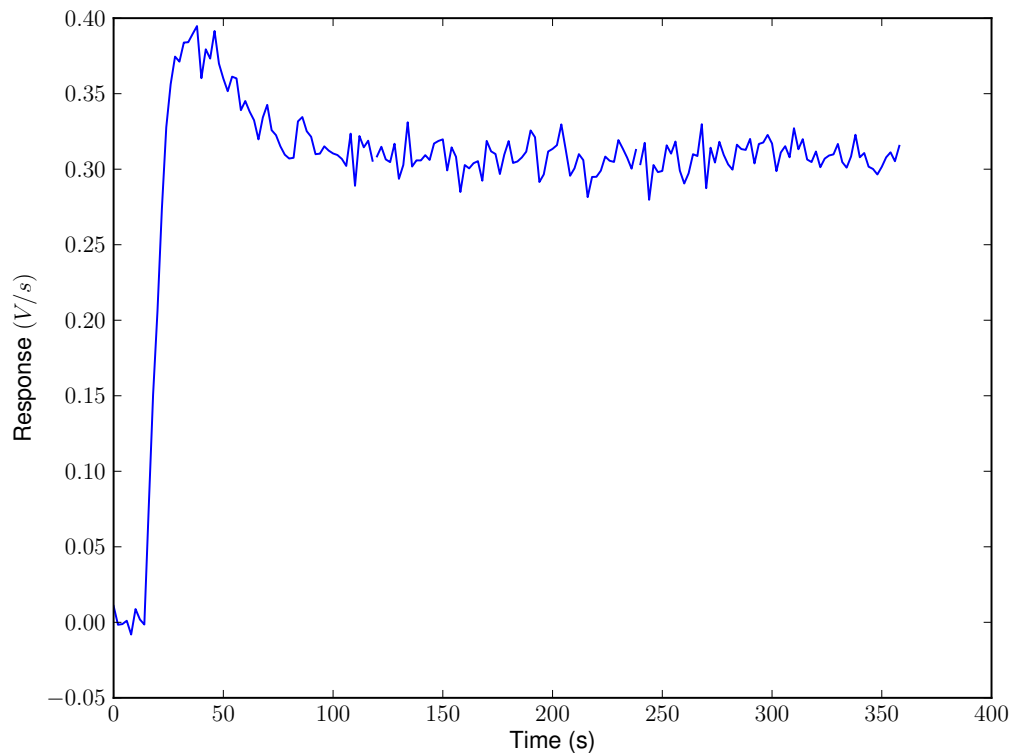


Figure 6.8: Instrument response as a function of time from a  $3.0e-6$  mol/L sample of perfluoro(methylcyclohexane). The response peaks early due to incomplete mixing of the sample in the sample introduction vial, then levels off. Limit of detection data were collected 4 min after injection of each sample to ensure a stable response.

a further experiment, where the vapor was injected into the septum vial while the inlet capillary was not inserted into the vial. Four minutes later the inlet capillary was inserted through the septum. The signal measured during this experiment (data not shown) was constant except for noise.

Increasing volumes of perfluoro(methylcyclohexane) vapor were withdrawn from the same prepared sample in the glass bottle, potentially leading to a decrease in concentration in the glass bottle, but, the total amount of sample withdrawn was small, resulting in an insignificant change in concentration in the glass bottle. The error in volume from the syringe was larger than the error from taking samples from the same bottle, so no precision would have been gained by making a fresh bottle sample for each concentration.

#### 6.2.4.c Limits of Detection

Plots of the response of combined instrument from the introduction of samples of perfluoro(methylcyclohexane) with concentrations near the limits of detection for both high gain and low gain are shown in Figures 6.9 and 6.10. The limits of detection in high and low gain computed from these plots, along with the theoretical detection limits computed in Chapter 5.8, are given in Table 6.3. For high gain, the limit of detection was extrapolated from the data, because a sample with a concentration at the limit of detection could not be reproducibly prepared. For low gain, the limit of detection was interpolated from the plot. The measured limit

of detection was estimated for a single integration period, but data from multiple integration periods were averaged to produce the results. Since the data points on both plots were obtained from an average of 30 integrations, concentrations lower than the detection limit for a single integration were measurable in low gain.

The detection limit in low gain is 89 times higher than in high gain, which is less than the expected factor of 120 (Chapter 5.8). The measured detection limit in high gain is higher than the predicted detection, while the measured detection limit in low gain is approximately what was predicted. The detector face and the ground plate of the mass spectrometer act like a capacitor on the input of the detector. Noise voltages on the ground plate can capacitively couple into the detector, resulting in additional noise on the output. Other plates in the mass spectrometer can also act as one end of a capacitor, and in the same way couple noise into the detector. The detector gain in low gain was not great enough to amplify these noises to levels comparable to the noise from the sample and hold stage, output buffers, and ADC, so the output noise in low gain with the mass spectrometer on was the same as the output noise of the detector by itself. In high gain, however, the gain was large enough to amplify input noises significantly compared to the noise from the sample and hold stage, output buffers, and ADC, so additional noise on the input from the mass spectrometer electronics contributed significantly to the output noise of the detector in the combined instrument. Because the output noise in high gain is higher in the presence of the mass spectrometer, the limit of detection in high gain

is higher than predicted from the noise from the detector alone.

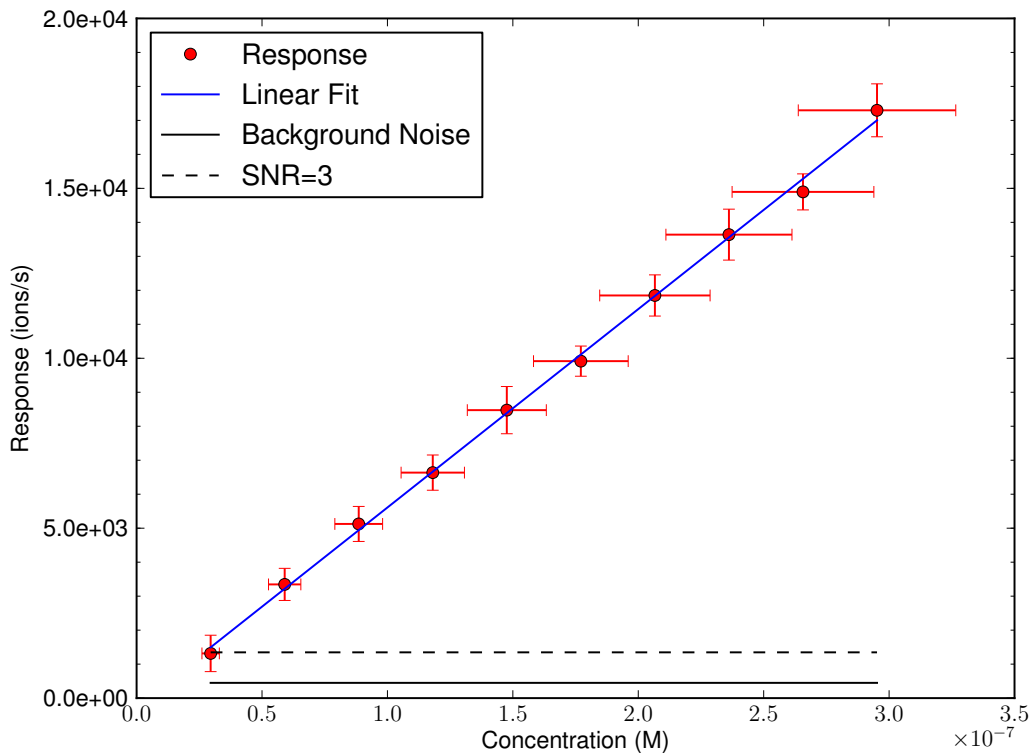


Figure 6.9: Instrument response as a function of concentration in high gain. Vertical error bars are 99% confidence intervals computed from the standard deviation of 30 measurements. Horizontal error bars are the propagated uncertainties from sample preparation. The limit of detection is extrapolated to be  $1.8 \pm 0.7 \times 10^{-8}$  mol/L, which corresponds to  $8.3 \pm 0.9 \times 10^2$  ions/s at the detector. Due to sample preparation difficulties, the limit of detection was not directly measurable. The limit of detection is higher than predicted due to noise from the instrument.

Parameter	High Gain	Low Gain
Measured LOD (mol/L)	$1.8 \pm 0.7 \times 10^{-8}$	$1.5 \pm 0.1 \times 10^{-6}$
Measured LOD (ions/s)	$8.3 \pm 0.9 \times 10^2$	$7.21 \pm 0.04 \times 10^4$
Theoretical LOD (ions/s)	$6.1 \times 10^2$	$7.3 \times 10^4$

Table 6.3: Measured limits of detection for perfluoro(methylcyclohexane) in high and low gain compared to the predicted limits of detection from Chapter 5.8.

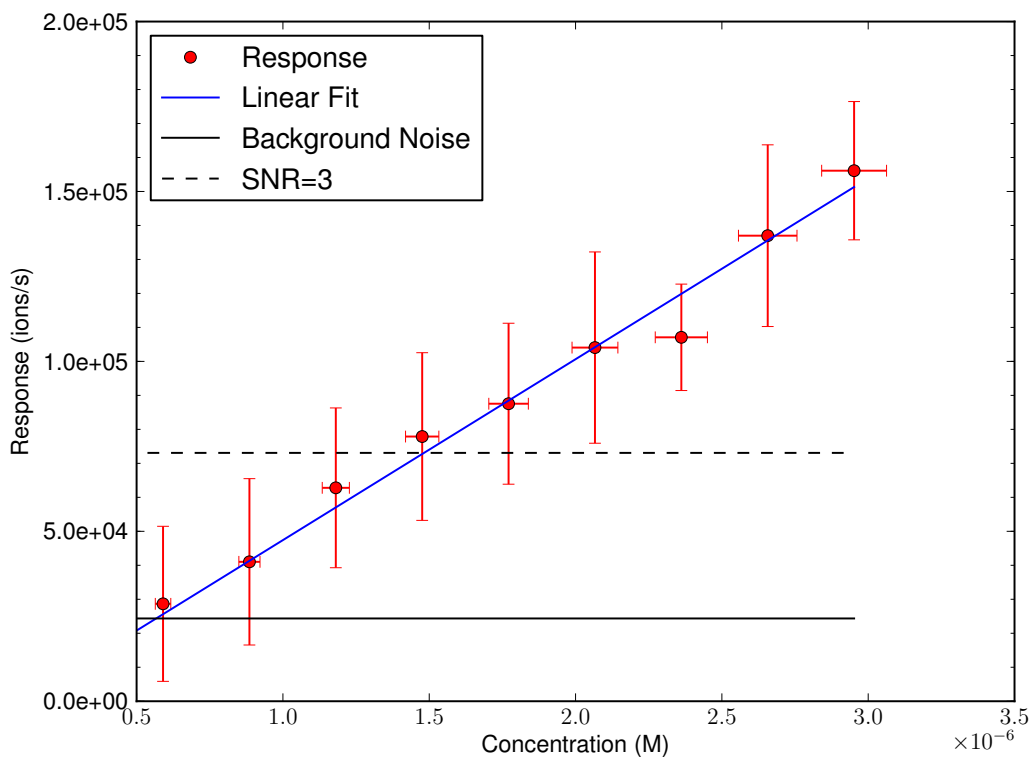


Figure 6.10: Instrument response as a function of concentration in low gain. Vertical error bars are 99% confidence intervals computed from the standard deviation of 30 measurements. Horizontal error bars are the propagated uncertainties from sample preparation. The limit of detection is interpolated as  $1.5 \pm 0.1 \times 10^{-6}$  mol/L, which corresponds to  $7.21 \pm 0.04 \times 10^4$  ions/s at the detector. Concentrations below the reported limit of detection are measurable because each data point is the average of 30 samples.

### 6.2.5 Dynamic Range

The linear dynamic range of the combined instrument was also investigated, using the same procedure described in Section 6.2.4.a, but with higher concentrations in addition to those listed. The response as a function of sample concentration for the combined instrument with the detector in high gain is shown in Figure 6.11. The response was linear up until the maximum response of the detector, then flattens out. Since all these data were measured using a 20 data point integration, this dynamic range is equivalent to a charge dynamic range. In high gain, this dynamic range is  $2.2 \pm 0.2$  orders of magnitude. This is a smaller dynamic range than measured for the detector alone ( $2.9 \pm 0.1$  orders of magnitude, Table 5.3). The mass spectrometer noise increased the minimum detectable charge, decreasing the charge dynamic range.

The response as a function of concentration for the combined instrument in low gain is shown in Figure 6.12. In this case, the the response is linear for only a small segment of the detector's dynamic range. As discussed above, the combined instrument suffered from a degradation in resolution due to focus and space charge effects. Because of this degradation in resolution, the total ion current for the  $CF_3^+$  peak was spread over a larger number of pixels at higher sample concentrations than at lower concentrations. The result was the instrument stopped responding linearly after only  $0.30 \pm 0.03$  orders of magnitude. To verify this conclusion, the ion current measured from all the pixels in the  $CF_3^+$  peak were added together and plotted in

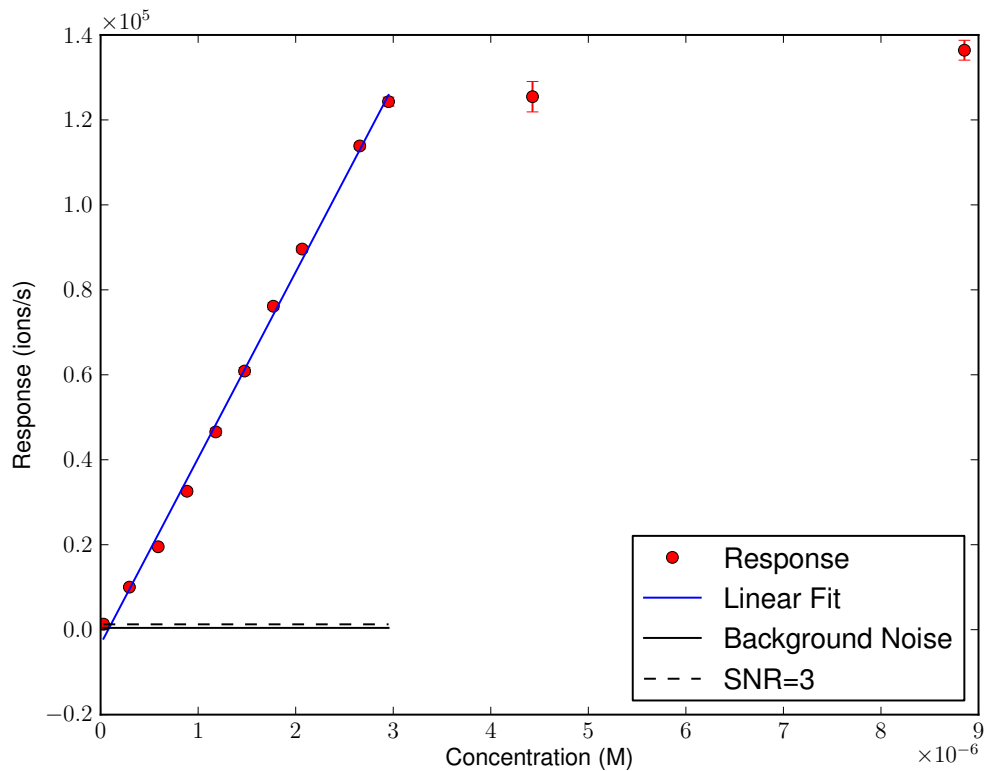


Figure 6.11: Dynamic range for the combined instrument with the detector in high gain. Vertical error bars are 99% confidence intervals computed from the standard deviation of 30 measurements. The dynamic range,  $2.2 \pm 0.2$  orders of magnitude, is not as large as expected ( $2.9 \pm 0.1$  orders of magnitude) due to noise from the instrument.

Figure 6.13. Using all the ion signal from the peak removes the influence of the space charge, and the charge dynamic range in low gain is as expected.

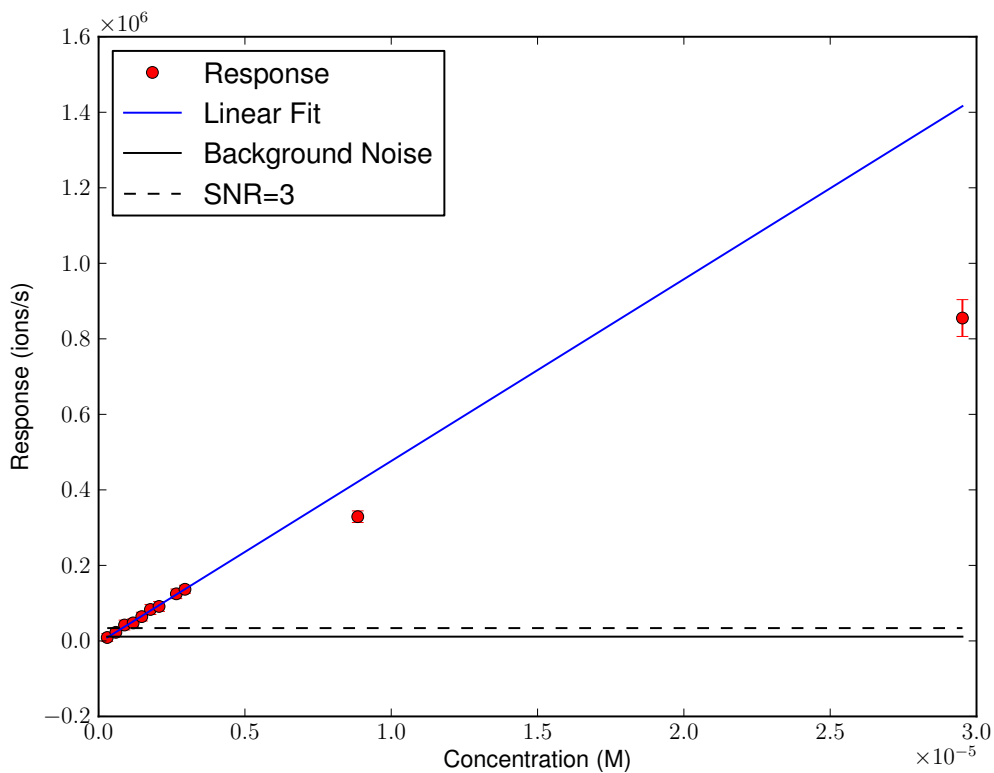


Figure 6.12: Dynamic range for the combined instrument with the detector in low gain. Vertical error bars are 99% confidence intervals computed from the standard deviation of 30 measurements. The dynamic range,  $0.30 \pm 0.03$  orders of magnitude, is substantially lower than expected. Peak broadening from increased space-charge effects as the sample concentration increases results in a non-linear peak height increase as the sample concentration increases.

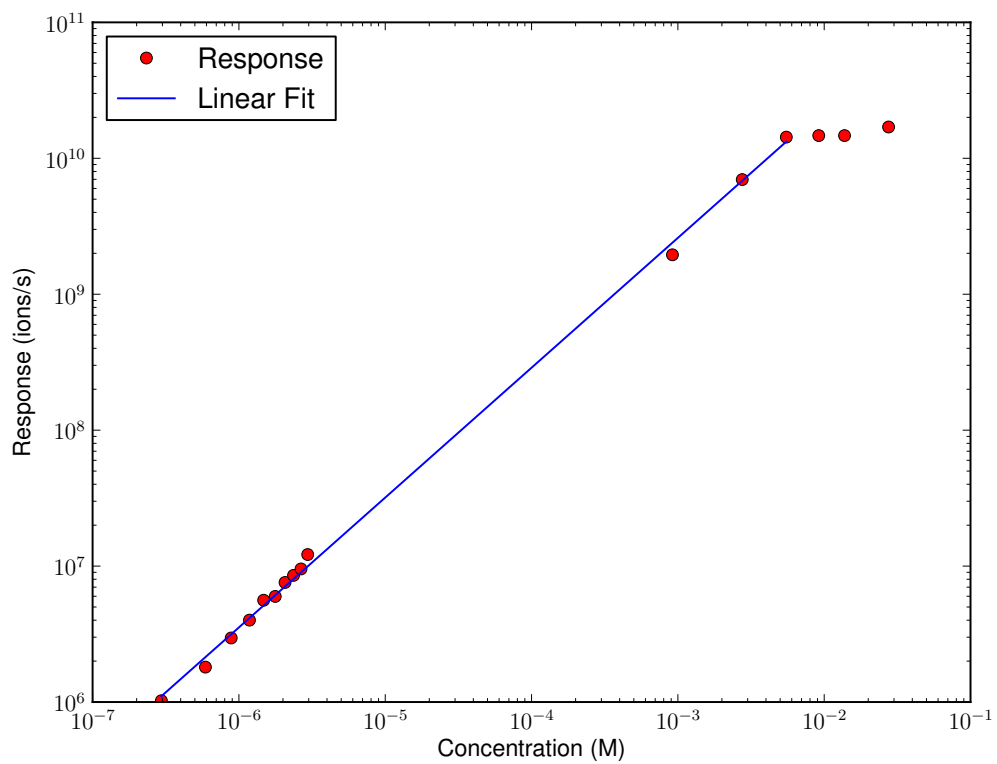


Figure 6.13: Response determined by peak area vs concentration in low gain. When the response is computed from peak area, rather than peak height, the response as a function of concentration remains linear, and the dynamic range is as expected.

### 6.3 Conclusions

Because the mass dispersion of a linear cycloid mass spectrometer was linear, it was expected that there would be many instruments reported that would take advantage of this property. Only a handful of such instruments have been reported. Smith and Adams reported a combination of a linear cycloid with a channel plate detector, read out by an array of copper strips, but only reported detection of a single peak with the electric field fixed (83, 84). Halas reported a linear cycloid with a pair of collectors for hydrogen isotope measurement (85). The mass spectrum presented in Figure 6.5 is, therefore, believed to be the first reported simultaneous detection of multiple masses using a linear cycloid with an array detector. In addition, the combined instrument is the first reported combination of a CTIA array detector with a linear cycloid. This combined instrument highlighted the linear mass dispersion of the linear cycloid, but suffered from resolution degradation due to mechanical difficulties with positioning the detector, design issues with the linear cycloid, and space charging. In addition, noise from the mass spectrometer resulted in lower sensitivity than expected, based on the characterization of the DM0025 1696 pixel CTIA array detector. The performance of the 1696 CTIA array detector combined with the Monitor Instruments linear cycloid mass spectrometer demonstrates the advantages of such a combination, but there is room for improvement. A more detailed discussion of improvements that can be made to the combined instrument is presented in Chapter 7.

## CHAPTER 7

### FUTURE DIRECTIONS

The primary purpose of this work was to combine a CTIA array detector with a linear cycloid and to evaluate the performance of the combined instrument. While this goal was accomplished, several limitations to the overall performance of the combined instrument, as well as limitations in the procedures used to characterize the detector were identified. The following sections present suggestions for overcoming the limitations encountered, allowing for the construction of a new linear cycloid mass spectrometer with a CTIA array detector with higher performance than the instrument described here.

#### 7.1 Detector Characterization

The calibration of the gain of the DM0025 detector should be repeated with a more stable ion gun. The OCI Vacuum Microengineering ion gun had problems regulating emission current, and produced a noisy ion beam. As discussed in Chapter 3.2.2, this poor regulation and noise prevented the use of mean variance analysis for detector gain characterization. A more stable ion gun would allow for better determination of the detector gain using the methods described in Chapter 5.1. In addition, a much more stable ion gun might be able to produce a shot noise limited ion beam,

thus allowing the gain of the whole array to be characterized using mean-variance analysis.

In addition, the behavior of the detector at lower temperatures than those used in Chapter 5 should be examined to better determine the optimum temperature to operate the device. A detailed characterization of noise like the one performed in Chapter 5.6 should be performed at a variety of temperatures, not just the lowest achievable temperature. Detailed information about the noise performance of the detector at different temperatures will allow detector performance to be estimated under operating temperatures different from the temperature characterized in this dissertation, which will be valuable information if the detector is used for applications where cryogenic temperatures are not easily obtainable, such as in a portable instrument. These data could be collected in a more efficient manner than presented in this dissertation through the construction of a testing platform specifically designed to characterize the DM0025 CTIA detector. This testing platform could be designed to mount on the current ion gun vacuum chamber, allowing the complete characterization of a detector to be performed easily. The testing platform should mount a detector on a small cooling block to minimize the amount of heat absorbed from thermal radiation from the vacuum chamber walls. In addition, a cooled thermal shield can be placed around the detector, further reducing the amount of extra heat on the cold side of the thermoelectric cooler. A test platform with these features should be able to characterize the detector at temperatures approaching -60

°C. If lower temperatures are required, alternative cooling strategies can be explored. The use of a new, more interchangeable detector package, described below, will allow multiple detectors to be characterized in rapid succession, allowing differences in detector performance due to the manufacturing process to be more thoroughly investigated.

## 7.2 Detector improvements

One change already in progress is the creation of a ceramic carrier mount for the DM0025 detector to replace the PCB daughter board currently in use. Like the daughter board, this ceramic carrier will integrate the power line bypass capacitors and output buffer amplifiers, but all the lines going from the carrier to the motherboard will be through connectors, making detector packages interchangeable. In addition, the carrier will be attached to a small piece of copper acting as a cooling bloc. This combined with the connectors will allow the detector package to be much more replaceable than the current design. Shrinking the copper block from its current large size to a much smaller size should also reduce the cooling requirements needed to lower the detector temperature to acceptable levels, because the radiant heat absorbed will be lower. This smaller detector package will also be significantly easier to mechanically attach to a mass spectrometer, helping to reduce accidental damage to the detector.

Future generations of CTIA array detector designs should correct all of the ob-

served deviations from ideal behavior (See Chapters 4.4 and 5.3). These deviations include the problems observed when the device in high gain with the global reset switch closed and the sample-and-hold switch open, the difference in average post-reset voltage between high and low gain, and the large spread in post-reset voltages. To improve sensitivity over the present generation of CTIA array detector, new detectors should be designed with lower read noise and dark current noise than the DM0025. Reducing the read noise should increase detector sensitivity for short integration times, while reducing the dark current noise should increase detector sensitivity for long integration times (See Chapter 3.4). Reducing both the read noise and the dark current noise should increase detector sensitivity for applications that require short integration times, as well as for applications than allow for long integration times.

### 7.3 Instrument Improvements

The biggest problem with the performance of the cycloidal mass spectrometer / CTIA detector combination is the inability to locate the detector on the instrument focal plane. This accounts for both the lower than expected resolution, as well as the decreased linear dynamic range. The main reason the the detector could not be positioned on the instrument focal plane was that the instrument itself was not designed around the array detector. The detector is wider than the ground plane of the instrument, making it mechanically difficult to position the detector in the focal

plane. In future work, the instrument must be redesigned to accommodate the new ceramic detector carriers in a pocket in the instrument ground plane such that the pocket acts as a shielding enclosure around the detector. Currently, the detector sits exposed above the ground plane with no electrical shielding, where it is subject to electrical noise from the voltage supplies powering the electric sector. In addition, the individual amplifiers are located on the edge of the detector die, where they are likely subject to ion impact from the fringes of the ion beam. Ions hitting the amplifiers instead of the Faraday electrodes can produce spurious noise signals or cause anomalous detector operation. By mounting the new detector package inside a pocket in the analyzer ground plane, the ground plane can act as a shield, reducing the detector's exposure to external noise. The opening in the pocket should be made large enough to allow ions to strike the detector electrodes, but prevent them from impacting anywhere else on the detector die. Additionally, thin grid wires could be stretched across the width of this opening to reduce penetration of external electric fields into the box. Positioning the wires perpendicular to the Faraday electrodes should ensure that the transmission loss for each wire affects each pixel in the same manner. By placing the detector package in the middle of the ground plane, where the voltage is close to zero, and by making the field free region inside the pocket small compared to the ion trajectories, the effect of the wires on resolution can be minimized. The number, size, and spacing of these wires should be optimized to maximize the signal-to-noise ratio. Minimizing the noise produced by all electrical

components in the vacuum chamber, especially the electric sector, will help reduce the need for these thin wires.

The geometry of the ground plane pocket should allow the focal plane to be moved both in front of and behind the detector surface. If the detector can be mechanically located in the approximate location of the focal plane, the actual focal plane location can be tuned electrically to achieve the best instrument resolution. Furthermore, the detector can be mechanically attached to the ground plane, improving instrument robustness.

In addition to widening the ground plane, the entire instrument must be slightly enlarged in order to take advantage of the array detector. Because the current instrument was designed for a single channel detector, there exists only a limited number of ion paths that are in uniform magnetic and electric fields. Even when optimally tuned, the current instruments unperturbed ion paths create a focal region covering approximately 0.35 inches, about 700 pixels, or a little over 40% of the array area. This severely reduced the mass range that can be simultaneously viewed.

One future application of this instrument/detector combination is explosives detection, but there are several further instrument changes that need to be made in order to optimize the instrument/detector combination for this purpose. The vapor pressures of many of the explosives of interest are low enough at room temperature that there is significant condensation of explosive residue on the inside of the inlet, as well as in the ion source when these samples are introduced into the instrument, even

under high vacuum. Therefore, to analyze these low vapor pressure samples, the instrument and inlet system must be heated. The new instrument should be divided into several thermally independent zones, including the ion source, the analyzer, and possibly the vacuum chamber housing the instrument. At minimum the ion source will need to be heated, but further experimentation will be needed to determine to what extent the analyzer temperature matters. The portion of the ground plane where the detector is attached will need to be thermally isolated from the other zones, because it needs to be cooled. The extent to which the detector will be heated due to radiant heat from the heated ion source and analyzer will need to be investigated in order to determine the power dissipation needed to cool the detector to an appropriate temperature.

In addition, several explosives of interest have mass peaks above the 200 amu limit of the current instrument. To provide better analyte identification, the upper mass range should be increased to at least 250 amu, possibly to 300 amu. Furthermore, it would be desirable to position the entire region of interest of the mass spectrum on the detector using a fixed electric field, allowing all mass peaks of an analyte to be measured simultaneously. However, there is a tradeoff between resolution and mass range on the detector. For a fixed detector position relative to the ion source, the mass dispersion must be lowered to increase the mass range. The resolution ( $m/\delta m$ ) decreases as the linear mass dispersion decreases because the peak width is controlled by the ion beam width at the entrance of the analyzer,

so the physical width of the ion beam does not change. A lower mass dispersion means that the physical beam width represents a larger mass spread, so  $\delta m$  is larger, decreasing resolution. Therefore, the ion beam width at the entrance of the analyzer must be made narrow enough to obtain the desired resolution for the highest mass of interest. Narrowing the ion beam width will have implications for overall sensitivity, however. As usual, a balance will have to be struck between sensitivity and resolution.

#### 7.4 Instrument Housing

The previous vacuum chamber design consisted of a rectangular chamber with a pair of 4.5" CF flanges welded on either side. On the top of the chamber there was an additional rectangular feed through. The magnet pole pieces pressed against the sides of the chamber, and the magnet yoke wrapped around the entire structure. With this configuration, it was extremely difficult to remove the magnet from around the vacuum chamber.

The new vacuum chamber should be designed to fit between the magnet pole pieces, but a further design requirement should be that the vacuum chamber can slide easily in and out of the magnet gap. This should be relatively easy to accomplish, as two of the flanges on the old vacuum can are unnecessary. The instrument, which should be mounted on a single flange, can easily slide into and out of the chamber, making accessing the instrument while it is in the vacuum chamber re-

dundant. The new vacuum chamber should consist of a rectangular chamber welded to a flange at one end and sealed at the other. With this configuration, the chamber should easily slide in and out of the magnet gap. This arrangement will facilitate the heating of the vacuum can for bake-out and degassing purposes as well. The magnet can be easily removed while the chamber is heated to remove possible contaminates and adsorbed water vapor. After bake-out is complete and the chamber cooled, the magnet can be returned around the vacuum chamber.

## 7.5 Instrument Control Electronics

The electronics used to control the instrument should also be redesigned. As shown in the limits of detection studies, the environmental noise in the instrument is sufficiently high as to seriously degrade the limits of detection in high gain. There is room for improvement in both the baseline noise characteristics of powers supplies and overall control board, as well as improvements to shielding the connections between the control board and the instrument. The buffer amplifiers on the detector package will help reduce the noise pickup out side of the vacuum chamber by increasing the magnitude of the signal and lowering impedance, but noise introduced inside the vacuum chamber from interconnecting wiring will still be picked up by the detector. Therefore, wiring from power supplies into the vacuum chamber must be shielded, and power supplies must have bypass capacitors and be properly grounded to the vacuum chamber.

Preliminary work has been done by the Denton research group into building custom instrument control and data collection systems based around the ARM family of microprocessors. These low power, high performance microprocessors offer the ability to combine control, data collection, and data processing in one package. New instrument control electronics could be designed with this in mind, using actuator controlled pots to provide the voltages for the analyzer, as well as voltage monitoring circuits. A central ARM CPU controlling these voltages and monitors, as well as the detector and analog to digital converters could use sophisticated control algorithms to optimize instrument performance on the fly. The instrument parameter space could be automatically characterized once when each instrument is assembled. With the instrument tuned to a manually determined optimum, small changes in instrument performance could be corrected by running a gradient ascent tuning algorithm, which could quickly return the instrument to optimal tuning. Changes in operating environment, such as magnet temperature, aging, or new setups could also be automatically optimized using autonomous dynamic tuning.

Further improvements to the instrument control electronics could also allow modulation schemes to be explored. Modulation of the ion signal may allow for improvements in signal-to-noise ratios through lock-in amplification as well as other demodulation techniques. While the spatial modulation of the ion beam relies on the mass peaks being sparse in the spectrum, modulation of the ionizer biases would allow amplitude modulation of all mass peaks regardless of their spacing.

## 7.6 Data Collection System Improvements

The current data collection system also has room for improvement. With the current arrangement, each pixel can only be sampled at about 72 Hz. In the current configuration, the two sets of pixels are sampled sequentially instead of simultaneously. In a future date collection scheme, fully independent sets of control lines can be used, so that the two sides of the detector can be collected at the same time, doubling the sampling frequency. Additionally, the currently employed National Instruments PCI-6281 card acts as a significant limitation on the data collection system. Because the detector clock is generated from the NI card, the detector can only be run at half the speed the card is running at. This sets an upper limit on data collection speed, because the maximum speed for the NI card acquiring two channels is only 250 kHz. Therefore, the detector can only be clocked at half this frequency, or 125 kHz.

A data collection system based on the ARM family of microprocessors described above would significantly improve the capabilities of the acquisition system by allowing the generation of high speed control signals. Furthermore, new high speed analog to digital converters with serial interfaces allow multiple analog to digital converters to be easily controlled by a single microprocessor, making it simple to sample multiple signals truly simultaneously with high sample rates. A custom control and data collection system could realistically run the DM0025 at 1 MHz, boosting the sampling rate of each pixel to over 1 kS/s.

A higher sampling rate will allow better characterization of the noise, both from the detector itself as well as from the environment. Improvements in the noise characterization may allow modulation schemes to further improve sensitivity. In addition, higher sampling rates should improve the linear dynamic range of the instrument. The linear dynamic range is limited by the time it takes to acquire the minimum number of points to perform a linear regression. The faster these points can be acquired, the more sample can be measured before detector saturation.

A new analog-to-digital converter could also address the input range of the National Instruments PCI-6281 card and reduce the noise contribution from the ADC. As explained in Chapter 5.6.1, the NI PCI-6281 has several bipolar (positive and negative) input ranges, but the DM0025 only outputs 0 to 3.3V, 0 to 6.6 V after the output buffer amplifiers on the daughter board. The  $\pm 10V$  input range of the NI PCI-6281 card is the only NI PCI-6281 card input range that can measure the signals from the output of the buffer amplifiers, but over 50% of the input range is wasted. Using an analog-to-digital converter with an input range that can be adjusted to 0 to 6.6 V will reduce the size of the least-significant bit of the analog-to-digital converter, thereby reducing the noise contribution from the ADC.

## APPENDIX A

### DERIVATIONS

#### A.1 Output Voltage from an Input Voltage Noise

The output voltage resulting from a voltage noise on the input can be calculated by evaluating the model with only the input voltage noise source present.

Applying Kirchhoff's current law to node  $a$  and assuming the amplifier has infinite input impedance results in the following equation:

$$C_g s [E_n(s) - V_g(s)] + C_f s [E_n(s) - V_0(s)] = 0 \quad (\text{A.1})$$

Setting  $V_g = 0$ , rearranging and solving for  $\frac{V_o(s)}{E_n(s)}$  yields the transfer function for input voltages.

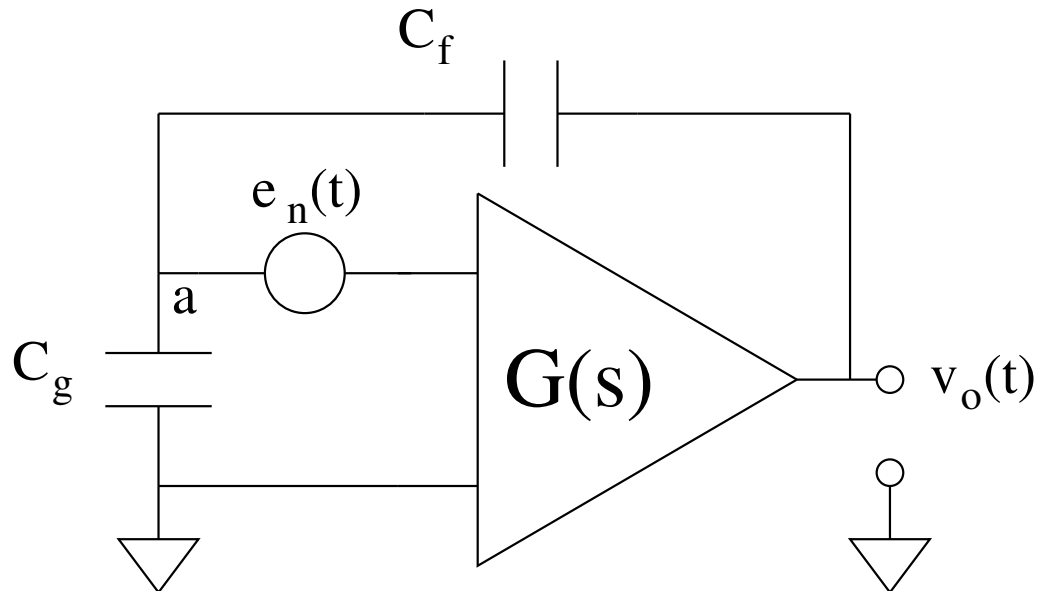
$$H(s) = \frac{V_o(s)}{E_n(s)} = \frac{C_f + C_g}{C_f} \quad (\text{A.2})$$

Taking the inverse Laplace transform of Equation A.2 gives the impulse response function:

$$h(t) = \frac{C_f + C_g}{C_f} \delta(t) \quad (\text{A.3})$$

The output voltage for an arbitrary input voltage noise  $e_n(t)$  is given by the convolution integral

$$v_o(t) = e_n(t) * \frac{C_f + C_g}{C_f} \delta(t) \quad (\text{A.4})$$



(a) Time domain model

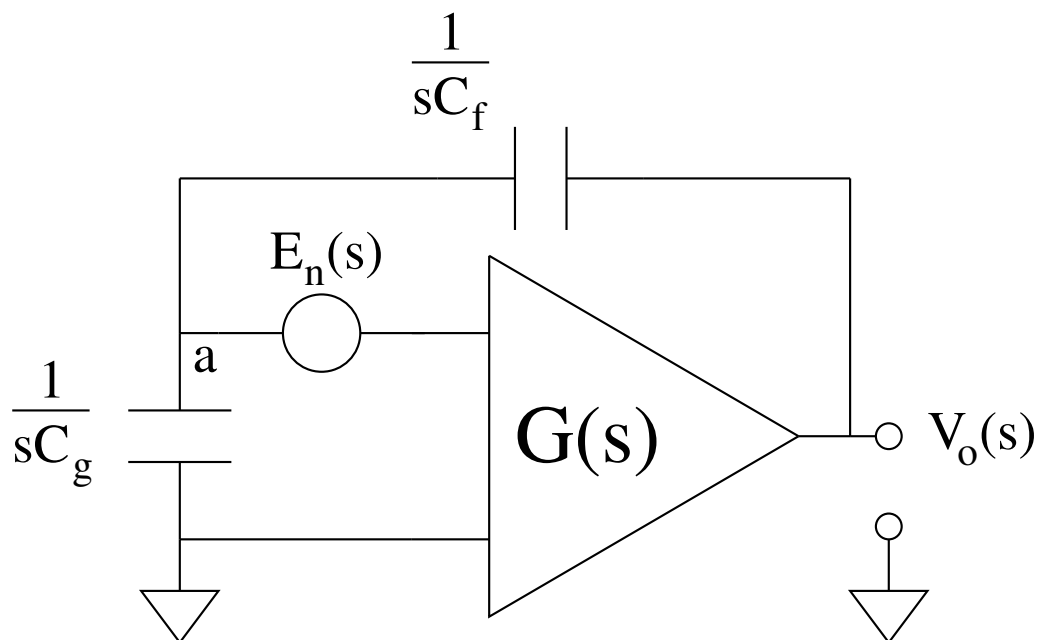
(b)  $s$  domain model

Figure A.1: Linear model of a CTIA with only the input voltage noise source.

Because the convolution of a function with  $\delta(t)$  is just the function evaluated at  $t$ , the output voltage is just the input voltage scaled by  $\frac{C_f + C_g}{C_f}$ , meaning the voltage response of the circuit is simply a voltage follower with gain.

## A.2 Output Variance from an Input Voltage Noise Source

Because the voltage impulse response for this circuit is just a scaled delta function, the output autocovariance can be calculated in terms of an arbitrary input autocovariance. If the input autocovariance is  $C_{xx}(t_1, t_2) = C_{\nu\nu}(t_1, t_2)$  for some arbitrary voltage  $\nu(t)$  the cross covariance is

$$C_{\nu y} = C_{\nu\nu}(t_1, t_2) * \frac{C_f + C_g}{C_f} \delta(t_2) = \frac{C_f + C_g}{C_f} C_{\nu\nu}(t_1, t_2) \quad (\text{A.5})$$

and the output autocovariance is

$$C_{yy} = \frac{C_f + C_g}{C_f} C_{\nu\nu}(t_1, t_2) * \frac{C_f + C_g}{C_f} \delta(t_1) \quad (\text{A.6})$$

$$= \frac{(C_f + C_g)^2}{C_f^2} C_{\nu\nu}(t_1, t_2) \quad (\text{A.7})$$

$$= \frac{(C_f + C_g)^2}{C_f^2} \sigma_\nu^2(t) \quad (\text{A.8})$$

## A.3 Generalized Least Squares Variance with Time Increasing Variance

The variance of the generalized least squares estimator is given by (56, 61)

$$V(\mathbf{b}_{\text{GLS}}) = (\mathbf{X}^T \boldsymbol{\Sigma}^{-1} \mathbf{X})^{-1} \quad (\text{A.9})$$

As explained in Section 3.4.2.b, the error matrix for the generalized least squares regression is:

$$\Sigma = \begin{bmatrix} \sigma_{dc}^2 1 dt & 0 & \cdots & 0 \\ 0 & \sigma_{dc}^2 2 dt & \cdots & 0 \\ \vdots & \vdots & \ddots & \vdots \\ 0 & 0 & \cdots & \sigma_{dc}^2 (N-1) dt \end{bmatrix} \quad (\text{A.10})$$

The inverse of a diagonal matrix is just the inverse of each element on the diagonal (70), so

$$\Sigma^{-1} = \begin{bmatrix} \frac{1}{\sigma_{dc}^2 1 dt} & 0 & \cdots & 0 \\ 0 & \frac{1}{\sigma_{dc}^2 2 dt} & \cdots & 0 \\ \vdots & \vdots & \ddots & \vdots \\ 0 & 0 & \cdots & \frac{1}{\sigma_{dc}^2 (N-1) dt} \end{bmatrix} \quad (\text{A.11})$$

The matrices  $\mathbf{X}$  and  $\mathbf{X}^T$  are given by

$$\mathbf{X} = \begin{bmatrix} 1 & 1 dt \\ 1 & 2 dt \\ \vdots & \vdots \\ 1 & (N-1) dt \end{bmatrix} \quad (\text{A.12})$$

and

$$\mathbf{X}^T = \begin{bmatrix} 1 & 1 & \cdots & 1 \\ 1 dt & 2 dt & \cdots & (N-1) dt \end{bmatrix} \quad (\text{A.13})$$

For this  $\mathbf{X}$  matrix, the parameter vector  $\mathbf{b}$  is

$$\mathbf{b} = \begin{bmatrix} b_0 \\ b_1 \end{bmatrix} \quad (\text{A.14})$$

where  $b_0$  is the intercept and  $b_1$  is the slope.

Carrying out the first multiplication,  $\mathbf{X}\Sigma^{-1}$  yields

$$\begin{aligned} \mathbf{X}\Sigma^{-1} &= \begin{bmatrix} 1 & 1 & \cdots & 1 \\ 1 dt & 2 dt & \cdots & (N-1) dt \end{bmatrix} \begin{bmatrix} \frac{1}{\sigma_{dc}^2 1 dt} & 0 & \cdots & 0 \\ 0 & \frac{1}{\sigma_{dc}^2 2 dt} & \cdots & 0 \\ \vdots & \vdots & \ddots & \vdots \\ 0 & 0 & \cdots & \frac{1}{\sigma_{dc}^2 (N-1) dt} \end{bmatrix} \\ &= \begin{bmatrix} \frac{1}{\sigma_{dc}^2 1 dt} & \frac{1}{\sigma_{dc}^2 2 dt} & \cdots & \frac{1}{\sigma_{dc}^2 (N-1) dt} \\ \frac{1}{\sigma_{dc}^2} & \frac{1}{\sigma_{dc}^2} & \cdots & \frac{1}{\sigma_{dc}^2} \end{bmatrix}_{[2 \times (N-1)]} \end{aligned}$$

Completing the next matrix multiplication yields

$$\begin{aligned} \mathbf{X}^T \Sigma^{-1} \mathbf{X} &= \begin{bmatrix} \frac{1}{\sigma_{dc}^2 1 dt} & \frac{1}{\sigma_{dc}^2 2 dt} & \cdots & \frac{1}{\sigma_{dc}^2 (N-1) dt} \\ \frac{1}{\sigma_{dc}^2} & \frac{1}{\sigma_{dc}^2} & \cdots & \frac{1}{\sigma_{dc}^2} \end{bmatrix}_{[2 \times (N-1)]} \begin{bmatrix} 1 & 1 dt \\ 1 & 2 dt \\ \vdots & \vdots \\ 1 & (N-1) dt \end{bmatrix}_{[(N-1) \times 2]} \\ &= \begin{bmatrix} \frac{1}{\sigma_{dc}^2 dt} \sum_{i=1}^{N-1} \frac{1}{i} & \frac{N-1}{\sigma_{dc}^2} \\ \frac{N-1}{\sigma_{dc}^2} & \frac{dt}{\sigma_{dc}^2} \sum_{i=1}^{N-1} i \end{bmatrix}_{[2 \times 2]} \\ &= \begin{bmatrix} \frac{H_{N-1}}{\sigma_{dc}^2 dt} & \frac{N-1}{\sigma_{dc}^2} \\ \frac{N-1}{\sigma_{dc}^2} & \frac{dt}{\sigma_{dc}^2} \frac{N(N-1)}{2} \end{bmatrix}_{[2 \times 2]} \end{aligned}$$

where

$$\sum_{i=1}^{N-1} \frac{1}{i} = H_{N-1} \quad (\text{A.15})$$

and  $H_{N-1}$  is the  $(N - 1)$ th harmonic number and

$$\sum_{i=1}^{N-1} i = \frac{N(N-1)}{2} \quad (\text{A.16})$$

The covariance matrix is the inverse of the matrix in Equation A.15. Because it is a  $[2 \times 2]$  matrix and none of the elements are zero it can be inverted directly (70) to give

$$V(\mathbf{b}_{\text{GLS}}) = \frac{2\sigma_{dc}^4}{H_{N-1}N(N-1) - 2(N-1)^2} \begin{bmatrix} \frac{dt}{\sigma_{dc}^2} \frac{N(N-1)}{2} & -\frac{N-1}{\sigma_{dc}^2} \\ -\frac{N-1}{\sigma_{dc}^2} & \frac{H_{N-1}}{\sigma_{dc}^2 dt} \end{bmatrix} \quad (\text{A.17})$$

The variance of the slope estimator is the second diagonal element of A.17, which evaluates to

$$V(b_1) = \frac{2\sigma_{dc}^2}{dt} \frac{H_{N-1}}{(N-1)[(H_{N-1}-2)N+2]} \quad (\text{A.18})$$

#### A.4 Derivation of Ion Trajectories in a Linear Cycloid Mass Spectrometer

This section presents a derivation of ion trajectories in a linear cycloid mass spectrometer. This derivation is taken from (44).

The equation of motion for an ion in static electric and magnetic fields is:

$$\vec{F} = q\vec{E} + q\vec{v} \times \vec{B} \quad (\text{A.19})$$

where  $q$  is the elementary charge, and  $\vec{F}$ ,  $\vec{E}$ , and  $\vec{B}$  are the force, electric field, and magnetic induction vectors and  $\vec{v}$  is the ion velocity vector. Expanding these vectors

and evaluating the cross product yields:

$$F_x = m\ddot{x} = q[E_x + (\dot{y}B_z - \dot{z}B_y)] \quad (\text{A.20})$$

$$F_y = m\ddot{y} = q[E_y - (\dot{x}B_z - \dot{z}B_x)] \quad (\text{A.21})$$

$$F_z = m\ddot{z} = q[E_z + (\dot{x}B_y - \dot{y}B_x)] \quad (\text{A.22})$$

using Newton's dot notation:

$$\dot{x} = \frac{dx}{dt} \quad (\text{A.23})$$

$$\ddot{x} = \frac{d^2x}{dt^2} \quad (\text{A.24})$$

Recognizing that  $E_x = E_z = 0$  and  $B_x = B_y = 0$ , Equations A.20 - A.22 reduce to:

$$m\ddot{y} = qE - qB\dot{x} \quad (\text{A.25})$$

$$m\ddot{x} = qBy \quad (\text{A.26})$$

By setting  $t = 0$  when  $x = y = 0$  and solving these differential equations, the equations of motion for an ion in these crossed fields can be derived as:

$$x = N\sin(\varphi) - N\sin(\gamma t + \varphi) + (E/B)t \quad (\text{A.27})$$

$$y = N\cos(\varphi) - N\cos(\gamma t + \varphi), \quad (\text{A.28})$$

where  $\gamma$  is defined as:

$$\gamma = \frac{qB}{m} \quad (\text{A.29})$$

and  $N$  and  $\varphi$  are parameters that depend on the initial velocity. It is difficult to eliminate time from Equations A.27 and A.28, but it is apparent that these equations

are the same as the equations for a trochoid, from (44–46):

$$x = a\psi - a\psi_0 + \rho\sin(\psi_0) - \rho\sin\psi \quad (\text{A.30})$$

$$y = L - \rho\cos(\psi) = \rho\cos(\psi_0) - \rho\cos(\psi) \quad (\text{A.31})$$

The prolate cycloid the locus of the end of an arm attached to a wheel rolling on a line, as seen in Figure A.2. The meanings of  $a$ ,  $\psi$ ,  $\rho$ , and  $L$  can be seen in Figure A.2. Comparing Equations A.27 and A.28 with A.30 and A.31 yields:

$$a = \frac{E}{B^2} \frac{m}{q} \quad (\text{A.32})$$

$$\rho = N \quad (\text{A.33})$$

$$\phi = (\gamma t + \varphi) \quad (\text{A.34})$$

$$\phi_0 = \varphi \quad (\text{A.35})$$

Because of the periodic nature of trochoid, charged particles that cross a plane  $y = y_0$  at some value  $x_0$  will again cross the plane  $y = y_0$  at  $x = x_0 + b$  where:

$$b = 2\pi a = 2\pi \frac{E}{B^2} \frac{m}{q} \quad (\text{A.36})$$

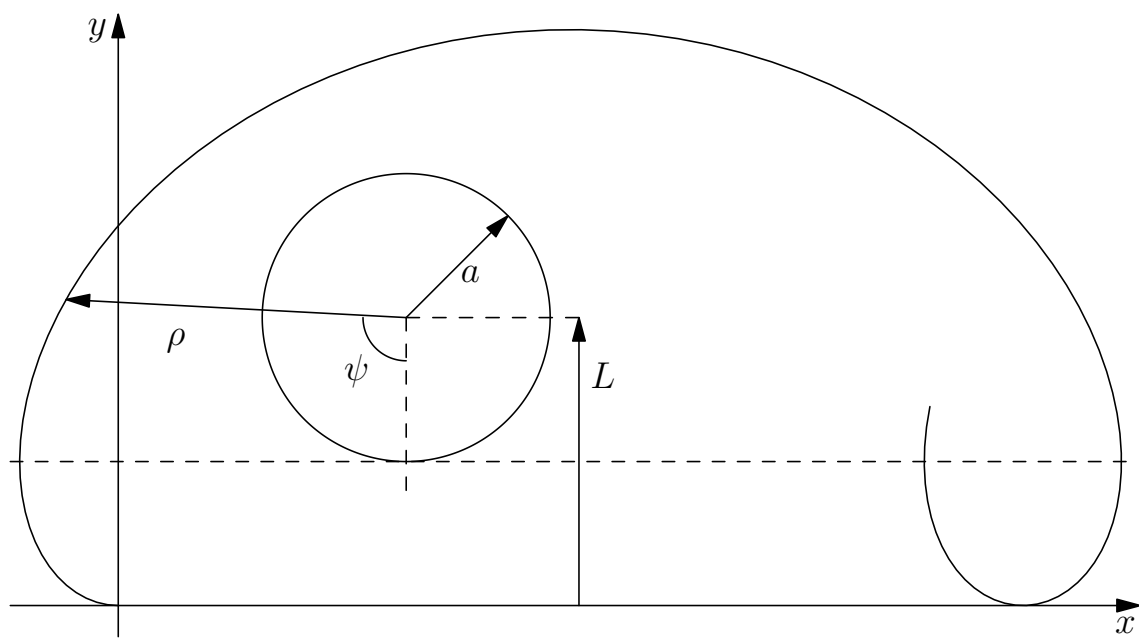


Figure A.2: The locus of the end of an arm of length  $\rho$  attached to a wheel of radius  $a$  rolling on a line.

## APPENDIX B

### CHARACTERIZATION OF SUPPORTING ELECTRONICS

The detailed characterization of a detector depends on several supporting electronics that need to be characterized before they can be used. For characterizing the DM0025 CTIA array detector, two primary components were used: a National Instruments PCI-6281 (NI 6281) analog to digital converter (ADC), and a Texas Instruments/Burr Brown ACF2101 low noise switched integrator. The NI 6281 ADC was used to digitize all measured signals for computer processing and analysis. The ACF2101 was used in the characterization of the gain of the DM0025 detector (Chapter 5.1).

#### B.1 NI PCI-6281 ADC Noise

The primary parameter of interest of the NI 6281 ADC is its noise. Any measurements of the noise of a device will be influenced by the noise of the ADC used to make those measurements. Therefore, it is important to characterize the ADC noise to determine the amount of influence the ADC noise has on other noise measurements.

$\pm 100\text{mV}$	$\pm 10\text{V}$
$9.9 \pm 0.2 \mu\text{V}$	$69 \pm 1 \mu\text{V}$

Table B.1: Voltage noise of the PCI-6281 ADC

### B.1.1 Experimental Procedure

The NI 6281 ADC noise was characterized by shorting the ADC's two inputs together. The fluctuations in the values reported by the ADC represent the noise due to analog to digital conversion. The ADC was sampled 10,000 times at 247,000 samples per second and this data collection was repeated 201 times to determine statistical means and standard deviations. Only two of the analog to digital converters input ranges were measures:  $\pm 100 \text{ mV}$  and  $\pm 10 \text{ mV}$ .

### B.1.2 Results

The noise for each input range is summarized in Table B.1. For the  $\pm 10 \text{ V}$  range, the majority of this noise comes from the process of digitizing the signal. For the  $\pm 100 \text{ mV}$  range there is some contribution from other noise in the ADC.

## B.2 Characterization of the Burr Brown ACF2101 Switched Integrator

The ACF2101 is a low noise, dual channel switched integrator, currently produced by Texas Instruments. It contains a pair of internal 100 pF capacitors, plus a pair of matched FET switched. The internal capacitors can be bypassed and external capacitors used in their place. The ACF2101 used for these studies had a 10 pF

capacitor in the feedback loop.

### B.2.1 Gain Calibration

In order to use the ACF2101 for calibrating other detectors, its gain must first be calibrated.

#### B.2.1.a Experimental Parameters

The ACF2101 gain was calibrated using a  $10.75 \pm 0.01 \text{ M}\Omega$  resistor connected to its input. The resistance was measured with a Fluke PM6303A automatic RLC meter at 1000 Hz. A series of voltages, from 10 mV up to 200 mV, were applied to this resistor using an Agilent 33220A function generator. A voltage across a resistor produced a current which was then integrated by the ACF2101. The output voltage with respect to ground was sampled differentially 10,000 times at 24.7 kHz, for a total integration time of 0.4 s, using a National Instruments PCI-6281 Multifunction card, with the analog to digital range set to  $\pm 100 \text{ mV}$ . Data was collected 201 times to obtain good statistical estimates of the parameters of interest. The ACF2101 amplifier and input resistor were housed in a grounded metal box to minimize external noise.

#### B.2.1.b Results

A plot of the slope of the output response vs input current can be seen in Figure B.1. Both the input currents and the output slopes are referenced to the first measurement point. There are several unknowns to be contended with in this experiment.

First of all, while the absolute voltage difference produced by the function generator is not exactly the same as the function generator display indicates, the voltage changes are linear, so for example, doubling the setting on the signal generator produces double the voltage output. Secondly, the amplifier itself has an input voltage offset. This means that the voltage at the input is not exactly at ground, but at some offset. The specification sheet for the ACF2101 indicates that this value is typically 3 mV, but it is difficult to measure for an individual device. Finally, the input bias (dark) current produces a response that is added to output caused by the input currents. By measuring the change in output response with respect to the change in input current, however, the effect of these unknowns can be eliminated. The currents used to calibrate the gain were in the nanoamp range (1 to 18 nA, see Figure B.1) to minimize the influence of the dark current (typically 100 fA or less) on the gain measurements. This gain corresponds to a feedback capacitor of  $10.0 \pm 0.1$  pF.

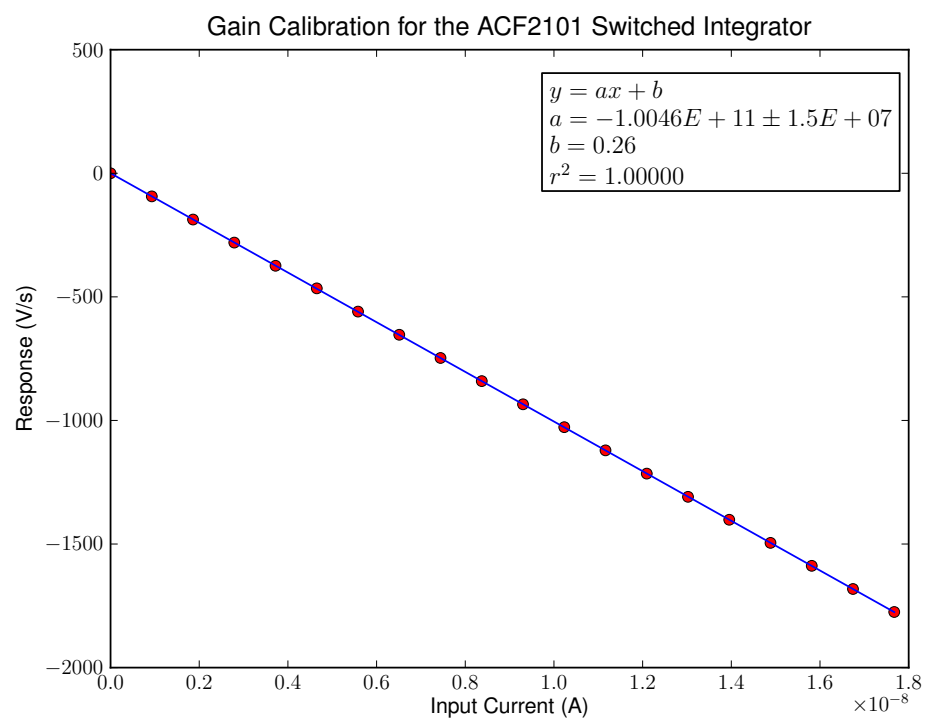


Figure B.1: Calibration of the gain of the ACF2101 switched integrator

### B.2.2 Post-Reset and Dark Current Characterization

Because of random thermal motion of charge carriers in the reset FET channel, when the device comes out of reset there is a random number of carriers present on the feedback capacitor, which produces a random offset voltage, referred to as the post-reset voltage. Because the output signal is typically measured as a voltage change, the effect of the post-reset voltage can be eliminated through linear regression.

#### B.2.2.a Experimental Procedure

The output voltage with respect to ground was sampled differentially 10,000 times at 24.7 kHz, for a total integration time of 0.4 s, using a National Instruments PCI-6281 Multifunction card, with the analog to digital range set to  $\pm 100$  mV. Data was collected 201 times to obtain good statistical estimates of the parameters of interest. The ACF2101 amplifier and input resistor were housed in a grounded metal box to minimize external noise.

#### B.2.2.b Results

While the magnitude of the post-reset voltage can be directly measured, the variance requires slightly more work. Assuming the post-reset variance is uncorrelated with other noise sources, the variance of the first data point collected after reset,  $\sigma_1^2$ , can be separated into two components: the post-reset voltage variance,  $\sigma_{PRV}^2$ , and another variance,  $\sigma_{other}^2$ , which represents variances from all other sources on the

output, including variance due to dark current, output noise, etc.

$$\sigma_1^2 = \sigma_{PRV}^2 + \sigma_{other}^2 \quad (\text{B.1})$$

Because the post-reset voltage offset is the same for all points in a single integration period and because the other noise is assumed to be uncorrelated in time, by subtracting the first point from the second the effect of the post reset variance can be assumed to be eliminated. The variance of this difference, then, is:

$$\sigma_{dif}^2 = 2\sigma_{other}^2 \quad (\text{B.2})$$

because the uncorrelated variances add. The post-reset variance can then be computed from Equation B.1. These values can be found in Table B.2.

The amplifier gain determined in Section B.2.1 can be used to determine the absolute value of the dark current. The standard deviation of the dark current is fairly large compared to the magnitude of the dark current because the dark current magnitude varies about zero. The dark current measured for this particular ACF2101 is much lower than the average dark current at room temperature indicated in the manufacturers ACF2101 specifications (70 fA) (86).

Parameter	
Gain	$-16.1 \pm 0.1 \text{ nV}/e^-$
Measured Dark Current	$3.0 \pm 12 \text{ fA}$
Dark Current (from (86))	typ 100 fA
Post-Reset Noise	$0.18 \pm \text{ mV}$
Output Noise	$40 \pm 1 \mu\text{V}$
Input Noise ( $e^-$ )	$2.50 \pm 0.07 \times 10^3$
FSR (V)	10 V
Linearity (%FSR, from (86))	$\pm 0.01$
Dynamic Range	5.4

Table B.2: Characterized parameters of the ACF2101 switched integrator

## REFERENCES

- [1] Becker, J. S. *Inorganic Mass Spectrometry: Principles and Applications*; John Wiley & Sons, Inc: New York, 2007.
- [2] Schilling, G. D.; Andrade, F. J.; Barnes, J. H.; Sperline, R.; Denton, M. B.; Barinaga, C. J.; Koppenall, D. W.; Hieftje, G. M. *Analytical Chemistry* **2007**, *79*, 7662–7668.
- [3] Kristo, M. J.; Enke, C. G. *Review of Scientific Instruments* **1988**, *59*, 438–42.
- [4] Industries, B. *Channeltron Electron Multiplier Handbook*, Technical Bulletin, ChannelBook.pdf.
- [5] Stresau, D.; Hunter, K.; Shiels, W.; Raffin, P.; Benari, Y. A New Class of Robust Sub-nanosecond TOF Detectors with High Dynamic Range. *54th ASMS Conference on Mass Spectroscopy*, 2006.
- [6] Jackson, W. J. *Physical Review* **1926**, *28*, 524–530.
- [7] Koppenall, D. W.; Barinaga, C. J.; Denton, M. B.; Sperline, R.; Hieftje, G. M.; Schilling, G. D.; Andrade, F. J.; Barnes, J. H. *Analytical Chemistry* **2005**, *77*, 418A–427A.
- [8] Boerboom, A. J. H. *Organic Mass Spectrometry* **1991**, *26*, 9290935.
- [9] Liu, A. D.; van Espen, P.; Adams, F. *Analytica Chimica Acta* **1987**, *198*, 71–79.
- [10] Franzen, J.; Maurer, K. H.; Schuy, K. D. *Zeitschrift fur Naturforschung, Teil A: Astrophysik, Physik, und Physikalische Chemie* **1966**, *21*, 37–62.
- [11] Freudenthal, J.; Jacobs, F. W. *International Journal of Mass Spectrometry and Ion Physics* **1983**, *46*, 115–18.
- [12] Honig, R. E.; Wollston, J. R.; Kramer, D. A. *Review of Scientific Instruments* **1967**, *38*, 1703–7.
- [13] Kennicott, P. R. *Analytical Chemistry* **1965**, *37*, 313–14.
- [14] Grais, K. I.; Bastawros, A. M.; El-Adl, E. H. *Indian Journal of Pure and Applied Physics* **1992**, *30*, 344–6.
- [15] Barnes, J. H.; Hieftje, G. M. *International Journal of Mass Spectrometry* **2004**, *238*, 33–46.

- [16] Belshaw, N. S.; Freedman, P. A.; O'Nions, R. K.; Frank, M.; Gou, Y. *International Journal of Mass Spectrometry* **1998**, *181*, 51–58.
- [17] Freedman, P. A.; Hall, E. F. H. *Multiple-Detector System for Detecting Charged Particles*, US Patent 5471059, 1995.
- [18] Brown, L.; Carelson, R. W.; Shirey, S. B. *Multiple Ion Multiplier Detector for a Mass Spectrometer*, US Patent 5220167, 1993.
- [19] Wiza, J. L. *Nuclear Instruments and Methods* **1979**, *162*, 587–601.
- [20] Goodrich, G. W. *Aparatus for Suppression of Ion Feenback in Electron Multipliers*, US Patent 3374380, 1968.
- [21] Birkinshaw, K. *Joirnal of Mass Spectrometry* **1997**, *32*, 795–806.
- [22] Knight, A. K. *Ph.D. Dissertation*, University of Arizona, 2006.
- [23] Giffin, C. E.; Boettger, H. G.; Norris, D. D. *International Journal of Mass Spectrometry and Ion Physics* **1974**, *15*, 437–449.
- [24] Sims, G. R.; Cook, J. J. *High-resolution scintillation screen for digital imaging*, US Patent 20070057195, 7285786, WO Patent 2007030499, 2007.
- [25] Hicks, P. J.; Davel, S.; Wallbank, B.; Comer, J. *Journal of Physics E: Scientific Instrumets* **1980**, *13*, 713–715.
- [26] Riegler, G. R.; More, K. A. *IEEE Transactions on Nuclear Science* **1973**, *20*, 102–106.
- [27] Hill, J. A.; Biller, J. E.; Biemann, K. *International Journal of Mass Spectrometry and Ion Processes* **1991**, *111*, 1–25.
- [28] Cody, R. B.; Tamura, J.; Finch, J. W.; Musselman, B. D. *Journal of the American Society for Mass Spectrometry* **1994**, *5*, 194–200.
- [29] Sinha, M. P.; Wadsworth, M. *Review of Scientific Instruments* **2005**, *76*, 025103.
- [30] Fuerstenau, S.; Soli, G.; Cunningham, T.; Hancock, B.; Pain, B.; Sinha, M. P. *International Journal of Mass Spectrometry* **2002**, *215*, 101–11.
- [31] Scheidemann, A. A.; Darling, R. B.; Schumacher, F. J.; Isakharov, A. *Journal of Vacuum Science & Technology A* **2002**, *20*, 597–604.
- [32] Darling, R. B.; Scheidemann, A. A.; Bhat, K. N.; Chen, T. C. *Sensors and Acuators A* **2002**, *95*, 84–93.

- [33] Knight, A. K.; Sperline, R.; Hieftje, G. M.; Young, E. T.; Barinaga, C. J.; Koppenall, D. W.; Denton, M. B. *International Journal of Mass Spectrometry* **2002**, *215*, 131–139.
- [34] Babis, J. S.; Sperline, R. P.; Knight, A. K.; Jones, D. A.; Gresham, C. A.; Denton, M. B. *Analytical and Bioanalytical Chemistry* **2009**, *395*, 411–419.
- [35] Gresham, C. A.; Rodacy, P. J.; Denton, M. B. *Micro Faraday-element array detector for ion mobility spectroscopy*, US Patent 6809313, 2004.
- [36] Maas, J. D.; Hendricks, P. I.; Ouyang, Z.; Cooks, R. G.; Chappell, W. H. *Journal of Microelectromechanical Systems* **2010**, *19*, 951–960.
- [37] Schilling, G. D.; Andrade, F. J.; Barnes, J. H.; Sperline, R.; Denton, M. B.; Barinaga, C. J.; Koppenall, D. W.; Hieftje, G. M. *Analytical Chemistry* **2006**, *78*, 4319–4325.
- [38] Dempster, A. J. *Physical Review* **1918**, *11*, 316–325.
- [39] *Mass Spectrometry*; McDowell, C. A., Ed.; McGraw-Hill Book Company, Inc, 1963.
- [40] Nier, A. O. *Review of Scientific Instruments* **1940**, *11*, 212–216.
- [41] Bainbridge, K. T.; Jordan, E. B. *Physical Review* **1936**, *50*, 282–296.
- [42] Nier, A. O. *Review of Scientific Instruments* **1960**, *31*, 1127–1132.
- [43] Mattauch, J. *Physical Review* **1936**, *50*, 617–623.
- [44] Bleakney, W.; Hipple, J. A., Jr. *Physical Review* **1938**, *53*, 521–530.
- [45] Yates, R. C. *Curves and Their Properties*; National Council of Teachers of Mathematics, Inc: Washington, D.C., 1974.
- [46] Lockwood, E. H. *A Book of Curves*; Cambridge University Press: London, 1961.
- [47] Strobel, H. A.; Heineman, W. R. *Chemical Instrumentation: A Systematic Approach*, 3rd ed.; John Wiley & Sons, Inc: New York, New York, 1989.
- [48] Skoog, D. A.; Holler, F. J.; Nieman, T. A. *Principles of Instrumental Analysis, 5th Edition*; Brooks Cole, 1997.
- [49] Oppenheim, A. V.; Willsky, A. S. *Signals and Systems*; Prentice Hall: Englewood Cliffs, New Jersey, 1983.

- [50] Marple, S. L., Jr. *Digital Spectral Analysis with Applications*; Prentice Hall: Englewood Cliffs, New Jersey, 1987.
- [51] Mitra, S. K. *Digital Signal Processing: A Computer Based Approach*; McGraw-Hill, Inc: Boston MA, 2001.
- [52] Papoulis, A. *Probability, Random Variables, and Stochastic Processes*, 3rd ed.; McGraw-Hill, Inc: New York, New York, 1991.
- [53] Taylor, J. R. *An Introduction to Error Analysis*, 2nd ed.; University Science Books: Sausalito, California, 1997.
- [54] Bevington, P. R. *Data Reduction and Error Analysis for the Physical Sciences*; McGraw-Hill, Inc: New York, 1969.
- [55] Hayes, M. H. *Statistical Digital Signal Processing and Modeling*; John Wiley & Sons, Inc, 2002.
- [56] Fox, J. *Applied Regression Analysis, Linear Models, and Related Methods*; SAGE Publications: Thousand Oaks, CA, 1997.
- [57] Devore, J. L. *Probability and Statistics for Engineering and the Sciences*, 5th ed.; Duxbury: Pacific Grove, CA, 2000.
- [58] Priestley, M. B. *Spectral Analysis and Time Series: Vol 1 Univariate Series*; Academic Press: London, 1981.
- [59] Kailath, T.; Sayed, A. H.; Hassibi, B. *Linear Estimation*; Prentice Hall: Upper Saddle River, New Jersey, 2000.
- [60] Schonhoff, T. A.; Giordano, A. A. *Detection and Estimation Theory*; Prentice Hall: Upper Saddle River, New Jersey, 2006.
- [61] Sorenson, H. W. *Parameter Estimation*; Marcel Dekker, Inc: New York, 1980.
- [62] van der Ziel, A. *Noise*; Prentice Hall, 1954.
- [63] Janesick, J. R. *Scientific Charge-Coupled Devices*; SPIE Press: Bellingham, Washington USA, 2001.
- [64] Simoen, E.; Claeys, C. *Solid-State Electronics* **1999**, 43, 865–882.
- [65] Philip Cha, C. D., James Rosenberg *Fundamentals of Modeling and Analyzing Engineering Systems*; Cambridge University Press, 2000.
- [66] Grey, P. R.; Meyer, R. G. *Analysis and Design of Analog Integrated Circuits*; John Wiley & Sons, Inc, 1984.

- [67] Sperline, R.; Knight, A. K.; Gresham, C. A.; Koppenall, D. W.; Hieftje, G. M.; Denton, M. B. *Applied Spectroscopy* **2005**, *59*, 1315–23.
- [68] Boyd Fowler, e. a. *Proc SPIE* **1998**, *3301*, 178.
- [69] Garnett, J. D.; Forrest, W. J. *SPIE Proceedings, Infrared Detectors and Instrumentation* **1993**, *1946*, 395–404.
- [70] Lay, D. C. *Linear Algebra and Its Applications*; Addison-Wesley, 1999.
- [71] Teranishi, N.; Mutoh, N. *IEEE Transactions on Electron Devices* **1986**, *33*, 1696–1701.
- [72] Technology, L. *LTC6244 Dual 50 MHz, Low Noise, Rail-toRail, CMOS OP-Amp*, PDF, 2009. <http://cds.linear.com/docs/Datasheet/6244fb.pdf>.
- [73] Janesick, J.; Andrews, J. T.; Elliott, T. Fundamental performance differences between CMOS and CCD imagers; Part I. *High Energy, Optical, and Infrared Detectors for Astronomy II*, 2006; p 62760M.
- [74] Janesick, J.; Andrews, J.; Tower, J.; Grygon, M.; Elliott, T.; Cheng, J.; Lesser, M.; Pinter, J. Fundamental performance differences between CMOS and CCD imagers; Part II. *Focal Plane Arrays for Space Telescopes III*, 2007; p 669003.
- [75] Janesick, J.; Pinter, J.; Potter, R.; Elliott, T.; Andrews, J.; Tower, J.; Cheng, J.; Bishop, J. Fundamental performance differences between CMOS and CCD imagers; Part III. *Astronomical and Space Optical Systems*, 2009; p 743907.
- [76] Janesick, J.; Pinter, J.; Potter, R.; Elliott, T.; Andrews, J.; Tower, J.; Grygon, M.; Keller, D. Fundamental performance differences between CMOS and CCD imagers; Part IV. *High Energy, Optical, and Infrared Detectors for Astronomy IV*, 2010; p 77420B.
- [77] Kozlowski, L. J. *Proc. SPIE* **1996**, *2745*, 2–11.
- [78] Schilling, G. D.; Ray, S. J.; Rubinshteyn, A. A.; Felton, J. A.; Sperline, R.; Denton, M. B.; Barinaga, C. J.; Koppenall, D. W.; Hieftje, G. M. *Analytical Chemistry* **2009**, *81*, 5467–5473.
- [79] Felton, J. A.; Schilling, G. D.; Ray, S. J.; Sperline, R.; Denton, M. B.; Barinaga, C. J.; Koppenall, D. W.; Hieftje, G. M. *Journal of Analytical Atomic Spectrometry* **2011**, *26*, 300–304.
- [80] Robinson, C. F.; Hall, L. G. *The Review of Scientific Instruments* **1956**, *27*, 504–508.

- [81] Robinson, C. F. *The Review of Scientific Instruments* **1956**, *27*, 512–13.
- [82] Dibeler, V. H.; Reese, R. M.; Mohler, F. L. *Journal of Research of the National Bureau of Standards* **1956**, *57*, 113–118.
- [83] Smith, D.; Adams, N. G. *Journal of Physics E: Scientific Instruments* **1975**, *8*, 44–46.
- [84] Adams, N. G.; Smith, D. *Journal of Physics E: Scientific Instruments* **1974**, *7*, 759–68.
- [85] Halas, S. *International Journal of Applied Radiation and Isotopes* **1985**, *36*, 957–960.
- [86] Burr-Brown, I. *ACF2101 Low Noise, Dual Switched Integrator*, PDF, 200. <http://focus.ti.com/lit/ds/symlink/acf2101.pdf>.